Author:
Woolf, Martha L H

Title:
Ago2/DDX6-Dependent miRNA Activity in Neuronal Plasticity

University of BRISTOL

Ago2/DDX6-Dependent miRNA Activity in Neuronal Plasticity

Martha L H Woolf

September 2023

A dissertation submitted to the University of Bristol in accordance with the requirements for award of the degree of MSc by Research in the School of Biochemistry, Faculty of Life Sciences

Total Word Count: 20,152

(excludes references, appendices and lists of contents)

Abstract

MicroRNAs (miRNAs) and the RNA-induced silencing complex (RISC), provide extremely important fine-tuning of local protein expression within individual dendritic spines of the mammalian brain, via miRNA-mediated gene silencing. *In vitro*, NMDAR stimulation can cause spine shrinkage as a part of long-term depression (LTD), a form of plasticity. LTD has roles in cognition and learning, and notably in neurodegenerative diseases such as Alzheimer's. Phosphorylation of the core RISC protein Argonaute-2 (Ago2) at site S387 has been defined as a specific pathway for the regulation of structural plasticity, essential for spine shrinkage to occur. NMDAR stimulation has been shown to cause Akt-dependent phosphorylation at S387, with *in vitro* studies further evidencing that this phosphorylation event causes increased indirect association of Ago2 with DDX6, via GW182. Unpublished *in vitro* work from the Hanley lab has indicated this phosphorylation event causes rapid increased interactions of proteins Ago2 and DDX6 with mRNA *Limk1*, leading to its increased translational repression via miR-134, whereas mRNA *Apt1* binding and translational repression via miR-138 is unaffected by this phosphorylation event. The overall aim of this project was to determine how these findings translate to *ex vivo* studies. RNA-immunoprecipitations (RNA-IPs) followed by real-time quantitative PCR (RT-qPCR) were utilised to determine differences in direct interaction of Ago2 or DDX6 with mRNAs *Limk1* and *Apt1*, using cortical tissue from $Ago2^{WT}$ versus $Ago2^{S388A}$ phosphonull mutant mice. My hypothesis was that less *Limk1* would be repressed in the $Ago2^{S388A}$ mutant, via reduced direct Ago2-*Limk1* binding, and possibly also via reduced direct DDX6-*Limk1* binding. This reduction would not be expected of *Apt1* mRNA. Results did not provide any statistically significant differences in these interactions *ex vivo*, although it is notable that for Ago2-*Limk1* interactions, a near-significant difference consistent with the main hypothesis was observed. RNA isolation optimisations using TRIzol are also considered in this project.

Acknowledgements

Firstly, I would like to thank my primary supervisor Prof. Jonathan Hanley for the opportunity to carry out my MScR in his lab. Dipping a toe into the world of academic research this year has been as much a lesson for me in optimism as it has in optimisations (in the words of Jon himself). Although difficult at times, the experience has been invaluable. The support throughout my research year, especially in the final sprint to get things submitted on time, has been greatly appreciated.

Thank you to Fathima Perooli for your patience in guiding me through the troublesome world of RNA-IPs; I wish you all the best with picking up where I left off with the tissues. Thank you to Grace for your endless support and words of encouragement (and brains of mice!) throughout the year. Thank you to Sofia Raak for showing me the ropes with neurons, even if I never ended up using them. To Sam Atkinson and Johnnie Chronias, thank you for making the first few months of my time in the laboratory so enjoyable, it was a pleasure working alongside both of you.

A special thank you to Anne Dewitz for her undying support throughout my entire project. You have been a rock throughout my MScR year, and I do not know what I would have done without you keeping me company during hectic days and late nights of RNA-IPs. It has been a pleasure to have you as a mentor for the year, and I will continue to look up to you.

Finally, thank you to my APM reviewer Prof. Jon Lane, and to all the members of the Henley lab. It has been a pleasure to work alongside such driven and enthusiastic lab members.

(Plus, a shout out to all my family, and Jack, Michael, Sophie, and Albi for the support outside of the laboratory.)

Author's Declaration

I declare that the work in this dissertation was carried out in accordance with the requirements of the University's *Regulations and Code of Practice for Research Degree Programmes* and that it has not been submitted for any other academic award. Except where indicated by specific reference in the text, the work is the candidate's own work. Work done in collaboration with, or with the assistance of, others, is indicated as such. Any views expressed in the dissertation are those of the author.

SIGNED: Martha L H Woolf **DATE:** 5th September 2023

List of Contents

List of Figures

List of Tables

Abbreviations

3'/5'UTR – 3/5-Prime untranslated region

Aβ – Amyloid-Beta

Ab – Antibody

ABPs – Actin-binding proteins

AD – Alzheimer's Disease

Ago(1-4) – Argonaute(1-4)

Ago2^{S388A} – Argonaute-2, homozygous for S388A

Ago2^{WT}– Argonaute-2, homozygous for WT

AMPAR – α-amino-3-hydroxy-5-methyl-4-isoxazolepropionic acid receptor

AP – Action potential

Apt1 – Acyl-protein thioesterase 1

Apt1 – Apt1 mRNA

Arp2/3 – Actin-related protein 2/3 complex

ATP – Adenosine triphosphate

BDNF – Brain-derived neurotropic factor

BME – β-mercaptoethanol

BSA – Bovine serum albumin

Ca^{2+} - Calcium ions

CaMKII - Ca2+/calmodulin-dependent protein kinase II

Cas-9 – CRISPR-associated protein 9

cDNA – Complementary DNA

CNS – Central nervous system

Co-IP – Co-Immunoprecipitation

CRISPR – Clustered regularly interspaced short palindromic repeats

Ct – Cycle threshold

CTX – Cortex

ddH_2O – Double-distilled water

DDX6 – DEAD-box helicase 6

DEPC – Diethyl pyrocarbonate

DNA – Deoxyribonucleic acid

dsDNA – Double-stranded DNA

eIF4A – Eukaryotic initiation factor-4A

EtOH – Ethanol

F-actin – Filamentous actin

FISH - Fluorescence in situ hybridisation

FUNCAT - Fluorescence noncanonical amino acid tagging

GABA - Gamma-aminobutyric acid

G-actin – Globular actin

GluA1-4 - AMPAR subunits 1-4

GPCR - G-protein-coupled receptor

GRIP(1) - Glutamate receptor-interacting protein(-1)

HET – Heterozygous

HOM – Homozygous

HPC – Hippocampus

HRP – Horseradish peroxidase

Hsp70/Hsp90 – Heat shock proteins

iGluR - Ionotropic glutamate receptor

IP - Immunoprecipitation

L1/2 – Linker 1/2

LIMK/LIMK1 - LIM kinase(-1)

Limk1 – LIMK1 mRNA

LTD – Long-term depression

LTP – Long-term potentiation

Mg^{2+} - Magnesium ions

miRNA/miR – MicroRNA

MRE – miRNA response element

mRNA – Messenger RNA

Ms-IgG – Mouse Immunoglobulin G

NMDAR - N-methyl-D-aspartate receptor

ns – Non-significant

PAK - p21-activated kinase

PAZ - PIWI/Ago/Zwille

P-bodies – Processing bodies

PBS(-T) – Phosphate buffered saline (with Tween 20)

PCR – Polymerase chain reaction

PICK1 - Protein Interacting with C Kinase-1

PIWI – P-element-induced wimpy testis

Pol-II – RNA polymerase II

PSD – Postsynaptic density

PVDF – Polyvinylidene fluoride (membrane)

RISC – RNA-induced silencing complex

RLC – RISC loading complex

RNA – Ribonucleic acid

RNA-IP – RNA-Immunoprecipitation

RT-qPCR - Real-time quantitative PCR

S387/8 – Serine-387/8

S388A – Serine-388-alanine (single amino acid change)

SD – Standard deviation

SDS-PAGE - Sodium dodecyl sulphate-polyacrylamide gel electrophoresis

SEM – Standard error of the mean

shRNA – Small hairpin RNA

siRNA - Small interfering RNA

ssDNA – Single-stranded DNA

TARP - Transmembrane AMPAR regulatory proteins

TEMED - Tetramethylethylenediamine

TRAP - Translating ribosome affinity purity

TRBP - Transactivating response RNA-binding protein

WB – Western blot(ting)

WT – Wild-type

Units

°C – Degrees Celsius

µg/mg – Micro/milligram(s)

µM – Micromolar

h – Hour(s)

kDa – Kilodaltons

mA – Milliamps

min – Minute(s)

mL – Millilitre(s)

nm/mm – Nano/millimetre

RCF (or g) – Relative centrifugal force

RPM – Revolutions per minute

s – Seconds

V – Volts

1. Introduction

1.1 The Brain and Neurons

The capacity of humans and other mammals to carry out processes of learning and memory are dependent on a complex flow of information centralised within the brain. Highly specialised cells called neurons are responsible for the processes of signal retrieval, integration, and transmission. There are billions of neurons present within the human brain (Herculano-Houzel, 2009), supported by non-neuronal glial cells. The highly polarised morphology of neurons (**Fig1.1**) is critical for their function (Schelski & Bradke, 2017) as it allows directional signal transmission along their lengths, in the form of electrical impulses, or action potentials (APs). Almost all neuronal cytoplasm is contained within highly branched structures known as axons and dendrites, which extend from the cell body (or soma) where the nucleus is located. Dendrites on the neuron are responsible for receiving signal inputs from multiple sources and allows signal information to be integrated together to provide a single processed output that can then be transmitted down an elongated axon. A myelin sheath surrounding the axon allows for the acceleration of signal transmission along long distances (Sherman & Brophy, 2005). Communication between two neurons occurs at specialised junctions known as synapses (Herculano-Houzel, 2009).

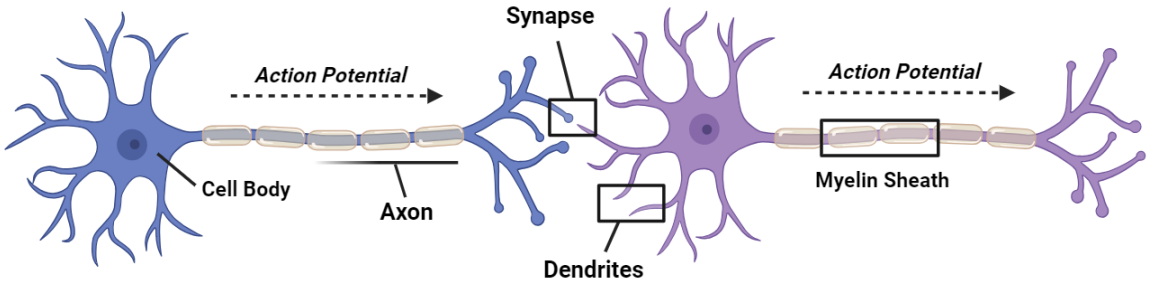

Figure 1.1: Polarised neuronal morphology. *A basic illustration of the morphology of two neurons, with the direction of action potentials indicated. Communication between the two occurs at a synapse, where the axon of one neuron meets the dendrite of another. (Created using BioRender)*

1.2 Synaptic Transmission

Unlike the transmission of signals along a neuron itself, synapses can be either electrical or chemical. Electrical synaptic transmission is based purely upon flow of ions in the same way as APs, whereas chemical synaptic transmission is based upon the release and detection of neurotransmitters, which

rapidly diffuse across a synaptic cleft (20-40 nm wide) (Pitman, 1984). At electrical synapses, ion-conducting pores known as connexins act at gap junctions to allow ions to flow directly between the intracellular compartments of adjacent neurons (Faber & Pereda, 2018). Electrical synaptic transmission is extremely simplistic and cannot contribute to inhibitory actions or produce long-lasting adaptations to electrical properties in postsynaptic neurons. Chemical synapses, however, are more specialised than electrical synapses and can therefore contribute to more complex neuronal signalling and neuronal behaviours, such as amplification of signals from presynaptic neurons.

The mechanism of chemical synaptic transmission (**Fig 1.2**) is dependent on initial firing of APs along the presynaptic neuron, which triggers neurotransmitter release from a presynaptic terminal within the axon (Pitman, 1984). Neurotransmitters rapidly diffuse across the cleft to the postsynaptic neuron, where they bind to transmembrane receptors to initiate further signal transmission. The two main receptor classes present at the postsynaptic membrane are ionotropic, ligand-gated ion channels, and metabotropic G-protein-coupled receptors (GPCRs) (Reiner & Levitz, 2018). Ionotropic receptors regulate ion flow through opening and closing of ion channels, whereas metabotropic receptors activate a variety of complex intracellular signalling cascades.

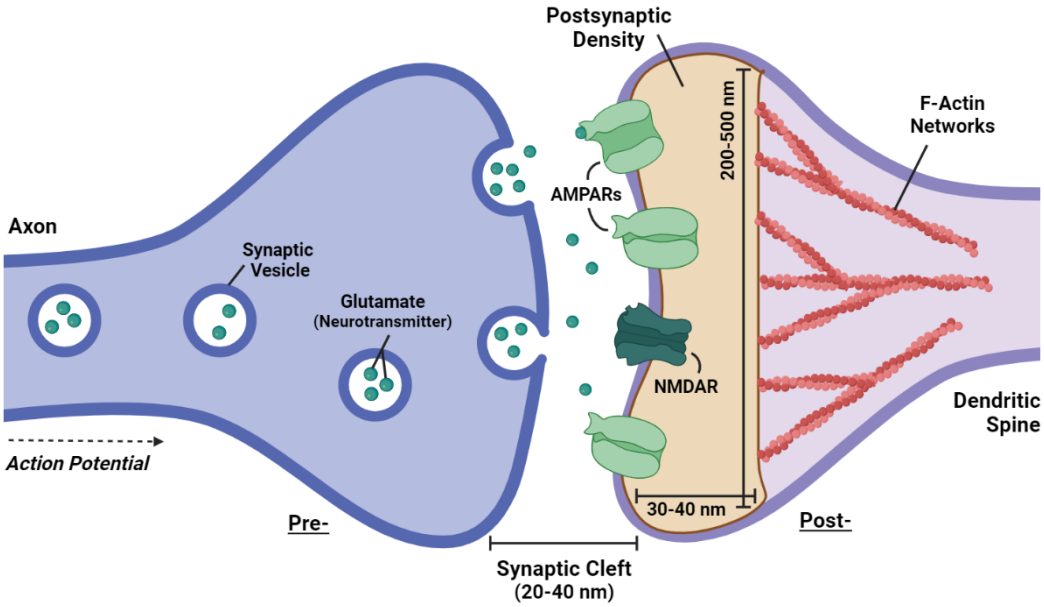

Figure 1.2: Chemical synaptic transmission. *An illustration depicting an excitatory chemical synapse. Neurotransmitter is released from the presynaptic neuron and interacts with receptors on the postsynaptic membrane. The postsynaptic density and actin network is also depicted within the postsynaptic dendritic spine. (Created using BioRender)*

Neurotransmitters can be classified as excitatory or inhibitory, depending on their characteristic abilities to open or close ion channels, and the ion selectivity of the channel itself. In the brain, glutamate acts as the major excitatory neurotransmitter (Hansen et al., 2021), and gamma-aminobutyric acid (GABA) acts as the major inhibitory neurotransmitter (Jembrek & Vlainic, 2015). Certain neurotransmitters can act as both excitatory and inhibitory molecules, with their activity at a given synapse dependent upon the postsynaptic receptors present. Most chemical neurotransmitter molecules are either amino acids, monoamines or peptides, with both glutamate and GABA being amino acids. The actions of neurotransmitters on their receptors cause electrical activity in the postsynaptic neuron to be altered, on timescales spanning milliseconds to minutes. Depending on the synapse and neurotransmitters involved, this response can be either excitatory or inhibitory.

Excitatory neurotransmitter glutamate mediates synaptic plasticity and hence learning and memory. Glutamate can act upon numerous receptor targets, including the ionotropic glutamate receptor (iGluR) family, that exhibit specific glutamate binding sites (Hansen et al., 2021). There are two major types of iGluR present on the postsynaptic membrane, both transmembrane proteins with tetrameric structures, that are named after their activating agonists: α-amino-3-hydroxy-5-methyl-4-isoxazolepropionic acid receptors (AMPARs) and N-methyl-D-aspartate receptors (NMDARs).

Modifying the strength of pre-existing synapses within the hippocampus is fundamental in learning and memory (Bliss & Collingridge, 1993). Synaptic transmission efficacy can be altered by both presynaptic and postsynaptic changes in electrophysiological activity. In receiving dendrites, key changes in synaptic activity and strength occur through modification of small, membranous structures known as dendritic spines, where most excitatory synapses are located (Berry & Nedivi, 2017). The importance of dendritic spines in the processes of synaptic plasticity are explained further in the section **1.5 Synaptic Plasticity** (p28).

1.3 Dendritic Spines and the Postsynaptic Density

Dendritic spines are essential for receiving excitatory input into the brain. They were first observed in 1896 by Cajal by light microscopy using the Golgi method or silver impregnation, with Methylene Blue staining verifying their presence along dendrites (García-López et al., 2007; Ramón & Cajal, 1888). Spine morphology is highly dynamic, allowing for spine formation, growth, shrinkage, and removal when required, with spines taking on varying morphologies. They can be classified as thin, stubby , or mushroom spines (**Fig1.3**), with mushroom spines having a bulbous head protruding from the dendrite via a thin neck (Harris et al., 1992). Activity-dependent changes in spine morphology

can occur via numerous complex signalling pathways. Individual spines act as individual compartments and can be regulated separately from their neighbouring spines (Müller & Connor, 1991).

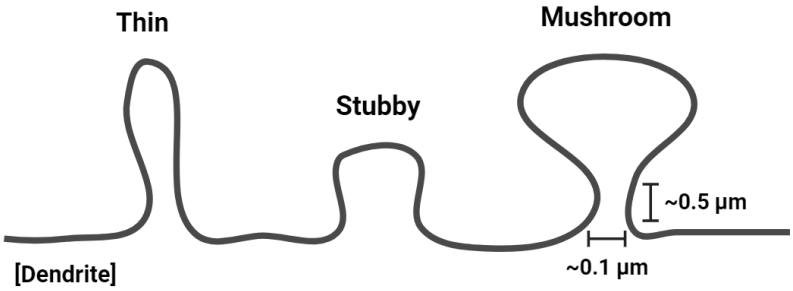

Figure 1.3: Dendritic spine morphology*. A basic illustration to show variation in spine morphology. Thin, stubby, and mushroom spines shown, with diameter and length of mushroom spine neck indicated.*

The head of a dendritic spine houses an electron-dense, macromolecular structure called the postsynaptic density (PSD) (Cotman et al., 1974). In excitatory neurons, the PSD is usually large and protein-rich, 30-40 nm thick and 200-500 nm wide with over 1000 proteins present (Sheng & Hoogenraad, 2007; Yamauchi, 2002). Inhibitory synapses house a PSD that is much thinner, with fewer proteins present. Positioning of the PSD close to the postsynaptic membrane is extremely important as its proteins regulate numerous activities here, with certain PSD proteins associating with the membrane itself. PSD proteins include transmembrane proteins such as glutamate receptors and adhesion molecules, cytoskeletal proteins such as actin and actin-binding proteins (ABPs), scaffold proteins such as PSD-95, and signalling proteins such as calcium/calmodulin dependent kinase II (CamKII) (Sheng & Hoogenraad, 2007). These proteins have numerous functions such as aiding in receptor clustering, adhesion, and synaptic transmission (Sheng & Hoogenraad, 2007).

Dendritic spines are rich in the structural protein actin, the main component of their cytoskeleton. The polymerisation of globular (G-)actin into actin filaments (F-actin) is aided by ABPs. Actin polymerisation and depolymerisation plays the principal role in underlying highly variable spine morphologies (Hotulainen & Hoogenraad, 2010).

1.4 RNA-Induced Silencing Complex

The RNA-induced silencing complex (RISC) is a ribonucleoprotein complex, consisting of multiple proteins and a small single-stranded RNA, such as a microRNA (miRNA) or a small interfering RNA (siRNA) (Ipsaro & Joshua-Tor, 2015; Iwakawa & Tomari, 2022), illustrated in **Fig1.4**.

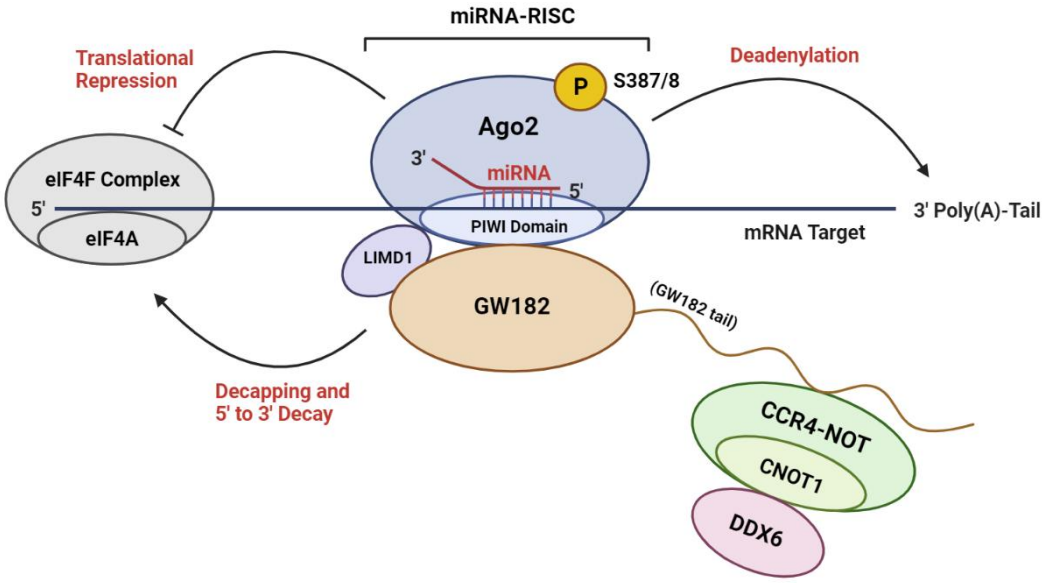

Figure 1.4: The RNA-Induced Silencing Complex. *An illustration of the key proteins in RISC. Methods of miRNA-mediated gene silencing via RISC are also indicated, along with Ago2 phosphorylation at S387/8. (Created using BioRender)*

Gene silencing can be mediated by RISC via various mechanisms, but in mammals it acts at a translational level, through cleavage of mRNA or causing translational repression (McManus & Sharp, 2002). RISC mediates a gene silencing event known as RNA interference, a sequence-specific silencing that occurs in most eukaryotic organisms, which acts to reduce expression of certain genes. Once associated with RISC proteins, miRNA targets mRNAs through complementary base pairing (Ipsaro & Joshua-Tor, 2015) and gene silencing is then performed by the protein components of RISC, including Argonaute-2 (Ago2), Dicer, DDX6, GW182, and the CCR4-NOT complex. mRNA translation is repressed as 5'-cap-dependent steps are inhibited (Douglas & Birchler, 2013).

1.4.1 Protein components of RISC

1.4.1.1 Argonaute-2 (Ago2)

The family of Argonaute (Ago) proteins are the core proteins in RISC and are highly conserved in almost all organisms, from eukaryotes to bacteria (Wu et al., 2020). They predominantly mediate gene silencing (Jin et al., 2021), and contrarily in rare occasions also can mediate activation of gene expression (Iwasaki & Tomari, 2009). Ago can also regulate alternative splicing, genome integrity control, DNA repair and epigenetic chromatin modifications (Li et al., 2020), once loaded with a small RNA. Four Ago proteins (Ago1-4) are expressed in mammalian cells (encoded by the genes *EIF2C1-4* in humans), with highly conserved domain architecture (Wu et al., 2020). They have four domains, arranged within a bilobed structure (**Fig1.5**). An N-terminal domain and PAZ (PIWI/Ago/Zwille) domain are connected by Linker 1 (L1) and form the first lobe, and the second lobe contains MID domain and PIWI (P-element-induced wimpy testis) domain, connected to the first lobe by Linker 2 (L2).

Ago2 is the best characterised and most widely studied of the Ago proteins. It is an endonucleolytic protein and has the most highly reported catalytic activity of the Ago proteins. It is the key protein component of RISC (Liu et al., 2004), with the N-terminal domain mediating RNA unwinding and loading of the guide strand (Kwak & Tomari, 2012). The structure of Ago2 allows for the cleavage of target mRNAs, where the post seed region of an Ago2-associated miRNA pairs with the 3’ and 5’ flanking regions of the mRNA. The binding of small RNAs to Ago2 causes a rearrangement in the bilobed structure of Ago2. Within a binding pocket of Ago2, a non-specific interaction between the 3’ overhang of the RNA with the PAZ domain protects the RNA in question from being degraded (Simon et al., 2011; Tian et al., 2011). Another RNA binding pocket is responsible for the interaction of the 5’-terminal of the guide strand associating with the MID domain of Ago2, which is essential for subsequent cleavage activity (Wang et al., 2019). The PIWI domain has endonuclease properties which can provide cleavage of target mRNAs in some cases (Cenik & Zamore, 2011).

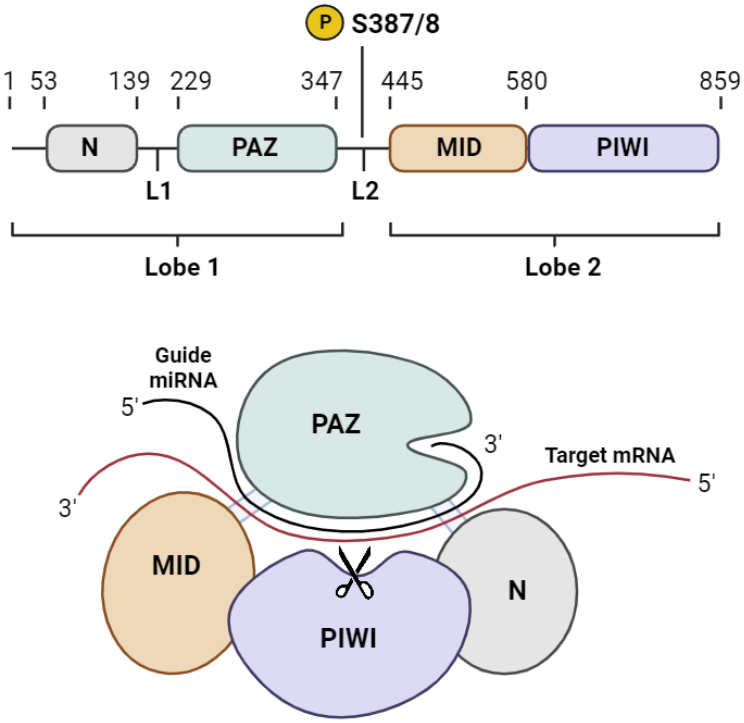

Figure 1.5: The domain architecture of human Ago2. *An illustration of the domains of Ago2 and its bi-lobed structure. The top figure shows domains N, PAZ, MID and PIWI with their amino acid locations; the phosphorylation site of S387 within L2 is also indicated. [NB: S388 is the site of phosphorylation in mice.] The below figure shows a basic structure of Ago2 with its associated guide miRNA and target mRNA interacting. A miRNA binding pocket on PAZ, and mRNA cleavage site on PIWI is also shown. (Created using BioRender)*

Post-translational modifications of Ago2 have important roles in regulating its function. These modifications include phosphorylation, methylation, ubiquitination, SUMOylation and hydroxylation (Josa-Prado et al., 2015; Lopez-Orozco et al., 2015; Qi et al., 2008; Zhang et al., 2022). Both methylation of Ago3 proteins, in the PIWI domain, and hydroxylation of Ago2 has been shown to affect the stability of Ago proteins (Kirino et al., 2009; Qi et al., 2008), for example.

1.4.1.2 Ago2 Phosphorylation

Phosphorylation is the most common form of Ago2 post-translational modifications, with Ago2 containing phosphorylation sites at multiple serine and tyrosine residues. Phosphorylation of Ago2 is important in regulating numerous protein-protein and protein-RNA interactions, including binding of

Ago2 to small RNAs which lends itself to mediating gene silencing activities (Lopez-Orozco et al., 2015).

Phosphorylation of serine-387 (S387) (Rajgor et al., 2018), or S388 in mice, is the phosphorylation site of interest in this project. Phosphorylation of S387 can be mediated by MAPK (Zeng et al., 2008), and is also Akt-dependent, with phosphorylation shown to be mediated by proto-oncogene Akt-3 (Horman et al., 2013) and two further Akt isoforms, Akt1-2 (Rajgor et al., 2018). Akt-dependent S387 phosphorylation is multifunctional, contributing to increases in translational repression, decreased cleavage activity, and reduced exosome sorting. Akt-3 phosphorylation of S387 on Ago2 can be achieved in neurons via NMDAR stimulation (Rajgor et al., 2018). Furthermore, Akt-mediated phosphorylation has shown to increase direct interaction of Ago2 with GW182 within RISC, in HeLa cells (Horman et al., 2013), and indirect association of Ago2 with DDX6 via this GW182 association in neurons (Rajgor et al., 2018), enhancing miRNA-mediated translational repression. In HeLa cells this switch to upregulation of translational repression is observed alongside downregulations in cleavage of endogenous mRNA, which insinuate that this phosphorylation may cause changes in interactions of key proteins responsible for these differing processes (Horman et al., 2013). The phosphorylation of Ago2 is also involved in its subcellular localisation; MAPK-mediated phosphorylation is responsible for the localisation of Ago2 within processing bodies (P-bodies).

1.4.1.3 GW182, LIMD1 and CCR4-NOT1

GW182 acts as a molecular scaffold protein within RISC, allowing for the binding of other proteins including DDX6 and the CCR4-NOT1 complex. The N-terminal of GW182 itself directly interacts with the PIWI domain of Ago (Behm-Ansmant et al., 2006). The protein LIMD1 binds both Ago2 and GW182 and is responsible for the coordination of Ago2-GW182 assembly (Bridge et al., 2017). Furthermore, Akt-dependent Ago2 S387 phosphorylation has been shown to increase binding to LIMD1 and subsequently enhance Ago2 interactions with GW182 and DDX6.

Interaction of the silencing domain of GW182 with the CNOT1 subunit of CCR4-NOT1, mediates translational gene repression, bringing the complex closer to the target mRNA to allow mRNA decay to occur via CCR4-NOT1 deadenylating activity which shortens the mRNA 3'-poly(A) tail (Behm-Ansmant et al., 2006). Shortening of mRNA causes reduced rates of translation and eventual mRNA decapping and degradation. Inhibiting the interaction of GW182 with Ago2 disrupts gene silencing via miRNAs, and LIMD1 knockout causes loss of Ago2 miRNA-silencing function (Bridge et al., 2017).

1.4.1.4 DDX6 Recruitment

DDX6 is a member of the ATP-dependent DEAD-box helicase family (Wang et al., 2015). It is highly conserved from prokaryotes to vertebrates, containing a conserved DEAD-box motif in its sequence that allows RNA helicase activity, and has different orthologs identified across species (Ostareck et al., 2014).

The DDX6 ortholog Rck/p54 in humans was first identified as a proto-oncogene product, causing chromosomal aberrations, and being involved in several cancers (Akao et al., 1995). It has since been discovered that translational repression of mRNAs requires DDX6, and DDX6 activity also helps to mediate activation of the mRNA decapping complex and assembly of P-bodies, contributing to miRNA-mediated gene silencing (Rouya et al., 2014). DDX6 structurally resembles the mRNA binding translation factor eukaryotic initiation factor-4A (eIF4A).

DDX6 forms an RNA-binding channel within its structure. RNA interactions with DDX6 can occur in an ATP-independent manner in its usual autoinhibited conformation (Ernoult-Lange et al., 2012). It has been revealed that CNOT1 is responsible for modulating DDX6 ATP-dependent activity (Mathys et al., 2014). It has been demonstrated that in human cells, DDX6 interacts indirectly with both Ago2 and GW182, via CNOT1. Basally, the interaction of Ago2 with DDX6 that occurs via the CNOT1 subunit within the CCR4-NOT1 is weak. The increase in this binding of DDX6 to the CNOT1 complex that occurs with increased NMDAR stimulation is essential to prime the active conformation of DDX6 and stimulate ATPase activity (Mathys et al., 2014). Using small hairpin RNA (shRNA) to knockdown DDX6 in HeLa cells causes mRNA silencing impairment. Furthermore, disruption of DDX6-CNOT1 binding via mutation of arginine-386 to a glutamic acid within DDX6 was shown to block miRNA-dependent silencing mediated by DDX6 (Rouya et al., 2014).

1.4.2 MicroRNAs

1.4.2.1 An introduction to miRNAs

miRNAs are small, non-coding RNAs, on average 19-22 nucleotides in length. They are mostly ubiquitously expressed, with some being organ- or tissue-specific. Aided by RISC, they can post-transcriptionally regulate gene expression. In the nucleus, RNA polymerase II (Pol-II) is responsible for transcription of miRNAs (Lee et al., 2004). The location of miRNAs within the genome can generally group them into two main classifications, intronic or intergenic (Ramalingam et al., 2014). Introns are non-coding regions on DNA or RNA transcripts that are spliced out before translation occurs. It has been shown that around 40% of miRNAs are intronic and are transcribed by Pol-II using

the promoters of host encoded genes, meaning the miRNA is usually coexpressed alongside an mRNA (Rodriguez et al., 2004). Intergenic miRNAs have their own promoters and are therefore not dependent on a host gene for transcriptional regulation. The RNase III protein Dicer processes pre-miRNA into mature miRNA, which is the form of miRNA that is capable of binding to Ago2 (Michlewski & Cáceres, 2019).

miRNAs regulate a wide range of different cellular mechanisms throughout the body, including cell differentiation, proliferation, apoptosis and metastasis (Ha & Kim, 2014). In the nervous system, characterised miRNAs regulate many neuronal genes, fine-tuning local regulation of the proteome within individual spines. Targeting of key structural proteins can cause spine shrinkage, with rapid modulation of the proteome through miRNA activity essential for structural plasticity.

1.4.2.2 MiRNA Biogenesis

There are two pathways through which miRNA biogenesis can occur (Ha & Kim, 2014). The canonical pathway is dominant, notably requiring both Drosha and Dicer proteins for two levels of miRNA processing. Non-canonical pathways are either Drosha-independent or Dicer-independent, but each make use of the other proteins usually utilised in the canonical pathway.

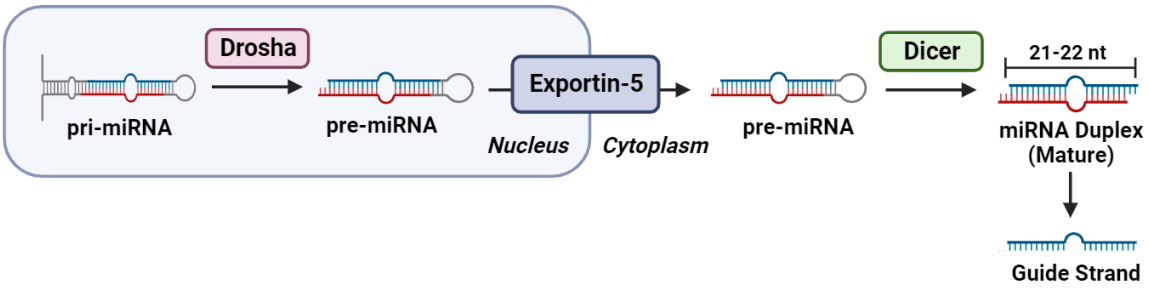

Figure 1.6: Canonical miRNA biogenesis. *An illustration of miRNA biogenesis, from primary miRNA to production of a mature miRNA guide strand. (Created using Biorender)*

In the canonical pathway (**Fig1.6**), the nuclear microprocessor complex including the ribonuclease III enzyme Drosha, recognises and processes primary miRNA transcripts in their double-stranded stem loop structure. Drosha generates precursor (pre-)miRNA with a 3' overhang of around 70-100 nucleotides in length, by cleavage of the miRNA at the base of its hairpin structure. This pre-miRNA is transported from the nucleus into the cytoplasm via Exportin-5. Another ribonuclease III enzyme

known as Dicer removes a terminal loop of pre-miRNA to form a duplex, on average 21-22 nucleotides long. Of this duplex, one strand is selected to be loaded into RISC by interactions with Ago2; this strand is defined as the guide strand (Ipsaro & Joshua-Tor, 2015). In Drosha-independent pathways, certain pre-miRNAs can be translocated to the cytoplasm without the use of Drosha, as the pre-miRNA already resembles a Dicer substrate. Where Dicer-independent pathways occur, a full, unprocessed pre-miRNA is loaded into Ago2.

1.4.2.3 miRNA Loading into RISC Loading Complex

The RISC loading complex (RLC) is responsible for the loading of RNA duplexes, and consists of the proteins Ago2, Dicer and transactivating response RNA-binding protein (TRBP) (Wang et al., 2009). Of the mature miRNA duplex, the strand that has a 5'-end with a lower thermodynamic stability is preferentially selected as a guide strand, and the other becomes a passenger strand (Meijer et al., 2014). The guide strand can be divided into five distinct, functional units. The 5'-end which interacts with a MID domain, a seed sequence directly following the 5'-end, a central region, 3' complementary sequences and finally a 3'-tail which interacts with a PAZ domain (Ma et al., 2004). Following duplex production by Dicer, Dicer interacts with Ago2 and TRBP, and the guide strand of mature miRNA then binds to Ago2. TRBP binds the double-stranded miRNA, and the heat shock multiprotein Hsp70/Hsp90 then causes a conformational change to occur in Ago2 (Naruse et al., 2018), that allows the duplex to be successfully transferred into Ago2, and therefore the RISC. This primes the RLC to carry out miRNA-mediated gene-silencing aided by actions of different RISC proteins. In humans, the removal of the passenger strand is then mediated by endonuclease Ago2 (Wang et al., 2009).

1.4.2.4 miRNA-Mediated Gene-Silencing

The mechanism of post-transcriptional regulation of protein expression that a miRNA mediates is determined by the degree of complementarity between the miRNA and the mRNA seed sequences (Ipsaro & Joshua-Tor, 2015). For mRNAs, this seed sequence consists of 2-8 nucleotides present at the 5'-end of a specific sequence known as a miRNA response element (MRE) (Alshalalfa, 2012). The MRE is almost always located within the 3-prime untranslated region (3'UTR) of the mRNA, although in some rare cases can be located elsewhere within the transcript, in promoter or coding sequences, or within the 5'UTR. In animals, most miRNAs do not have perfect complementarity with their target, and this leads to gene silencing through mRNA decay or translational repression, rather than

processes of direct cleavage and degradation that occur with perfect complementarity (Muljo et al., 2010).

Reportedly, approximately 70% of all discovered miRNAs are expressed within brain regions (Chen & Qin, 2015), with most neuronal miRNAs having important roles in the processes of functional or structural plasticity, through silencing gene expression.

1.5 Synaptic Plasticity

Synaptic plasticity is an extremely important property of the mammalian brain, as it allows the adaptation of behaviours via modification of related neural circuits at the level of the synapse, based upon historical neuronal activity. Activity-dependent changes at pre-existing synapses, such as in regulation of both size and strength of dendritic spines, can cause an enhancement or reduction in the efficiency of synaptic transmission (Meriney & Fanselow, 2019). Dynamic, activity-dependent AMPAR trafficking is essential for changes in synaptic strength (Antunes & Simoes-de-Souza, 2018). Different spine morphologies compartmentalise signalling factors and receptor machineries differently. Spine volume is proportional to PSD volume, and in turn proportional to the levels within spines of cytoskeletal molecules, surface expression of AMPARs, and therefore also amplitude of AMPAR-mediated currents. Synaptic plasticity can be bi-directional (Milstein et al., 2021) and can provide modification of synaptic strength that lasts for sub-second timescales, to timescales of hours or even days. Synaptic plasticity plays key roles in memory formation, development of the brain and in recovery of function following injuries. It has also been associated with drug addiction (Smith & Kenny, 2018) and neurodegenerative diseases such as Alzheimer's (Wang et al., 2011).

1.5.1 Homeostatic versus Hebbian Plasticity

Homeostatic plasticity is aptly named as it describes a form of plasticity that acts to return a neuron back to an initial, homeostatic point (Fox & Stryker, 2017). This form of plasticity has a significant role in the development of neuronal circuits. Homeostatic plasticity ensures that, on the one hand, a decrease in overall neuronal activity does not cause a comatose state, and on the other hand, a long-term increase in neuronal activity does not saturate synaptic strength, as this would reduce the ability of neurons to encode signals and could also lead to excitotoxic damage in extreme cases. Homeostatic plasticity occurs via processes such as synaptic scaling across all synaptic connections of

a neuron, changes in inhibition, or changes in the intrinsic properties of the neuronal membrane. This synaptic scaling causes either a net upscaling or downscaling of synaptic strength, to oppose any long-term decrease or increase in activity, respectively.

A model for Hebbian plasticity was formulated in the 1940s by Hebb (Hebb, 1949), leading on from proposed mechanisms in plasticity from Cajal, following his dendritic spine discovery (DeFelipe, 2006; Ramón & Cajal, 1888). Hebbian plasticity acts on a faster timescale than homeostatic plasticity and is essential in storing of information in memory formation. It is vital in many fundamental brain properties, including in development, memory and learning, as well as in recovery after loss of function (Fox & Stryker, 2017). This form of plasticity supports the idea that synaptic strength can be modified by both pre- and postsynaptic changes in activity. Hebbian plasticity can be split into two forms, short-term and long-term plasticity.

1.5.2 Short- versus Long-Term Plasticity

Short-term plasticity, observed in invertebrates to mammals, allows for changes in the strength of synaptic transmission to occur on timescales of milliseconds to minutes (Zucker & Regehr, 2002). The underlying mechanisms of short-term plasticity are almost entirely presynaptic in nature. Paired-pulse (or short-term) depression or facilitation are the two main forms of short-term plasticity. Paired-pulse depression is caused by a transient depletion of synaptic vesicles at short interstimulus intervals (under 20 ms) and is observed at all synapses (Zucker & Regehr, 2002). Paired-pulse facilitation is caused by transient cytosolic Ca^{2+} accumulation in the axon terminal and is exhibited at longer interstimulus intervals (from 20 to 500 ms) (Katz & Miledi, 1968).

Long-term plasticity allows for persistent, long-lasting changes in strength of synaptic transmission to occur, on timescales of hours to days. Mechanisms dependent upon protein synthesis underlie this sustained expression of long-term plasticity, with regulation of such allowing late-phase plasticity to take over from early-phase plasticity (Bliss & Cooke, 2011). Experimentally, this form of plasticity was first observed in the hippocampus of a rabbit, with enhancement of synaptic transmission lasting hours to days following repetitive excitatory synapse activation (Bliss & Lomo, 1973). The two forms of long-term plasticity are long-term potentiation (LTP) and long-term depression (LTD)

1.5.3 Long-Term Potentiation (LTP) and Long-Term Depression (LTD)

LTP describes a rapid and long-lasting increase in synaptic strength caused by high frequency stimulation, and is the predominant mechanism associated with learning and memory (Baltaci et al., 2019). In the CNS, LTP is mainly dependent on activation of Ca^{2+}-permeable NMDARs, although NMDAR-independent forms of LTP have also been discovered (Bliss & Cooke, 2011).

LTD describes a persistent, long-lasting decrease in synaptic strength, up to hours or days. The discovery of LTD was first made as a breakthrough in the 1990s using Schaffer collateral synapses of the CA1 region of the hippocampus (Dudek & Bear, 1992), where a reliable homosynaptic LTD of basal synaptic response was elicited experimentally using low frequency (0.5-3 Hz) stimulation (LFS) (Huber et al., 2001). Experimental LFS causes LTD via NMDAR-dependent mechanisms. Similarly to LTP, LTD in the CNS usually requires the activation of NMDARs, which increases the concentration of postsynaptic Ca^{2+} (Bliss & Cooke, 2011), although some NMDAR-independent forms of LTD exist such as through activation of metabotropic glutamate receptors. This proved that changes in synaptic strength could be bidirectional as well as activity-dependent, supporting the idea that the storing of memories was not only modulated by the process of LTP, but also by LTD (Connor & Wang, 2016).

1.5.4 NMDAR-Dependent Plasticity

NMDARs are considered coincidence detector of pre- and post-synaptic activity, as they require binding of two co-agonists, glutamate and glycine, for activation (Bliss & Cooke, 2011). Sufficient depolarisation in the postsynaptic neuron allows NMDAR channel opening as it expels a magnesium ion (Mg^{2+}) channel block in a voltage-dependent manner, allowing for non-selective positive ion flow. The influx of Ca^{2+} into the postsynaptic neuron, specifically, triggers intracellular signalling pathways that can ultimately alter synaptic plasticity through downstream regulation of various cellular activities (Bliss & Cooke, 2011).

AMPARs are the principal iGluRs acting at the postsynaptic membrane and their dynamic expression and trafficking within dendritic spines is essential in modulating synaptic strength and plasticity. Rapid increase or decrease of AMPAR surface expression is characteristic of LTP or LTD, respectively (Bassani et al., 2013). The regulation of AMPAR trafficking is activity-dependent, aided by post-translational modifications of their C-terminus and interactions with AMPAR-interacting proteins, that cause further downstream signalling events to occur via various pathways. AMPAR-interacting proteins such as scaffold proteins interact with AMPARs in a subunit-specific manner, due to C-terminal domain variation (Shepherd & Huganir, 2007; Song & Huganir, 2002). Scaffold proteins are

crucial in AMPAR trafficking and channel gating and are also regulated themselves by post-translational modifications such as phosphorylation (Yokoi et al., 2012).

Conventionally, the pathway for LTD induction is NMDAR-dependent. NMDAR activation can occur either via action of their neurotransmitter agonists, or through electrical stimulation, with both resulting in a modest but prolonged increase in postsynaptic Ca^{2+} concentration within the dendritic spine (Huber et al., 2001). The subsequent downstream Ca^{2+}-dependent activation of a serine-threonine phosphatase cascade and action of kinases ultimately causes decreased AMPAR surface expression. This occurs as activated phosphatases dephosphorylate the AMPAR subunit GluA1 at sites S831 and S845, reducing the AMPAR open-channel probability, whilst kinases phosphorylate subunit GluA2 at site S880 which reduces AMPAR stability due to disrupted interactions with PDZ proteins such as GRIP1 (He et al., 2009; Tan et al., 2020). The dissociation of AMPARs away from scaffold proteins allows them to be endocytosed in a clathrin-mediated fashion at extrasynaptic sites (Parkinson & Hanley, 2018), either at the somatodendritic region or at endocytic zones positioned closer to the PSD. Once endocytosed AMPARs are either degraded in lysosomes, retained in endosomal compartments, or recycled back to the cell surface (Parkinson & Hanley, 2018).

1.6 Structural Plasticity in Spines

1.6.1 Mechanism of Structural Plasticity

The morphology of neurons, and vitally of their dendritic spines, can be modified in an activity-dependent manner by mechanisms of structural plasticity. Structural changes are brought about via changes in cytoskeletal-related signalling via modifications of gene expression and synthesis of key protein players. Structural plasticity of dendritic spines lends itself to their dynamic nature, allowing their formation, growth, and shrinkage to be carried out in mature neurons. Growth of spines correlates with LTP (Lisman, 2003), with LTP induction linked to increasing actin polymerisation within spines, whereas shrinkage correlates to LTD (Zhou et al., 2004). A basic overview of how miRNA-mediated gene silencing via RISC leads to LTD is shown in **Fig1.7**.

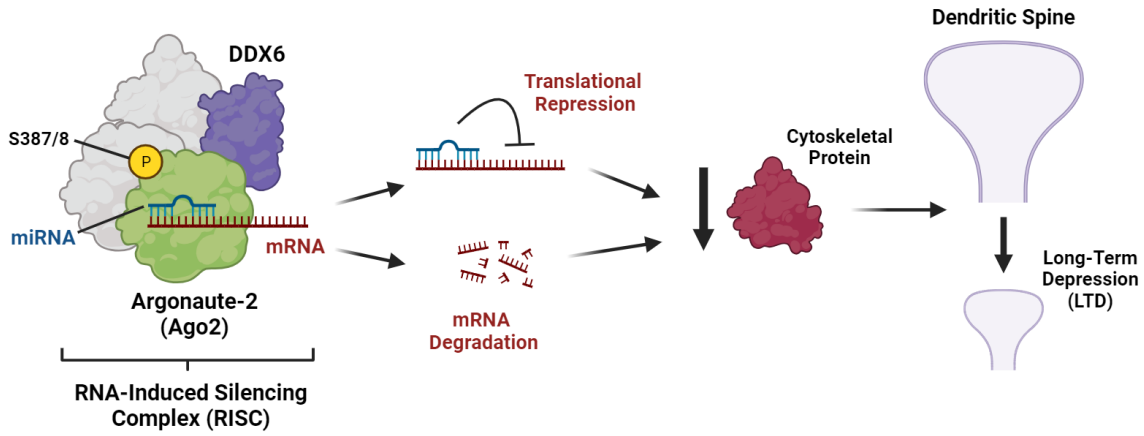

Figure 1.7: miRNA-mediated gene silencing via RISC can cause LTD. *Targeting of mRNAs coding for cytoskeletal proteins can cause spine shrinkage, and hence LTD. (Created using Biorender)*

Structural plasticity can be initiated within individual spines via NMDAR activation (Bliss & Cooke, 2011). The ability of dendritic spines to act as their own individual compartments – without affecting neighbouring spines (Müller & Connor, 1991) can be demonstrated by studying the rapid accumulation of Ca^{2+} that occurs within NMDAR-stimulated spines, using glutamate uncaging experiments (Sobczyk & Svoboda, 2007).

CaMKII is the most abundant protein within excitatory synapses, so unsurprisingly has a major role in the regulation of multiple spine processes, contributing to synaptic plasticity and in turn to learning and memory (Malenka et al., 1989; Yasuda et al., 2022). During the early stages of plasticity in LTP, Ca^{2+} influx leads to a downstream activation of the 'gate-keeper' CaMKII (Lledo et al., 1995), which then mediates later stages of LTP. CaMKII kinase activity on AMPARs acts to increase receptor conductance and mediate AMPAR exocytosis during LTP, with non-kinase-related activity of CaMKII affecting actin dynamics via different mechanisms (Byth, 2014). Importantly, in terms of structural plasticity, there are two mechanisms via which CaMKII exhibits a structural function, both mediating the remodelling of the actin cytoskeleton within spines. Firstly, the assembly and disassembly of F-actin is mediated via direct binding of CaMKII to F-actin; in an inactivated state, CaMKII is bound to F-actin, but following activation CaMKII detaches. Secondly, the activation of numerous small GTPases is carried out by CaMKII. These small GTPases are responsible for activating ABPs, which mediate the remodelling of actin networks within spines via different mechanisms (Byth, 2014).

Small GTPases have various functions; Rac1 and Cdc42 mediating spine formation, growth, and maintenance, whereas small GTPase RhoA has a role promoting spine density and stability (Nishiyama, 2019). The activation of several downstream kinases is carried out by small GTPases, including that of p21-activated kinase (PAK) (Murakoshi et al., 2011). PAK activates serine/threonine LIM kinase (LIMK) proteins, including LIM kinase-1 (LIMK1) (Nikolić, 2008), which are important regulators of actin. PAK3 is a Rac1-activated PAK family kinase that phosphorylates and activates LIMK1. Mutations in LIMK1 in humans and knockout of LIMK1 in mice has been shown to cause dendritic spine abnormalities and cognitive impairment (Meng et al., 2002; Tassabehji et al., 1996; von Bohlen und Halbach, 2010), similarly to mutations in PAK3 (Boda et al., 2004). ABPs including cofilin and Arp2/3 that are essential in actin reorganisation have their activity modulated by LIMK1 (Meng et al., 2002). Cofilin regulates actin reorganisation in a phosphorylation-dependent manner, with its dephosphorylation leading to the severing of F-actin, and hence depolymerisation. LIMK1 phosphorylates cofilin at Ser-3 (Yang et al., 1998), which has been demonstrated in cultured cells to reverse this depolymerisation. Actin-related protein 2/3 complex (Arp2/3) promotes nucleation of actin polymerisation, and the branching of F-actin (Hotulainen & Hoogenraad, 2010)

The dynamic ability of dendritic spines to change in structure contributes to the processes of memory and cognition (Kasai et al., 2010; Segal, 2017), and defects in the morphology of spines has been linked to intellectual disability and neurodevelopmental disorders. Structural plasticity within spines is heavily dependent upon the correct localisation and regulation of all its protein components.

1.6.2 Localised Protein Synthesis in Synaptic Plasticity

Synaptic plasticity requires rapid turnover and remodelling of the dendritic proteome, through local activity-dependent changes in protein translation. Local translation of proteins can be observed in homeostatic plasticity, when rapid homeostatic scaling occurs following induced mini-NMDAR-blockade (Sutton et al., 2006). It has been demonstrated that in processes of Hebbian plasticity, compartmentalised gene expression and proteomic changes occur, allowing propagation of synaptic transmission to occur at a single stimulated synapse, without these changes occurring in neighbouring, unstimulated synapses (Müller & Connor, 1991). Detection of protein synthesising machinery and specific mRNA localisation in neuronal compartments provides evidence for local protein translation occurring at synapses.

Ribosomes are responsible for protein synthesis within cells, translating messenger RNAs (mRNA) into polypeptides. Numerous mRNA transcripts, as well as ribosomes (both individually and in clustered polysomes) have been found to be locally distributed in dendritic spines (Holt et al., 2019; Steward, 1997). MAP2 mRNA was the first mRNA shown to be locally distributed within neurons, being detected in distal dendrites using in situ hybridisation (Garner et al., 1988). The advancement of techniques to less biased approaches such as fluorescence in situ hybridisation (FISH), and microarray analysis and quantitative PCR, has allowed for hundreds of distally localised mRNA transcripts to be identified (Holt et al., 2019). Hundreds of mRNAs have also been shown to be enriched at presynaptic terminals, using purified synaptosome analysis. mRNAs can be translocated from their site of production, along dendrites to individual spines, where required translational machinery is located, and hence they can undergo local protein synthesis. Various factors regulate processes of expression, translocation, and protein translation and degradation. The 3'UTR on mRNA controls both localisation of mRNA via *cis*-acting sequences , and translation via actions of RNA-binding proteins that bind the 3'UTR (Meer et al., 2012; Yergert et al., 2021).

Local expression of protein machineries, and further synthesis of new polypeptides using these machineries, can be studied within spines. Translating ribosome affinity purity (TRAP) is a technique that has recently isolated over 2000 mRNAs undergoing local translation *in vivo*, in isolated embryonic and adult axons (Holt et al., 2019; Shigeoka et al., 2018). In hippocampal distal dendrites, using FISH with single-molecule imaging has allowed 'bursting' translation of local mRNAs to be detected in live cells (Wu et al., 2016). Locally synthesised synaptic and axonal proteins have successfully been directly visualised in situ using recent techniques such as fluorescence noncanonical amino acid tagging (FUNCAT) (Dieterich et al., 2010) and click-chemistry with fluorescent labelling.

Research into the α-subunit of CaMKII (CaMKIIa) and its mRNA transcript *CamKIIa* provide insight into the holistic importance of localised translation in neurons. *CamKIIa* is dendritically localised, and it has been demonstrated that its translation into CaMKIIa protein, in distal portions of the dendrite (up to 200 µm from the soma), can occur just 5 min after LTP has been induced (Ouyang et al., 1999). Local protein synthesis must occur, as the distance from the cell body to the site of protein translation is too far for neuronal protein transport to have occurred in such a small timeframe. The deletion of the *CamKIIa* 3'UTR – responsible for dendritic targeting of the mRNA – within a generated mouse model restricts *CamKIIa* to the soma, and furthermore cause a significant reduction in PSD-localised CaMKIIa protein (Miller et al., 2002). Mice with this mutation exhibit

defects in both late-phase LTP and impairments in spatial and object recognition memory, providing clear evidence that local dendritic translation is essential in both synaptic plasticity and its translation to animal behaviour (Miller et al., 2002).

Synaptic plasticity requires the local translation of many more regulatory proteins within neurons and importantly their dendritic spines. The identification of nascent polypeptides in neuronal compartments, that are fundamental in plasticity, has been achieved. For example, up-regulation in dendritic synthesis of LIMK1 can be caused using brain-derived neurotropic factor (BDNF), in cultured rat cortical neurons (Ravindran et al., 2019). Increased LIMK1 synthesis allows fine-tuning of the actin cytoskeleton within dendritic spines, leading to spine development. The repression of dendritic LIMK1 expression via NMDAR stimulation causes spine shrinkage (Rajgor et al., 2018).

The distribution of mRNAs and translational machineries such as ribosomes, and the subsequent regulation of protein synthesis via this spine compartmentalisation is essential in regulating mechanisms of synaptogenesis, neural circuit development, and importantly synaptic plasticity (Holt et al., 2019).

1.7 MiRNAs in the Brain

1.7.1 miRNAs and DDX6 in Alzheimer's Disease (AD)

LTD within the perirhinal cortex is critical in visual recognition memory, and one study has indicated that this form of memory becomes impaired early on in Alzheimer's Disease (AD), with LTD compromised at 3 months in AD-model mice (Tamagnini et al., 2012). Changes in miRNA profiles within human Alzheimer's AD patients, along with mouse models of the disease, have been identified (Liu et al., 2022). AD hallmarks include tauopathies and amyloid-β (Aβ) plaque deposition. The aggregation of Tau proteins within cells occurs in non-primary tauopathy in AD, and human brains displaying non-primary tauopathies have been shown to have altered expressions of RISC protein DDX6 (Chauderlier et al., 2018). Certain miRNAs have also been correlated with AD drivers, pathogenic Tau and amyloid-β (Wang et al., 2022). One study found, using tandem-affinity purification with mass spectrometry, that Tau and RISC protein DDX6 interact (Chauderlier et al., 2018). Through this interaction with DDX6, Tau was shown to increase gene silencing activity of multiple miRNAs including miRNA let-7, miR-21 and miR-124. Tau mutations disrupt Tau-DDX6 interaction and impair let-7a-mediated gene silencing.

1.7.2 The Role of S387 Phosphorylation, *in vitro*

Numerous miRNAs are responsible for changes in expression of synaptic proteins that occur following NMDAR stimulation, which leads to rapid spine shrinkage. The miRNA-134 (miR-134) is a key miRNA involved in regulation of structural plasticity (Schratt et al., 2006), with its multiple targets for repression including *Limk1* and *Pum2* (Fiore et al., 2009; Rajgor et al., 2018). Dendritic *Limk1* repression affects the cytoskeletal actin structures within dendritic spines, ultimately causing spine shrinkage. The mechanism of enhanced *Limk1* silencing via Ago2 phosphorylation at S387 was discovered to be specific to *Limk1*, with other miR-134 targets including *Pum2* unaffected by S387 phosphorylation (Rajgor et al., 2018). This study incorporated only the 3'UTRs of miRNAs in experiments, as this is where complementary binding with mRNAs usually occurs, hence specificity of this mechanism was also determined to be by the 3'UTR of the target mRNA .

Both miR-134 and miRNA miR-138 are enriched in dendrites and have roles in regulating dendritic spine morphology . The protein acyl-protein thioesterase 1 (Apt1), encoded by mRNA *Apt1*, is silenced via miR-138, and is responsible for the palmitoylation of proteins at synapses and negatively regulates dendritic spine size (Siegel et al., 2009). It has been previously shown that NMDAR stimulation rapidly increases translational repression of *Apt1* via miR-138, similarly to that of *Limk1* via miR-134, *in vitro*, using rat cortical neuronal cultures (Rajgor et al., 2017). However, the repression of *Apt1*, although regulated through NMDAR stimulation as *Limk1* was, was revealed not to be sensitive to the specific Akt-dependent phosphorylation of Ago2 at S387 (Rajgor et al., 2018). This suggests S387 phosphorylation only enhances silencing of a specific pool of neuronal genes, introducing a novel method of phosphorylation-dependent gene silencing regulation within dendritic spines. The phosphorylation of S387 has since been defined as a specific pathway for structural plasticity, as it is not involved in regulating AMPAR trafficking or LTD within the hippocampus (Rajgor et al., 2018).

Furthermore, Fathima Perooli in the Hanley lab investigated regulation of protein-mRNA binding events by S387 phosphorylation and DDX6 helicase activity using RNA-immunoprecipitation technique to determine changes in direct, physical protein-RNA binding. Data has shown that physical association of Ago2 with *Limk1* mRNA in rat neurons increases with the phosphomimic mutant Ago2-S387D and decreases with the phosphonull mutant Ago2-S387A. In contrast, Ago2-*Apt1* mRNA association was shown to be unaffected by S387 mutation (Perooli & Hanley, Unpublished Observations). RNA-immunoprecipitations also indicated an increase in endogenous DDX6 binding to *Limk1* mRNA, upon NMDAR stimulation, with DDX6 binding to *Apt1* unaffected.

DDX6 and its helicase activity were demonstrated to be essential for spine shrinkage, alongside S387 phosphorylation.

To develop our understanding of the mechanism of enhanced *Limk1* silencing via Ago2 phosphorylation at S387, an important next step would be to investigate this mechanism *in vivo* (or *ex vivo*). A first step would be to carry out similar experiments to those carried out by Fathima Perooli, using brain tissue rather than cultured neurons, to ascertain whether the same phenomenon observed in *in vitro* studies exist *in vivo*. Studies could then lead to determination of further genes regulated by this phosphorylation event *in vivo*, and further development in understanding how this phosphorylation may relate to a physiological manifestation of miRNA-dependent plasticity, such as in changing memory behaviours.

1.8 Aims and Objectives

Previous *in vitro* studies carried out in rat cortical neuronal cultures demonstrated that Akt-dependent phosphorylation of Ago2 at S387 regulates silencing of specific genes required for dendritic spine shrinkage. Increased translational repression of *Limk1* upon NMDAR stimulation was shown to be regulated via this mechanism, whereas increased repression of *Apt1*, although stimulated by NMDAR, was not regulated via this S387 phosphorylation (Rajgor et al., 2018). RNA-immunoprecipitations also proved increased DDX6-*Limk1* mRNA binding occurs, but not DDX6-*Apt1* mRNA binding, upon NMDAR stimulation.

To investigate whether the effects of Ago2 S387 (see S388 in mice) phosphorylation observed following NMDAR stimulations in cortical neuronal cultures can translate to animal models, S388A phosphonull mutant mice were created (see **Methods**).

The overarching aim of my project was to further define the role of Ago2 phosphorylation and subsequent DDX6 association in regulating RISC interactions and miRNA silencing. To determine whether previous *in vitro* findings can be translated to animal models, the aim of this study was to investigate how the same Ago2 phosphorylation event in mice at S388 influences the binding of both proteins Ago2 and DDX6 to the mRNAs *Limk1* and *Apt1*, using an *ex vivo* approach.

The objectives of this study were therefore:

- To optimise the immunoprecipitation of proteins of interest, Ago2 and DDX6, from mouse brain tissue using appropriate antibodies.
- To optimise the extraction of RNA from mouse brain tissue, using TRIzol, particularly when low amounts of RNA are present due to prior immunoprecipitation.
- To use an *ex vivo* approach of RNA-immunoprecipitation, to quantify differences between wild-type versus Ago2^{S388A} phosphonull mouse brain tissue, in Ago2 and DDX6 interactions with each other and with *Limk1* and *Apt1* mRNAs.

My hypothesis was that in the mutant S388A mouse, where S388 of Ago2 cannot be phosphorylated, less mRNA encoding LIMK1 would be repressed than in the wild-type, and hence would be indicated by reduced binding to RISC protein Ago2, and possibly also DDX6, which is also involved in RISC activity. This reduction would not be expected of the mRNA encoding Apt1, as repression of this mRNA is unaffected by Akt-dependent phosphorylation at this site (Rajgor et al., 2018).

2. Materials and Methods

2.1 Materials

2.1.1 Chemicals

Chemical reagents were purchased from Sigma-Aldrich, and solvents and acids from Fisher, unless otherwise stated.

2.1.2 Commonly Used Solutions

Solution	Solutes	Solvent
Co-IP Buffer	1% Triton X-100 (Sigma Aldrich) 150 mM NaCl (Sigma Aldrich) 20 mM HEPES, pH 7.4 (Sigma Aldrich) 1x Protease Inhibitor Cocktail Tablet (per 50 mL) (Sigma Aldrich) 0.1% β-mercaptoethanol (BME) (Acros Organics) 1:100 Phosphatase Inhibitor Cocktail 3	ddH_2O
RNA-IP Buffer	(as above, plus) 1:200 SUPERase•In™ RNase Inhibitor	DEPC- H_2O
Wash Solution (0.3 M Guanidine Hydrochloride)	0.3 M Guanidine Hydrochloride	95% EtOH in DEPC-H_2O
4X SDS (Laemli) Sample Buffer	200 mM Tris pH 6.8 (Thermo Fisher Scientific) 5% BME (Acros Organics) 50 mM EDTA (Sigma Aldrich) 8% SDS (Thermo Fisher Scientific) 40% Glycerol (Sigma Aldrich) 0.08% Bromophenol Blue (Sigma Aldrich)	ddH_2O
SDS-PAGE 8% Resolving Gel	375mM Tris-HCl pH 8.8 8% Acrylamide 0.1% SDS 0.1% Ammonium Persulfate (APS) 0.01% Tetramethyl-ethylenediamine	ddH_2O

	(TEMED)	
SDS-PAGE 5% Stacking Gel	125mM Tris-HCl pH 6.8 5% Acrylamide 0.1% SDS 0.1% APS 0.01% TEMED	ddH_2O
10X PBS	1.37 M NaCl (Sigma Aldrich) 27 mM KCl (Sigma Aldrich) 100 mM Na2HPO4 (Sigma Aldrich) 20 mM KH2PO4 (Sigma Aldrich) pH 7.4	ddH_2O
PBS-T	0.1% Tween (Sigma Aldrich)	1X PBS
10X SDS-PAGE Running Buffer	25 mM Tris (Thermo Fisher Scientific) 250 mM Glycine 0.1% SDS (Thermo Fisher Scientific)	ddH_2O
10X Transfer Buffer	24mM Tris (Thermo Fisher Scientific) 192 mM Glycine	ddH_2O (20% Methanol)
BSA (for Blocking)	Bovine Serine Albumin Fraction V	PBS-T/Co-IP Buffer
Ponceau Stain	0.1% Ponceau S 5% Glacial Acetic Acid	ddH_2O

Table 2.1: Commonly used solutions.

2.1.3 Electronic Equipment

- Heat Block (Eppendorf)
- Benchtop microfuges (Eppendorf, Biofuge)
- Centrifuges (Eppendorf, Avanti centrifuge)
- X-Ray film developer (SRX-101A)
- Real-time qPCR Machine (Stratagene Mx 3000P) (Agilent Technologies)
- Spectrophotometer
- Shakers and rotating wheel

2.1.4 Molecular Biology Reagents

- SUPERase•In™ RNase Inhibitor (20 U/µL) (Invitrogen™)
- Protein G Sepharose 4 Fast Flow Resin beads (Cytiva™)
- RNase*Zap*™ RNase Decontamination Solution (Invitrogen™)
- TRIzol™ Reagent (Invitrogen™)
- GlycoBlue™ Coprecipitant (15 mg/mL) (Invitrogen™)
- RevertAid First Strand cDNA Synthesis Kit (Thermo Scientific™)
- *Luciferase* Control RNA, 1 mg/mL (Promega)
- SYBR™ Green PCR Master Mix (Applied Biosystems™)

2.1.5 Protein Biochemistry Reagents

- PageRuler™ Prestained Protein Ladder (Thermo Scientific™)
- 30% Acrylamide 'Protogel' (National Diagnostics)
- Phosphatase Inhibitor Cocktail 3, in DMSO (Sigma-Aldrich®)
- cOmplete™ Protease Inhibitor Cocktail Tablets (Roche)
- Immobilon®-FL Polyvinylidene Difluoride PVDF Membrane (0.45µM pore size) (via Millipore)
- Filter Paper (GE Healthcare Life Sciences)
- Bovine Serum Albumin (BSA) Fraction V (Roche)
- CL-XPosure™ Film (Thermo Scientific™)
- Restore™ Western Blot Stripping Buffer (Thermo Scientific™)
- Protein Assay Dye Reagent Concentrate 'Bradford Reagent' (Bio-Rad)

2.1.5.1 Western Blotting Chemiluminescence Substrates

- SuperSignal™ West Pico PLUS Chemiluminescent Substrate (Thermo Scientific™)
- Immobilon Classico Western HRP Substrate (Millipore)
- Immobilon Crescendo Western HRP Substrate (Millipore)
- SuperSignal™ West Femto Maximum Sensitivity Substrate (Thermo Scientific™)

2.2.6 Primers

See **RT-qPCR methodology** section.

2.2.7 Antibodies

2.2.7.1 Primary Antibodies

Antibody	Animal	Supplier Conc.	WB Dilution [Solute]	Amount Used in IP	Cat. No.	Supplier
Ago2	Mouse	1 mg/mL	-	5 µg	018-22021	FUJIFILM Wako
Ago2	Rabbit	-	1:1000, [5% BSA]	-	50683-R036	SinoBiological
DDX6	Mouse	0.5 mg/mL	-	6 µg	11G10B39	Biolegend
DDX6	Rabbit	-	1:2000, [5% BSA]	-	A300-461A	(Fortis) Bethyl Laboratories
Ms-IgG	Mouse	3 mg/mL	-	5 or 6 µg	10400C	Invitrogen

Table 2.2: Primary antibodies used in WB and IP experiments.

2.2.7.2 Secondary Antibodies

Antibody	WB Dilution [Solute]	Cat. No.	Supplier
Rabbit IgG, HRP-linked whole Ab (from donkey)	1:10,000 [3% BSA]	NA934	Amersham ECL
Mouse IgG, HRP-linked whole Ab (from sheep)	1:10,000 [3% BSA]	NA931	Amersham ECL

Table 2.3 : Secondary antibodies used in WB experiments.

2.2 Methods

2.2.1 Transgenic Mice

2.2.1.1 Production

Transgenic animal use was approved by the Animal and Welfare Ethical Review Body at the University of Bristol. Initial generation of transgenic mice was carried out at MRC Harwell, via CRISPR-Cas9 gene-editing. Mouse embryos at 1-cell stage had an amino acid change introduced at Ago2 S388 via pronuclear injection of Cas9 protein, single guide RNAs and single-stranded oligodeoxynucleotides. Embryos were re-implanted into a pseudopregnant female mouse, and progeny bred with wild-type (WT) mice to produce heterozygotes (HETs). Homozygous Ago2 S388A mutants (HOMs) and WT mice colonies were produced through breeding HETs together. New generations of mice are genotyped often. To prevent excessive inbreeding and avoid introduction of unintended mutational phenotypes that could affect our findings, hybrid vigor was promoted occasionally, by crossing HOMs with WTs to produce new HETs, which are crossed back to form HOMs. Throughout, these 'WT' mice are referred to as '$Ago2^{WT}$', and 'HOMs' are referred to as '$Ago2^{S388A}$'.

2.2.1.2 Cortex and Hippocampus Extraction

Mice were culled either by cervical dislocation, or decapitation following deep anaesthesia using inhalational isoflurane, by other members of the Hanley lab. Brains were then quickly removed, with cortex and hippocampus dissected out, on ice. Tissue for use in final RNA work was snap-frozen using liquid nitrogen, and stored at -80 °C. Some tissue used in optimisation stages was only frozen on dry ice before storing at -80 °C.

It should be noted that only experiments using cortex tissue are presented throughout the **Results** and **Discussion** sections. Hippocampal tissue was used only in some early optimisation experiments that are not discussed.

2.2.2 Sample Preparation

2.2.2.1 Homogenisation

Snap-frozen cortex (CTX) or hippocampus (HPC) tissue was homogenised using a Dounce homogeniser, on ice. The Dounce was first sterilised with RNaseZAP, and washed with DEPC-H_2O, and any metal instruments were sterilised with 70% EtOH. Metal instruments were kept on ice or

dry ice before use. CTX was initially chopped into smaller pieces, on dry ice, and weighed. Tissue was then quick-washed with detergent-free Co-IP buffer, to remove any residual fluids. The first stroke (pressing down and twisting) was then carried out without buffer, for both CTX and HPC. Co-IP Buffer with detergent, with added protease inhibitor (1 tablet per 50mL) was used as lysis buffer. For every 1 µg of CTX tissue used, 10 µL of Co-IP buffer was added if using more than 0.05 g tissue, or 20 µL per 1 µg added if using less tissue (to avoid the loss of protein through production of bubbles). A further 9 strokes were then carried out following buffer addition. HPC tissue was not weighed, but for each whole HPC homogenised, 500 µL Co-IP Buffer was added, and 15 strokes carried out. Lysate was then transferred to a sterile, pre-cooled 1.5 mL microfuge tubes (Eppendorf), on ice. Additional phosphatase inhibitors (1:100 dilution) were then added to all lysates, with RNase inhibitor (1:200 dilution) and BME (0.1%) also added to lysates to be used in RNA work. Lysate was then incubated for 20 min on ice, inverting occasionally, before being spun down at 4 °C, 16,0000 g for 3 min to pellet insoluble cell debris. Supernatant was transferred to a new 1.5 mL microfuge tube and used immediately in downstream applications (or stored at -80 °C).

2.2.2.2 Bradford Assay

On ice, 5 BSA standards over a range of concentrations between 1-20 mg/mL (1, 2.5, 5, 10 and 20 mg/mL) were made up in Co-IP Buffer, from an initial stock of 100 mg/mL. BSA standards and tissue lysates were each diluted 1/10 in ddH_2O, and blank control of Co-IP Buffer only prepared in the same way. After addition of 20% Bradford Reagent (Bio-Rad) – diluted in ddH_2O – to each, 1.5 mL microfuge tubes were quickly shaken. Following a 5 min incubation at room temperature, mixtures were transferred to cuvettes. Using a spectrophotometer, optical densities at wavelength 595 nm were measured for each standard and lysate (in triplicate), with the blank control set as reference. A scatter graph of optical densities against BSA standard protein concentrations was plotted on Excel. Protein concentrations of tissue lysates were interpolated from the equation of a standard curve with an appropriate R^2-value (0.97 or above).

2.2.3 Immunoprecipitation (IP)

2.2.3.1 Co-Immunoprecipitations (Co-IPs)

Co-IPs were used to study interactions between endogenous RISC proteins, by precipitating one protein of interest and analysing co-precipitation of other proteins of interest. All steps were carried out on ice using pre-cooled 1.5 mL microfuge tubes, or at 4 °C where specified. Fresh tissue lysate

was diluted to 1-1.2 mg/mL in Co-IP Buffer containing protease and phosphatase inhibitors, to give a final volume of 500 µL per condition. An input of 5% was then taken. For Ago2 IP, DDX6 IP or a control condition to look at any non-specific interactions; 5 µg Ago2-Ms, 6 µg DDX6-Ms, or 5/6 µg Ms-IgG Ab was added, respectively. Where 'beads only' conditions were used, 1-1.2 mg/mL starting lysate was used with no Ab addition. Further Ab control conditions, using 500 µL of Co-IP Buffer without lysate, had 5 µg Ago2-Ms or 6 µg DDX6-Ms Ab added. All conditions were then incubated at 4 °C for 3 h, with gentle rotation on a rotary wheel, to allow for protein-antibody binding. Protein G Sepharose beads were washed 4x in 1 mL Co-IP Buffer to remove the 20% EtOH that they are stored in, each time centrifuging at 4 °C for 30 sec at 1000 rpm and discarding the supernatant by aspirating. Beads were then blocked in 0.1% BSA in Co-IP Buffer at 4 °C for 2 h, with gentle rotation. Following the 3 h incubation, 20 µL of blocked beads were added to each condition, and Co-IP Buffer was added to a final volume of 1 mL, to minimise non-specific binding. Conditions were returned to the rotating wheel for a further 1 h incubation, to allow for Ab-bead binding. Following Ab-bead incubation, beads were spun down at 4 °C for 30 sec at 1000 rpm. Supernatants (5%) were taken at this point if required, to test for IP efficiency. Beads were then washed 4x in 1 mL Co-IP Buffer, being spun down each time at 4 °C for 30 sec at 1000 rpm, and supernatant aspirated. Washes 1 and 4 were carried out by flicking/inverting, and washes 2 and 3 were longer 3 min washes at 4 °C, with gentle rotation on the wheel. After the final wash, 4X sample buffer (with 5% BME) was added directly to the beads and any proteins associated with them, for Western blotting.

2.2.3.2 RNA-Immunoprecipitations (RNA-IPs)

RNA-IPs were used to study changes in interactions between endogenous mRNAs and mRNA-binding proteins within RISC, by precipitating a protein of interest and then analysing differences in mRNA binding using TRIzol separation, Western blotting and qPCRs. RNA-IPs were carried out as described in the Co-IP section above, with the following changes in place. All 1.5 mL microfuge tubes and pipette tips were autoclaved, and any surfaces and equipment cleaned using RNaseZAP before use. RNase inhibitors and BME were also present in lysates used for RNA-IPs. SUPERase•In™ RNase inhibitor inhibits most common RNases, and the reducing agent BME irreversibly denaturing RNase enzymes by reducing disulfide bonds. Initial inputs of 1% and 10% were taken, rather than 5%. After the final wash, 4X sample buffer (with 5% BME) or TRIzol was added directly to the beads and any proteins and mRNA associated with them, for Western blotting or TRIzol isolation, respectively. 4X sample buffer was added to the 1% input which acted as a direct input, and TRIzol was added to the 10% input which acted as an indirect input. All other conditions had TRIzol added. *Luciferase* spike-in

control RNA was added to any TRIzol conditions that would later require qPCR analysis (IP, Ms-IgG and indirect input conditions), as described further in the TRIzol Reagent use section.

2.2.3.3 Pre-Clearing

In some experiments, a pre-clearing step would be taken to minimise any non-specific binding of lysate proteins to the Protein G Sepharose beads. To each 500 µL of 1-1.2 mg/mL fresh tissue lysate required, 20 µL worth of 4x washed, non-blocked Protein G Sepharose beads were added. Lysates were incubated for at 4 °C for 1 h, being spun at 14 rpm, for pre-clearing. Beads were then spun down at 4 °C for 30 sec at 1000 rpm. Supernatant was transferred to a new, pre-cooled, sterile 1.5 mL microfuge tube, and this pre-cleared lysate used as the starting lysate for Co-IP or RNA-IP as described above. Furthermore, to investigate proteins or mRNA bound non-specifically to the pre-clear beads, the beads were washed 4x in Co-IP Buffer and either 4X sample buffer or TRIzol added as described above.

2.2.4 Western Blotting

2.2.4.1 Sample Preparation

Protein samples (fresh or stored at -20 °C) in 4X sample buffer (with 5% BME) were heated for 10 min at 90 °C in a shaking heat block, prior to loading. A quick centrifuge spin was used to bring all sample to the bottom of the 1.5 mL microfuge tube and pellet any beads from the IP process.

2.2.4.2 SDS-PAGE (Sodium dodecyl sulphate-polyacrylamide gel electrophoresis)

Protein samples were resolved using SDS-PAGE, separating proteins based upon their molecular weights. Bio-Rad Mini-PROTEAN apparatus was used to carry out the electrophoresis process. Hand-made polyacrylamide gels of 8% were used, based upon the molecular weights of the proteins of interest Ago2 (97kDa) and DDX6 (54 kDa). Gels were cast within 1.5 mm glass plates, first cleaned with 70% EtOH. 8% resolving gel solution and 5% stacking gel solution was made up (see **Materials** for recipe), without TEMED added. TEMED was then added when required to the resolving gel solution, and after inverting to combine all components, 7.5 mL of resolving gel solution was quickly poured between the plates. Isopropanol was then instantly added on top, to remove any bubbles and allow for a level interface for proteins to stack upon. Once the resolving gel had polymerised (~10 min), isopropanol was removed and washed off using ddH_2O. TEMED was added to the stacking

gel solution, and after inverting to combine all components, ~2.5 mL was poured over the resolving gel, to the top of the glass plates, with a 1.5 mm 10- or 15-well comb quickly added to allow wells to form upon gel setting. Following stacking gel polymerisation (~30 min), the gel was either used immediately or stored overnight at 4 °C, wrapped in clingfilm to avoid drying out. Gel plates were fitted into a Bio-Rad electrophoresis system, and the comb was carefully removed once wells 1x SDS-PAGE running buffer had been added up to a level where wells were immersed. Proteins samples (20 µL) were added to wells using a pipette, and 3 µL of pre-stained protein ladder added to at least one well to aid in molecular weight estimation. Protein sample volume used was the equivalent of 50% of total IP protein loaded into the IP well, for a given Western Blot. Gel loading pipette tips could not be used when pipetting in IP samples, due to the presence of large Sepharose beads. An appropriate volume of 1x SDS-PAGE running buffer was then added to the tank, based on the number of gels running (half-filled for 1-2 gels, and fully filled for 3-4 gels). Gels were run at 80V until proteins had stacked at the interface between gels, and a visible separation of protein ladder bands had occurred. Voltage was then increased to 120 V as proteins were run through the resolving gel, until the dye front either reached the bottom of the gel or ran off.

2.2.4.3 Wet-Transfer and Drying

Immobilon-FL PVDF membrane with 0.45 µm pores was used during transfer, which bind proteins via hydrophobic interactions. Stacking gels and any remaining dye front was discarded, and the resolving gel then equilibrated in 1x SDS-PAGE transfer buffer for 2 min. Sponges and filter paper was also pre-soaked in 1x transfer buffer, to carry out a wet-transfer. PVDF membrane was activated in methanol for 30 s and quickly washed in transfer buffer. Forceps were used to handle the membrane at all times to avoid any contaminating protein transfer. A transfer sandwich was then assembled in a transfer cassette as follows: sponge, 4x filter papers, gel, activated membrane, 3x filter papers, and a sponge. A roller was used throughout the assembly to remove possible bubbles that would interfere with the transfer. The cassette was then tightly closed and placed between electrodes, with the gel next to the cathode and membrane next to the anode. The tank was then filled with 1x transfer buffer, and proteins were transferred to the PVDF membrane at a constant current of 400 mA for 60 min, with an ice pack and constant magnetic stirrer utilised to reduce temperature increase over this time. Following transfer, membranes were air-dried for 10 min, to help increase protein binding and reduce background.

2.2.4.4 Immunoblotting

Dried membranes were reactivated in methanol for 30 s and washed quickly in PBS-T. Membranes were then blocked at room temperature for 1 h in 5% BSA in PBS-T, with gentle shaking. Working stocks of primary antibodies were made up in advance in 3% or 5% BSA in PBS-T, and 0.02% sodium azide added to avoid contamination and allow for longer-term storage at 4 °C. Primary antibody working stocks were reused until poor chemiluminescence detection occurred. Blocked blots were cut at 70 kDa and incubated protein-side up with appropriate primary antibodies overnight at 4 °C, with gentle agitation on a roller. After 1x quick wash and 3x 5 min PBS-T washes to remove any unbound proteins (and importantly to remove sodium azide, as this is an HRP inhibitor), blots were incubated at room temperature in appropriate HRP-conjugated secondary antibodies in 3% BSA in PBS-T, with gentle rocking for 1 h. Secondary antibody was then discarded, and a 1x quick wash and 3x 10 min PBS-T washes carried out, to remove unbound antibody and minimise background.

2.2.4.5 Chemiluminescence Detection

To visualise antibody-labelled proteins of interest, chemiluminescence detection was utilised. Blots were incubated for 2 min protein-side down in 0.5-1 mL (depending on blot size, to provide full coverage) of a HRP chemiluminescent substrate of appropriate strength (**Table 2.4**).

Substrate	Supplier	Strength
Pico	Thermo Fisher Scientific	1
Classico	Millipore	2
Crescendo	Millipore	3
Femto	Thermo Fisher Scientific	4

Table 2.4 : HRP chemiluminescent substrates. *In order of strength, and with supplier listed.*

Blots were then transferred protein-side up, either to a Licor plate with an acetate sheet placed on top to be imaged using an Odyssey FC Imaging System (LI-COR Biosciences), or to a developing cassette between plastic sheets for exposure to CL-XPosure™ Film (Thermo Fisher Scientific) using a dark room developer. Using the Licor, a 2-5 min exposure was used. X-ray film was generally used following TRIzol use in RNA-IPs, due to lower signals given using the Licor, and film exposure ranged from 1 sec to 15 min depending on signal intensity. If no signal was shown, blots were washed 3x in

PBS-T before repeating incubation with a substrate of higher strength. Developed film was then scanned and saved as a .jpg file, both with 0 contrast and a contrast of 30. Contrast 30 scans were then imported as third-party images to Image Studio Lite Ver 5.2, and data inverted. Quantification of blot signals from both the Licor or dark room was carried out on Image Studio, using the add rectangle tool to select and quantify signal intensity. A user-defined background was subtracted, and further densitometry analysis carried out, normalising as required for individual experiments.

2.2.4.6 Stripping Blots and Re-Probing

Any blots that required re-probing were stripped using Restore stripping buffer (Thermo Scientific). Following chemiluminescence detection, blots were washed 3x in PBS-T to remove any remaining substrate. Blots were then submerged protein-side up in stripping buffer and incubated for 10 min at room temperature with gentle shaking, to remove primary and secondary antibodies. Stripping buffer was then discarded, and 3x PBS-T washes of the membrane carried out over the course of 1 h, following an initial 1x quick wash. Blots were then air-dried and stored in plastic at 4 °C. Stripped membranes could then be reactivated and blocked when required, as described above.

2.2.4.7 Ponceau Staining

Ponceau staining can be used to rapidly visualise any protein on the membrane following the transfer stage, as it stains any proteins present a pink-red. This technique was used during some optimisation steps to quickly indicate if protein had been isolated successfully following TRIzol use. Once reactivated in methanol, membranes were submerged protein-side up in Ponceau S stain and incubated at room temperature for at least 5 min, with gentle rocking. To destain the membrane after protein visualisation, 1x quick wash in ddH2O followed by 3x 10 min washes in PBS-T were carried out, until as much of the stain as possible was removed. Blocking and further steps can then be carried out as usual, without interference from this stain.

2.2.5 TRIzol Reagent Use

2.2.5.1 Phase Separation

Use of TRIzol reagent allows both RNA and protein to be isolated directly from tissue or extracted from protein beads in an RNA-IP sample. All 1.5 mL microfuge tubes and pipette tips were autoclaved, and any surfaces and equipment cleaned using RNaseZAP before use. All steps were

performed on ice unless otherwise stated, with sterile 1.5 mL microfuge tubes pre-cooled. TRIzol reagent was used to isolate protein and RNA from tissue lysates, following an adapted procedure from Invitrogen™. Using a starting sample of 50 µL or less, 500 µL of TRIzol Reagent used for lysis was added, along with 1 µL of exogenous *luciferase* spike-in control RNA (Promega, 1:25 dilution). *Luciferase* RNA was used as a control here, as usual endogenous housekeeping genes do not associate with RISC in a manner that allows them to be used in downstream normalisation. Samples were usually left overnight at 4 °C, at this stage, before continuing with the procedure, or incubated for 5 min at 4 °C to allow for complete 47dissociation of nucleoprotein complexes. Following addition of 150 µL chloroform, samples were thoroughly mixed by shaking for 10 sec, and incubated for 3 min. Samples were centrifuged for 15 min at 12,000 g at 4 °C, to separate into an upper RNA-containing, colourless aqueous layer, a white interphase, and a lower protein-containing, red phenol-chloroform layer.

2.2.5.2 RNA Isolation

RNA was isolated by first transferring 200 µL of the upper aqueous layer to a new 1.5 mL microfuge tube. This step must be carried out extremely carefully, as taking up any of the DNA-containing interphase or lower TRIzol-containing phase makes the following RNA isolation non-viable for downstream applications, as contaminants can interfere with these processes. To help with pellet visibility, 2 µL RNase-free Glyco-Blue co-precipitant (Invitrogen™) was added. RNA was then precipitated as a pellet by adding 400 µL isopropanol, incubating for 10 min at 4 °C and then centrifuging for 10 min at 12,000 g at 4 °C. A moving pellet at this point indicates that DNA or phenol has been taken up in the previous step, and that the sample will not be useable in downstream qPCR due to contamination. Supernatant was discarded and RNA pellets were then washed 3x in 0.5 mL ice cold 75% EtOH (diluted in DEPC-H_2O), centrifuging at 7500 g at 4 °C for 5 min, each time. After the final wash, supernatant was discarded, and RNA pellets air-dried at room temperature for a minimum of 20 min, until they looked fully dry. It is important that pellets are fully dry as leftover EtOH may cause contamination and interfere with downstream processes, but pellets should not be overdried as this will cause issues with re-solubilisation of the pellet. RNA pellets were then resuspended in 20 µL DEPC-H_2O and solubilised by incubating in a shaking heat block for 10 min at 60 °C and pipetting up and down. Total RNA yield and purity was determined using a NanoDrop™ Spectrophotometer (Thermo Scientific), and ND-1000 V3 program. A blank reading was taken using Glyco-Blue-containing DEPC-H_2O. Absorbances at wavelengths 230, 260 and 280 nm were taken for each RNA sample, providing A260/280 ratios and A260/230 values. Pure RNA with negligible protein contamination present should give an A260/280 ratio of ~2.0. The A260/230 value should also be

~2.0, with values <1.8 indicating a high absorbance at 230 nm, and hence signalling that there may be significant organic contamination (e.g. EtOH or phenol) present that could interfere with downstream reverse transcription. See **optimisation chapter** for further information. RNA samples were then stored at -80 °C.

2.2.5.3 Protein Isolation

To isolate proteins, aqueous and inter- phases were removed, and 150 µL 100% ethanol added to the phenol-chloroform layer. After inverting and incubating for 3 min, 750 µL isopropanol was added and samples incubated for 10 min, before centrifuging at 12,000 g at 4 °C for 10 min to pellet proteins. Protein pellets are difficult to see at this point, but assumed to be on the side of the 1.5 mL microfuge tube that was facing outward during centrifugation. Supernatant was carefully aspirated from the opposite side of the 1.5 mL microfuge tube. Pellets were then washed 3x in 1 mL wash solution (0.3M guanidine hydrochloride in 95% ethanol), and 1x in 1 mL 100% ethanol, each wash consisting of a 20 min incubation followed by centrifuging for 5 min at 7500 g at 4 °C. After the final wash, supernatant was discarded, and the pellet immediately resuspended in 40 µL of 4X sample buffer with 5% BME, taking care not to let pellets dry out at all. Samples were then incubated at 90 °C for 10 min in a shaking heat block, for downstream Western blot use. Samples were stored at -20 °C.

2.2.5.4 cDNA Preparation

First strand cDNA synthesis was carried out using RevertAid (Thermo Scientific) protocol, as follows. All reagents were stored at -80 °C. The following reaction was prepared in an RNase-free microfuge tube, on ice. RNA isolated using TRIzol was first diluted using nuclease-free H_2O as required to an 11 µL final volume (total RNA should be 0.1 ng – 5 µg, as per protocol), usually with 5-6 or 11 µL RNA used. Then 1 µL Oligo (DT)18 primer was added, which consists of 12–18 deoxythymidines bases and detects mRNAs with a poly-A tail. After brief centrifugation and 5 min incubation at 65 °C, samples were placed on ice for 1 min, and then briefly centrifuged to bring down any water condensed on the lid. The following was then added to the 12 µL reaction mix: 4 µL 5X Reaction Buffer, 1 µL RiboLock RNase Inhibitor (20 U/µL), 2 µL 10 mM dNTP Mix and 1 µL RevertAid M-MuLV RT (200 U/µL). After brief centrifuging, a reverse transcription reaction was carried out, incubating at 42 °C for 60 min, and terminating by heating at 70 °C for 5 min. The produced cDNA was then used immediately in a qPCR, or stored short-term at -20 °C.

2.2.5.5 Reverse Transcription Quantitative Real-Time PCR (RT-qPCR)

2.2.5.5.1 RT-qPCR Methodology

Real-time mRNA amplification was analysed by quantitative PCR, using PowerUp SYBR® Green PCR Master Mix (Applied Biosystems™), to investigate relative mRNA interactions. In triplicate, for each primer pair (*Luciferase*, *Limk1* or *Apt1*) used, 2 µL of produced cDNA was added to a mix of 10 µL SYBR Green, 0.5 µL forward primer, 0.5 µL reverse primer and 7 µL DEPC-H_2O, and briefly centrifuged. Working stock concentration of all primers was 10 µM, so 0.25 µM final concentration of each was used. The primers used and their target genes are shown **Table 2.5**. No primer controls contained no primer and were not performed in triplicate.

Gene	Primer Name	Sequence	Primer Length (Base Pairs)
Limk1	F	5'-AGT GCA TGA GGT TGA CGC TA-3'	20
	R	5'-GGA GGT ACT GGC CGT CAT AG-3'	20
Apt1	F	5'-GCC CTT ACC ACA CAG CAG AAA C-3'	22
	R	5'-TCA GGG GAA CCA AAG GGT CAC-3'	21
Luciferase	F	5'-AGA GAT ACG CCC TGG TTC CT-3'	20
	R	5'-ATA AAT AAC GCG CCC AAC AC-3'	20

Table 2.5: Primers used in RT-qPCRs.

Sequences and lengths both forward and reverse Limk1, Apt1 and Luciferase primers

PCR amplification was performed using a Stratagene PCR machine for 40 cycles with the following thermal profile set-up:

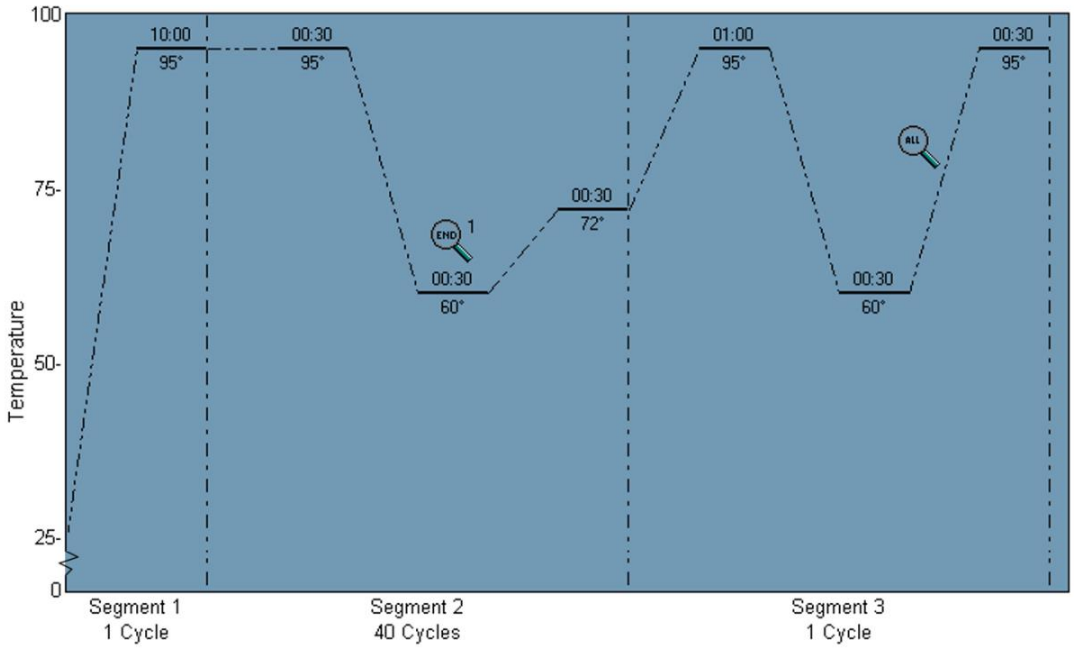

Figure 2.2: Illustration of the thermal profile set-up for RT-qPCRs.
(Screenshot from Stratagene Mx 3000P qPCR system, provided by Agilent Technologies)

	Temperature (°C)	Time	No. of Cycles
Segment 1	95	10 min	1
Segment 2	95	30 sec	40
	60	30 sec	
	72	30 sec	
Segment 3	95	1 min	1
	60	30 sec	
	95	30 sec	

Table 2.6: Overview of thermal profile set-up for PT-qPCRs.
Segment cycles, temperatures, and timings.

A fluorescent signal is produced by SYBR Green during the RT-qPCR assay, as cDNA is amplified. Fluorescence occurs when SYBR Green is bound specifically to double-stranded DNA (dsDNA), and not when unbound or bound only to single-stranded DNA (ssDNA). Cycle threshold (Ct) values indicate the number of amplification cycles required for a certain level of fluorescence signal to be detected. Ct values based upon SYBR Green dissociation curves were provided by an MxPro programme, using a programme-determined and assay-specific threshold. 'No Ct' value indicates that the determined threshold for fluorescence was not reached within the 40 cycles of Segment 2. Ct values too close to 40 are less reliable and would suggest that more RNA should be used in the initial cDNA preparation step.

Intercalating dyes such as SYBR Green are not sequence-specific. It is important to confirm specificity, by both confirming amplicon homogeneity and determining whether primer dimer formation occurs. To do so, after amplification cycles are completed, the thermal cycler continues to increase the temperature, which causes dsDNA to denature and dye to dissociate, and hence fluorescence to decrease. This fluorescence decrease is measured over time and allows a dissociation (melting) curve to be produced by the programme. The peak indicates when the primer has become single-stranded, with a single peak evidencing a single, pure amplicon produced during the assay. Multiple peaks may suggest multiple amplicons produced or the formation of unwanted primer dimers. Specificity of primers used was validated (**Fig2.2**).

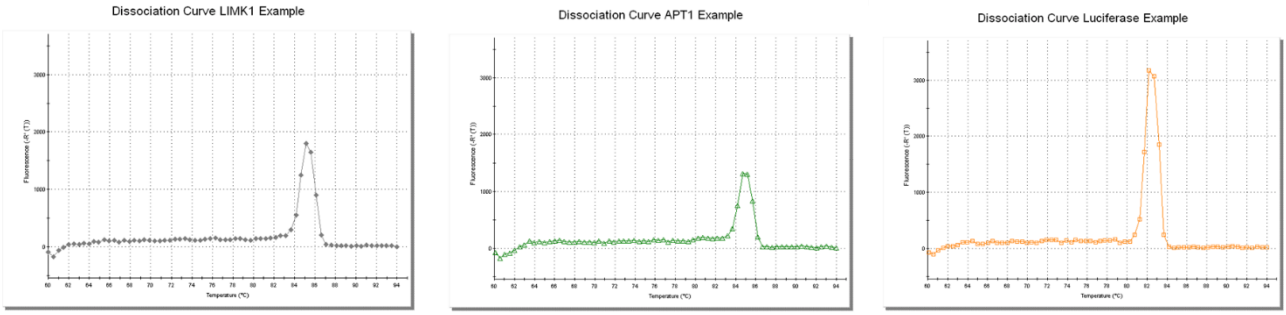

Figure 2.3: Exemplar dissociation curves for Limk1, Apt1 and Luciferase. *Curves provide validation of primer specificity in each case, as a single peak is present for each primer pair, indicative of pure singular amplicon production.*

2.2.5.5.2 RT-qPCR Analysis

Average Ct values were determined from triplicated repeats, for each reaction. A ΔΔCt method was then used to quantify relative interaction levels between mRNAs of interest and a protein of interest, after normalising to *luciferase* levels, as follows:

$$\Delta Ct = Mean\ Ct\ (Limk1\ or\ Apt1\ mRNA) - Mean\ Ct\ (Luciferase\ Control\ mRNA\ )$$

$$\Delta\Delta\text{Ct} = \Delta Ct\ (Immunoprecipitated\ Ago2\ or\ DDX6) - \Delta Ct\ (Input)$$

$$Relative\ association\ or\ interaction\ level = 2\text{^}(-\Delta\Delta Ct)$$

Relative interaction levels from the RT-qPCR analysis for each mRNA of interest were then normalised to protein data. Protein signal intensities were measured using Image Studio Lite Ver 5.2 from Western blots, as described in the 'Chemiluminescence Detection' section above. Relative interaction levels were first divided by their associated protein signal (either the direct input or the immunoprecipitated Ago2 or DDX6, corrected for controls), and then Ago2^{WT} an Ago2^{S388A} data was all normalised to Ago2^{WT}, such that Ago2^{WT} = 1.

2.2.5.5.3 Statistical Analysis

For the statistical comparisons of Ago2^{WT} vs Ago2^{S388A} data, where experimental repeats of 3 of more were carried out, a two-tailed, unpaired student's t-test was utilised, with an alpha of 0.05. Standard error of the mean (SEM) was indicated as error bars on column graphs where applicable, with non-statistically significant difference indicated as 'ns' above bars. Boundaries of ±2.5 standard deviation (SD) from the mean were used for detection of outlier values within repeats. Where technical repeats of only 1 or 2 were carried out, notably within that of optimisation data, only descriptive statistics were utilised as inferential statistical tests could not be used. Ct-value analysis including SD calculations were carried out in Excel, and further statistical testing and graphing carried out in GraphPad Prism (Version 9.5.1).

3. Results

3.1 The Trials and Tribulations of TRIzol and Tissues

3.1.1 RNA Purity and Contamination

As the isolation of RNA is necessary for downstream RT-qPCR, from which Ct-values are used directly in the analysis of protein-mRNA interactions, it was important that these Ct-values were not being impacted by the presence of any contaminants in samples of isolated RNA. It was important to determine which steps during the TRIzol isolation of RNA could bring in factors of contamination and in turn to make optimisations to the original protocol. It was also of interest to determine how small amounts of starting material for this isolation impact the ability of our NanoDrop™ Spectrophotometer and ND-1000 V3 program to detect total RNA concentrations as well as absorbance ratios.

As described in the methods section, when looking at TRIzol-isolated RNA, purity was determined by looking at A260/230 and A260/280 ratios calculated from absorbance graphs for each sample. Pure RNA with negligible protein contamination present should give an A260/280 ratio of ~2.0; values of less than 1.8 or higher than 2.2 were initially determined to be out of an acceptable range. Pure RNA should also have an A260/230 value ~2.0, with values <1.8 indicating a high absorbance at 230 nm, and hence signalling that there may be significant organic contamination (e.g. EtOH or phenol) present that could interfere with downstream reverse transcription; values of <1.8 were therefore initially determined to be out of an acceptable range.

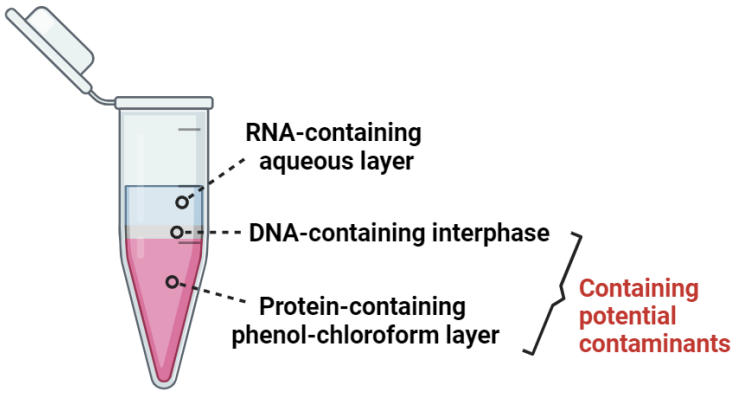

Figure 3.4: Simple schematic of TRIzol phase separation. *Distinct layers are provided during phase separation using TRIzol Reagent. Bottom layers contain potential contaminants. (Created using BioRender)*

During phase separation using TRIzol reagent, the addition of chloroform causes the separation of the sample into three distinct layers: a colourless RNA-containing aqueous layer, a white DNA-containing interphase, and a lower protein-containing, red phenol-chloroform layer (**Fig3.1**). Only the top aqueous layer is desired in the following step of RNA isolation.

However, with smaller amounts of starting material the interphase is very difficult to see, hence DNA can be taken up as an unwanted contaminant with the RNA. When attempting to precipitate RNA as a pellet, it is easy to identify when DNA is present, as the pellet floats rather than adhering to the side of the microfuge tube. Similarly, the lower phenol, protein-containing bottom layer can also contaminate the aqueous layer. This is indicated more clearly during the step itself, as the pipetting up of a red layer can be easily observed. In cases where it was known the phenol layer had been taken up, all the pipetted sample was added back to the microfuge tube and samples were re-spun and re-separated as in the phase separation method, before carefully transferring the top layer as per the RNA isolation method.

Part 1 aims to optimise TRIzol reagent protocol for smaller starting amounts of tissue. Sample volume should not exceed 10% of the volume of TRIzol reagent being used in lysis (as per reagent protocol), and since 500 µL of TRIzol is used following immunoprecipitations in the RNA-IPs carried out, this meant 50 µL of lysate could be used in optimising TRIzol use. All immunoprecipitations at the beginning of RNA-IPs were carried out using a starting lysate volume of 500 µL, with a protein lysate concentration of ~1 mg/mL, meaning an initial ~500 µg of total protein was present before the immunoprecipitation of the Ago2 or DDX6 was carried out. Considering this, when carrying subsequent optimisation steps, an initial highest protein mass of 400 µg was used. For all optimisation experiments, 50 µL of starting lysate was used, using additional Co-IP buffer to dilute to required amount of 'starting protein'. Total 'starting protein' amounts and their corresponding concentrations are shown in **Table 3.1**.

Total 'Starting Protein' in 50 µL (µg)	Starting Total Protein Concentration (mg/mL)
400	8
200	4
100	2
50	1
25	0.5
10	0.2
5	0.1
1	0.02

Table 3.1: Total 'starting protein' used in optimisation experiments, with corresponding total protein concentrations

3.1.2 Phase Separation: Additional Chloroform Step

From the initial protocol, total RNA values were shown to increase as starting protein was increased (**Fig3.2A**), as would be expected. A260/280 values were also all within an acceptable range, but A260/230 values were all below 1.0 indicating possible organic contamination (**Fig3.2B**).

Organic contamination can occur through accidental phenol uptake. To consider whether a secondary chloroform addition following initial transfer of the aqueous layer could potentially spin-down contaminants in a way that allows a non-contaminated supernatant to then be taken, the following was carried out: 150 µL chloroform was added to the previously transferred aqueous layer, vortexed for 30 s and then centrifuged for 2 min at 14,000 g at 4 °C, before transferring the supernatant to a new microfuge tube and continuing with RNA isolation. The results for this experiment indicated that this additional step was in fact detrimental to the RNA-isolation process, providing even lower A260/230 values and strangely causing an increase in A260/280 values to 2.4 and above, outside of the range considered to be acceptable (**Fig3.2D**). This secondary chloroform addition was not used in further experiments.

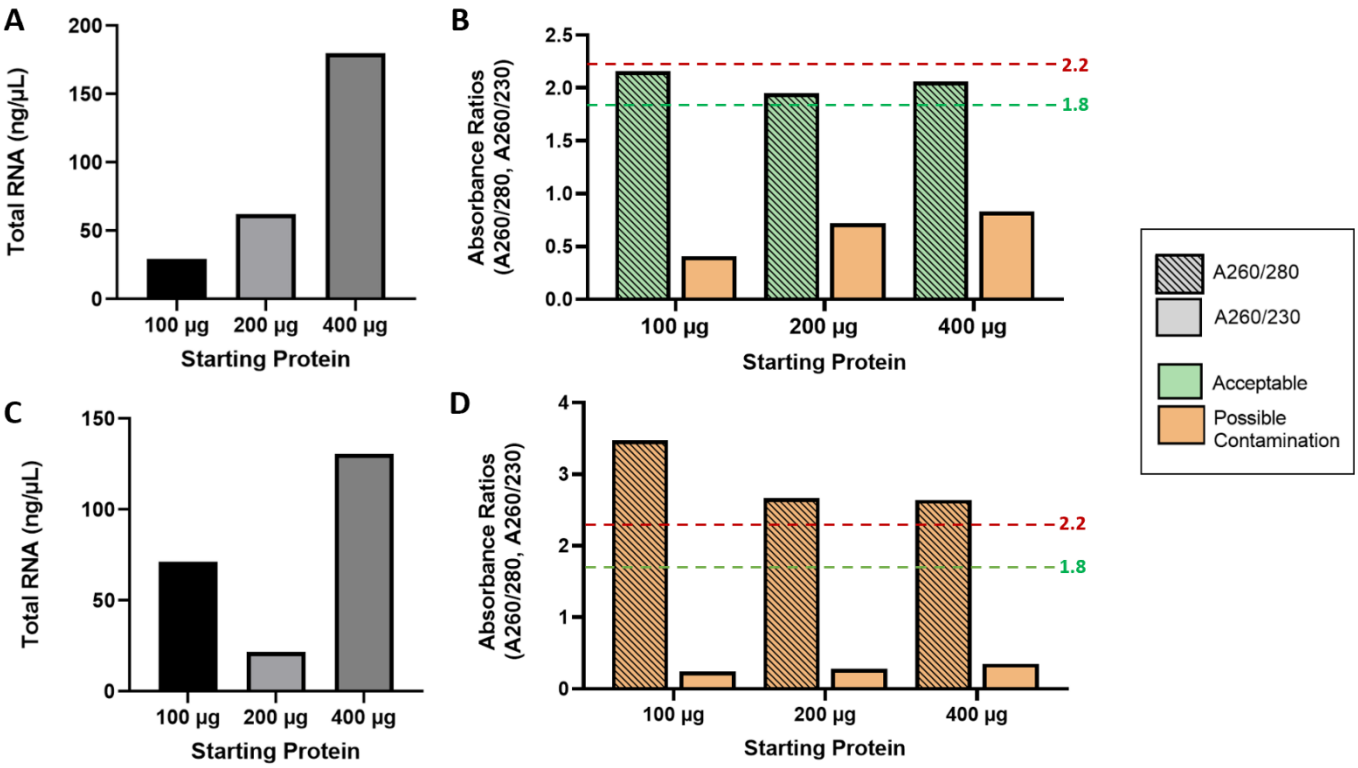

Figure 3.5: Nanodrop readings from TRIzol-isolated RNA using 100-400 µg of starting protein from mouse CTX, following initial protocol versus protocol with a secondary chloroform addition. (A) *and* ***(B)*** *show results from an initial TRIzol isolation following original protocol (n=1), and* ***(C)*** *and* ***(D)*** *show results following the same protocol with a secondary chloroform addition in the phase separation step (n=1).* ***(A)*** *and* ***(C)*** *show total RNA (ng/µL).* ***(B)*** *and* ***(D)*** *show read-outs of A260/280 and A260/230 ratios. Green bars indicate that ratios are within an 'acceptable' range, whereas orange bars indicate that values are not within this range and therefore possible contamination may be present. Lowest acceptable threshold of 1.8 is indicated by a green dashed line, and highest acceptable threshold of 2.2 indicated with a red dashed line. [NB: Experiments were not run alongside one another/from the same starting material so may not be considered directly comparable.]*

3.1.3 Phase Separation: Aqueous Layer Uptake

During phase separation, according to the original TRIzol Reagent product protocol (Invitrogen™), transferring any of the interphase or organic layer into the pipette during aqueous phase removal should be avoided, as it could cause contamination as previously described. Using caution at the beginning of experimentation, 150 µL of the aqueous layer was transferred to a new microfuge tube

each time, as this volume ensured that it was easy to see where the interface was between the aqueous layer and lower layers. However, taking up smaller volumes of the available aqueous layer to avoid contamination would result in isolation of lower amounts of RNA for downstream applications.

To understand how taking larger amounts of this aqueous layer affects both total RNA and A260/280 and A260/230 ratios, TRIzol isolation was carried out using starting protein of 50-400 µg, taking 150 µL of the aqueous layer and then taking the maximum volume of aqueous layer available (whilst still avoiding the bottom layers) (**Fig3.3**).

It should be noted that the 'maximum' volume was relatively arbitrary here, as although it should optimally be the same volume across all conditions, volumes differed slightly due to avoiding taking up the bottom layers. However, the volume of available aqueous layer was roughly 250-300 µL, for any given condition. Results indicated that at starting protein amounts of 200 µg and 400 µg, total RNA concentration remained unchanged (**Fig3.3A**). However, taking a larger amount of aqueous layer at a starting protein of 50 µg almost halved the RNA concentration, and conversely at a starting protein of 100 µg taking a larger amount of aqueous layer almost doubled the RNA concentration. A260/280 values remained practically unchanged at all starting proteins, taking 150 µL versus maximum aqueous layer, all remaining within an acceptable range (**Fig3.3B**). On the other hand, taking a larger amount of aqueous layer improved the A260/230 values for all amounts of starting proteins, although still not to what would usually be considered within an 'acceptable' range. Due to this result, 200 µL of the aqueous layer was taken for each condition rather than 150 µL in further experiments, to improve A260/230 values whilst also still minimising the potential uptake of bottom layers, and maintaining the volume transferred the same between conditions. It is difficult to conclude from this single experiment that the volume of aqueous layer transferred affects to the RNA sample, especially with regards to total RNA when higher initial starting protein amounts are used.

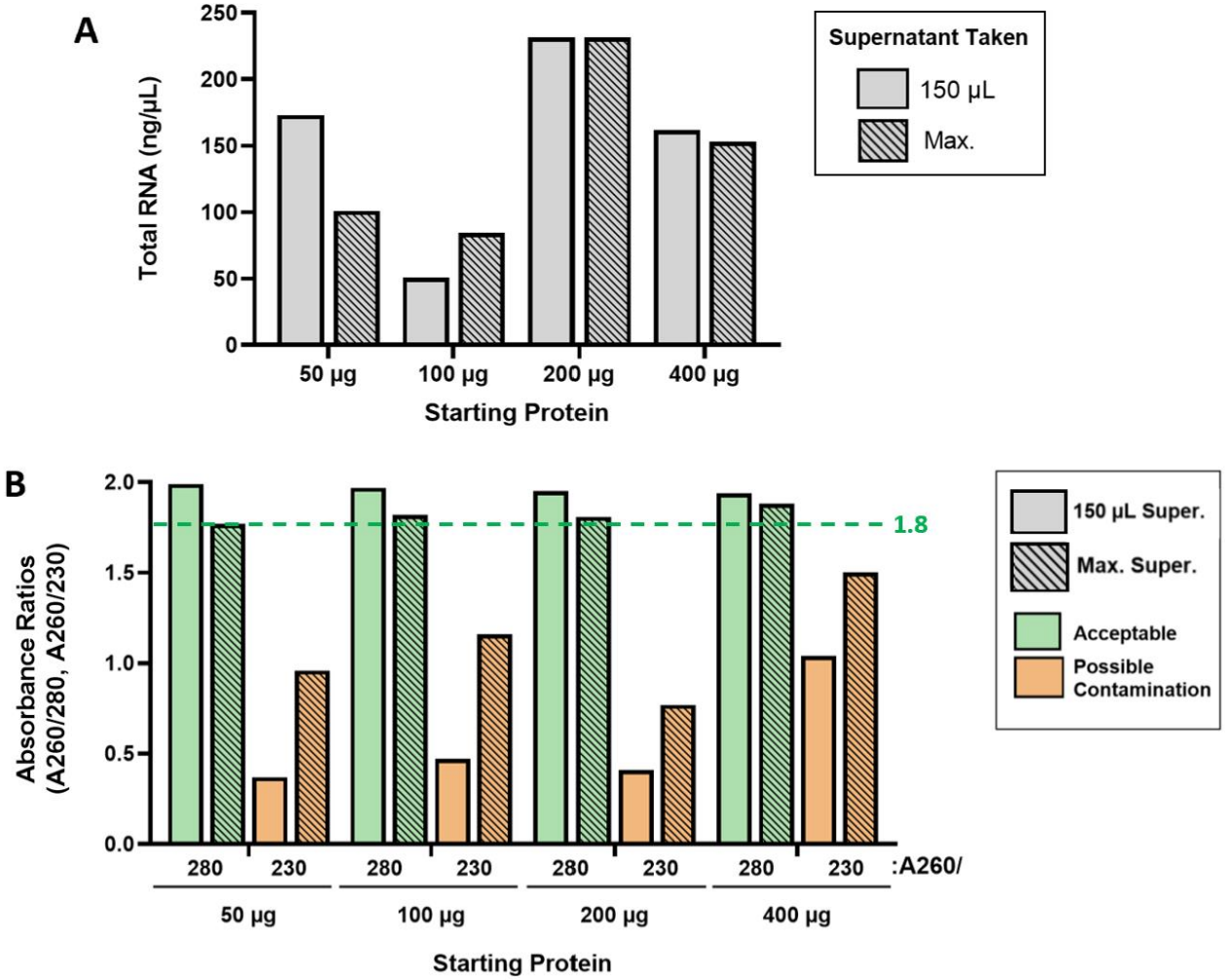

Figure 3.6: Nanodrop readings from TRIzol-isolated RNA, taking 150 µL of aqueous layer versus maximum amount of aqueous layer in the phase separation step of TRIzol reagent use, using starting protein of 50-400 µg mouse CTX. (A) *shows total RNA (ng/µL).* ***(B)*** *shows read-outs of A260/280 and A260/230 ratios. Green bars indicate that ratios are within an 'acceptable' range, whereas orange bars indicate that values are not within this range and therefore possible contamination may be present. Lowest acceptable threshold of 1.8 is indicated by a green dashed line. (n=1)*

3.1.4 Nanodrop Use: Blanking

Originally, DEPC-H_2O was used as a blank for Nanodrop readings. A260/230 values of below 1.8 are indicative of potential organic contamination, and as organic Glyco-Blue was added to RNA samples as a co-precipitant to improve pellet visualisation it was important to see whether using the same concentration of Glyco-Blue in the blank affects A260/280 ratios.

Results indicated that in this instance for the same RNA sample, addition of Glyco-Blue to the blank slightly increased the A260/230 ratios (**Fig3.4B**), bringing them closer to 2.0, with A260/280 ratios remaining unchanged. Glyco-Blue in the blank also caused slightly decreased readings in total RNA (**Fig3.4A**). Although not entirely conclusive, Glyco-Blue was used within the blank in further experiments, to make sure that chemically, the solution used to blank was as similar as possible to that used to re-solubilise isolated RNA.

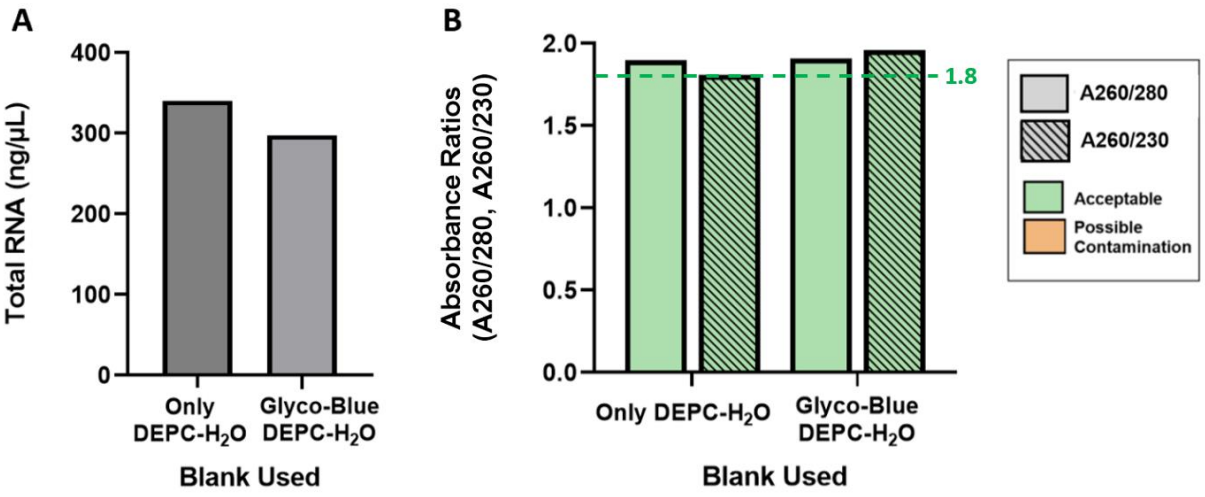

Figure 3.7: Nanodrop readings from TRIzol-isolated RNA from 400 µg start protein using mouse CTX, using DEPC-H_2O versus Glyco-Blue DEPC-H_2O to blank. (A) *shows total RNA (ng/µL).* ***(B)*** *shows read-outs of A260/280 and A260/230 ratios (hatched bars show A260/230 ratios of interest here). Green bars indicate that ratios are within an 'acceptable' range, whereas orange bars indicate that values are not within this range and therefore possible contamination may be present. Lowest acceptable threshold of 1.8 is indicated by a green dashed line. (n=1)*

3.1.5 RNA Isolation: Drying Times

As mentioned in the methods section, it is important that RNA pellets are fully dried during the RNA isolation stage, as leftover EtOH may cause contamination and interfere with downstream processes. However, pellets should also not be overdried as this will cause issues with re-solubilisation of the pellet. The original TRIzol Reagent product protocol (Invitrogen™) indicated that pellets should be air dried for 10-15 min, although the protocol being followed by Hanley Lab members at the time indicated an air-drying time of 30 min-1 h.

To determine which pellet drying time would be best to use for smaller RNA concentrations, 50 µg and 100 µg starting protein amounts were used first used to test drying times of 10, 20, 30 and 40 min (**Fig3.5, left-hand side**). None of the drying times were detrimental to A260/280 values, which remained at acceptable levels at all times tested (**Fig3.5C**). At 100 µg A260/230 values also remained unchanged apart from at 20 min drying time where a reduction was observed (**Fig3.5E**), although this could be due to experimental error. However, a downward trend in A260/230 was observed using 50 µg starting protein, as drying time was increased from 20 to 40 mins. This suggests that with smaller RNA pellets, longer drying times are detrimental to A260/230 ratios, even if total RNA and A260/280 values are unaffected. This reduction in A260/230 values is presumably due to over-drying of pellets. It is also notable that for 50 µg, all drying times tested gave A260/230 values below what would be deemed 'acceptable'.

As drying times of 10 and 20 min appeared to be most appropriate for starting protein of 50 µg, the effect of drying times of 0, 5, 10, 15 and 20 min using starting proteins of 25 µg and 50 µg was then tested (**Fig3.5, right-hand side**). Again, none of the drying times were detrimental to A260/280 values, which remained at acceptable levels at all times tested (**Fig3.5D**). For both 25 µg and 50 µg, all drying times tested gave A260/230 values below what would be deemed 'acceptable' (**Fig3.5F**), although with 50 µg an upward trend was observed when increasing drying time from 0 to 15 min. Due to this finding, in following experiments a drying time a minimum of 15 min was used.

As well as timing of air-drying, it is important to consider that other factors outside of our control such as the temperature or humidity could impact how long pellets take to dry. This added a layer of subjectivity to the times that pellets should be left to dry. So, although a minimum of 15 min was always used, RNA pellets were then checked by eye to make sure they did not look 'wet' still, as this would indicate EtOH was not fully evaporated at this point. Above 15 min drying time, pellets were resolubilised as soon as they looked 'dry', to avoid any potential over-drying.

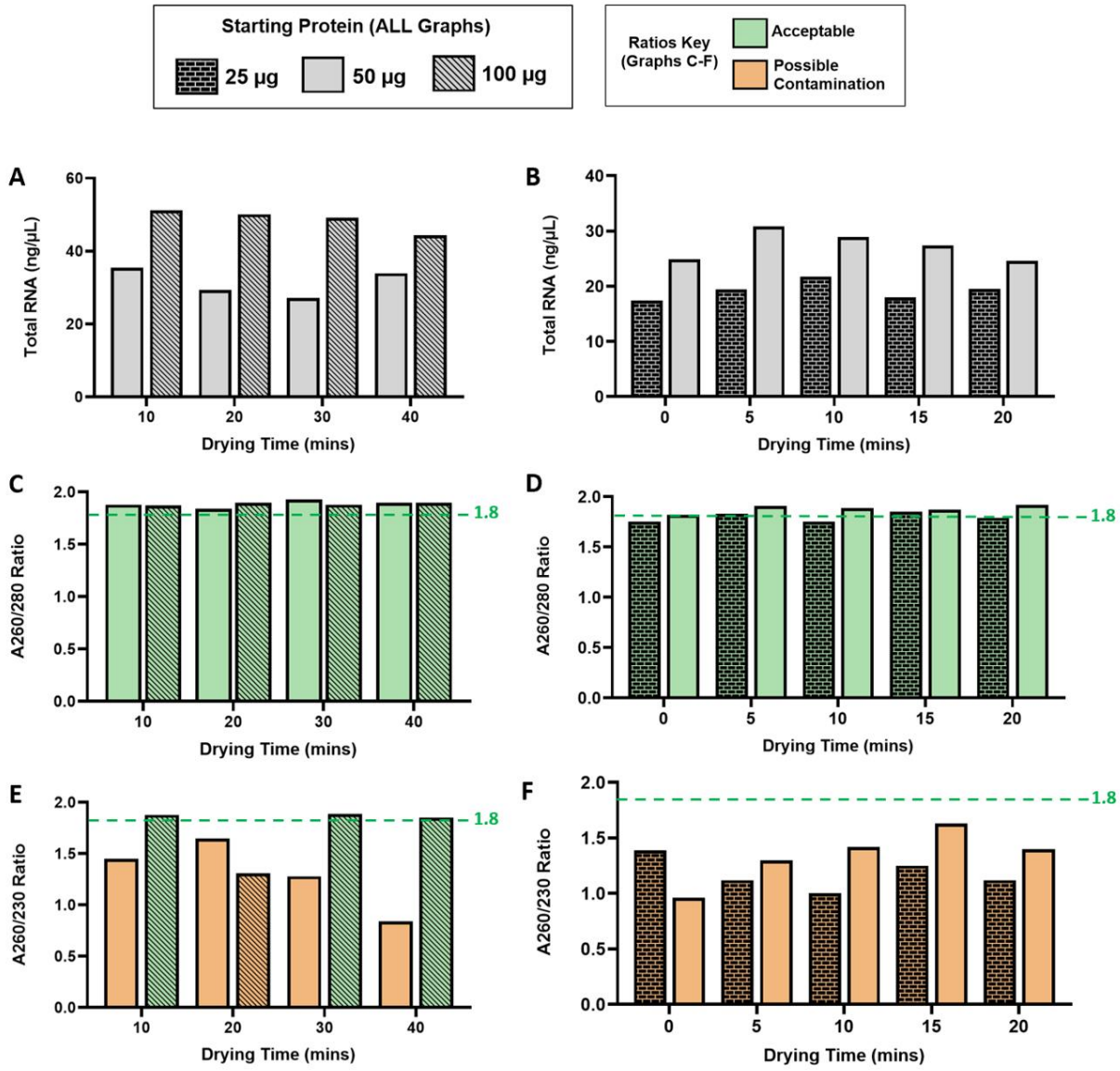

Figure 3.8: Nanodrop readings from TRIzol-isolated RNA, looking at the effects of different RNA pellet drying times using starting proteins 25-100 µg mouse CTX. (Left-hand side; A, C and E) *show one experiment (n=1) using 50 µg and 100 µg starting protein, and drying times of 10-40 min.* ***(Right-hand side; B, D and F)*** *show a subsequent experiment (n=1) using 25 µg and 50 µg starting protein, and drying times of 0-20 min.* ***(A-B)*** *show total RNA (ng/µL).* ***(C-D)*** *show read-outs of A260/280 and* ***(E-F)*** *A260/230 ratios. Green bars indicate that ratios are within an 'acceptable' range, whereas orange bars indicates that values are not within this range and therefore possible contamination may be present. Lowest acceptable threshold of 1.8 is indicated by a green dashed line. (n=1)*

3.1.6 Final TRIzol Protocol: Small Initial Protein Concentrations

Up to this point, only starting protein of 25 µg and above had been used. As a final consideration in the Nanodrop readings provided following TRIzol isolation, the effect of using starting protein of below 50 µg on total RNA concentrations, and on both A260/280 and A260/230 ratios was investigated. This was useful to consider as it was unknown how much Ago2 or DDX6 would be precipitated in later immunoprecipitations, from which RNA would later be isolated for use in RT-qPCRs.

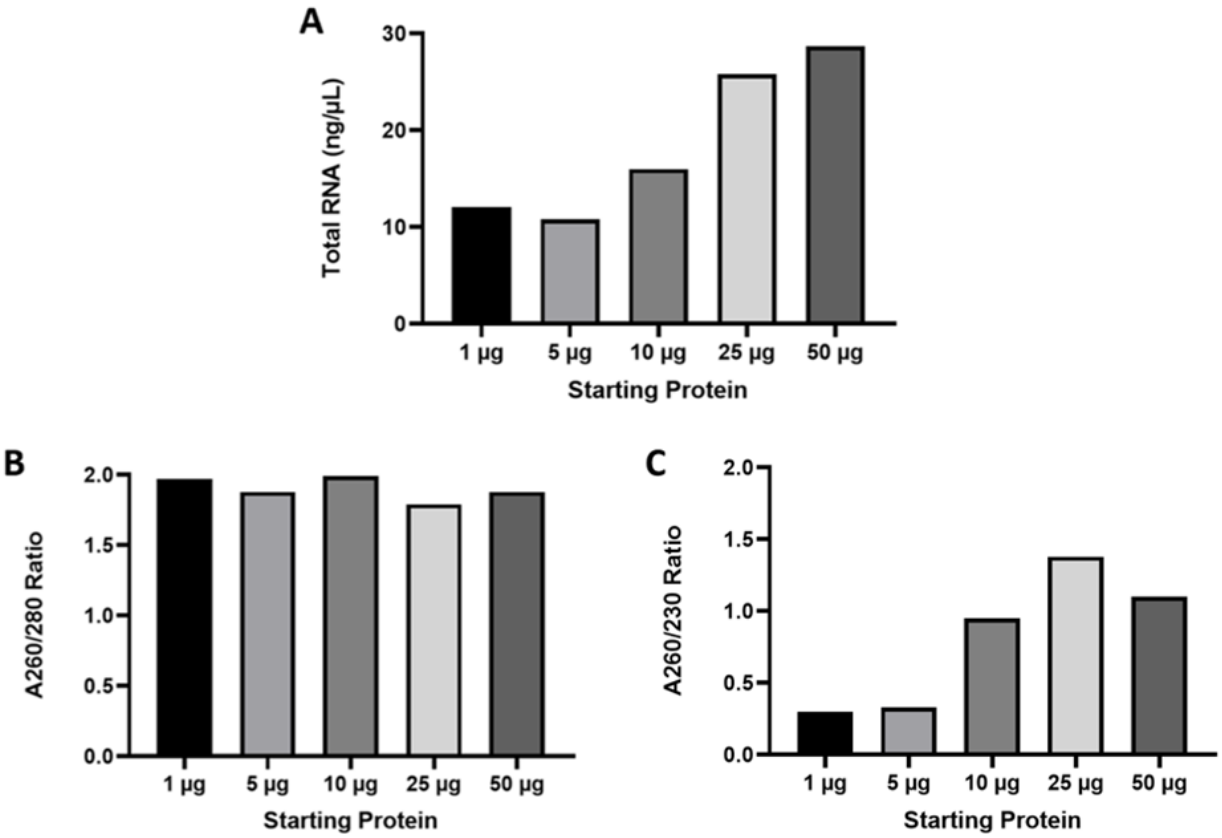

Figure 3.9: Nanodrop readings from TRIzol-isolated RNA using 1-50 µg start protein using mouse CTX. (A) *shows total RNA (ng/µL).* ***(B)*** *shows read-out of A260/280 ratios and* ***(C)*** *A260/230 ratios.*

To test the effect of using smaller starting protein amounts on Nanodrop readings, TRIzol isolation procedure that had been optimised up until this point to provide A260/280 and A260/230 ratios within an acceptable range (A260/280 of 1.8-2.2, A260/230 of >1.8) at higher starting protein, was used with starting protein of 1-50 µg (**Fig3.6**). The results indicated that even at much smaller starting protein amounts, an upward trend in total RNA concentration is still observed from 5 µg up to 50 µg of starting protein (**Fig3.6A**), although not from 1 µg to 5 µg. All A260/280 values were within the 'acceptable' range (**Fig3.6B**). A general upward trend in A260/230 values was observed when increasing starting protein from 1 µg to 50 µg (**Fig3.6C**), although values did not go above 1.4 – as with 25 µg starting protein, which would not usually be classed as 'acceptable' and would suggest organic contamination could have occurred. As the same protocol had provided higher concentrations of RNA from higher starting proteins (see **Fig3.6A**; 400 µg starting protein provided ~300 ng/µL RNA), with acceptable A260/280 and A260/230 values (see **Fig3.6B**), it is reasonable to suggest that lower concentrations of RNA (here, <30 ng/µL) isolated in the same manner causes reduced A260/230 ratios. This is presumably due to the fact that at smaller RNA concentrations, and hence smaller absorbances at A260, even small amounts of organic contaminants (i.e. EtOH residue left during drying stage) could cause large reductions in A260/230 values due to disproportionately large A230 values, that would usually not be detected with larger RNA concentrations.

Following TRIzol protocol optimisations, results indicate that using smaller amounts of starting protein (as is likely following immunoprecipitation) for RNA isolation, compromises A260/230 values. However, this may just be due to such small concentrations of RNA being present, and may not indicate any true presence of organic contamination that would interfere with downstream processes.

It is useful to note here that total RNA values for '10% inputs' in optimised RNA-IPs (discussed later in **Part 3**), initially containing ~50 µg of total protein, gave maximum total RNA concentrations of 35 ng/µL throughout all experiments, in line with total RNA values provided for this amount of starting protein in **Fig3.5A** and **Fig3.6A**. RNA in IP conditions provide even lower RNA concentrations than the input. With this considered, A260/230 ratios provided by the Nanodrop were not heavily relied upon during RNA-IPs. Instead, Nanodrop absorbance graphs could be inspected to ascertain whether an absorbance at wavelength 230 nm was higher than the absorbance at wavelength 260 nm. Where absorbance at wavelength 230 nm was above a 10 mm absorbance reading of 1.5, isolated RNA was considered contaminated, and was not used in downstream processes.

3.2 Immunoprecipitations of Ago2 and DDX6

3.2.1 Ago2 Co-Immunoprecipitation

As my research hypothesis was centred upon the regulation of Ago2 interactions by phosphorylation of S388, it was important to have an Ago2-Ab that would successfully precipitate this protein of interest before considering investigating any differences in Ago2-mRNA interactions between $Ago2^{WT}$ and $Ago2^{S388A}$ mice. Using 5 µg of Ago2-Ms Ab, both Ago2 and its interacting RISC protein DDX6 were successfully precipitated from mouse CTX lysate, in a Co-IP experiment (**Fig3.7**).

Only a single Co-IP experiment was carried out here, so it is therefore not possible to say whether the following results are statistically significant. However, the use of 5 µg Ago2-Ms Ab efficiently precipitated Ago2 with extraction efficiency up to 88% in $Ago2^{WT}$ CTX (**Fig3.7B**). The immunoprecipitation was also very clean, with no protein signal showing up in any of the control lanes for Ago2 or DDX6 blots, at an exposure where the protein band in IP lane could be well visualised (**Fig3.7A**). In addition to this, normalisation of immunoprecipitated Ago2 to input protein, indicated that 73% more Ago2 was precipitated in the $Ago2^{S388A}$ versus in the $Ago2^{WT}$ (**Fig3.7C**). Finally, the interaction between Ago2 and DDX6 showed a 13% decrease in $Ago2^{S388A}$ versus $Ago2^{WT}$ (**Fig3.7D**).

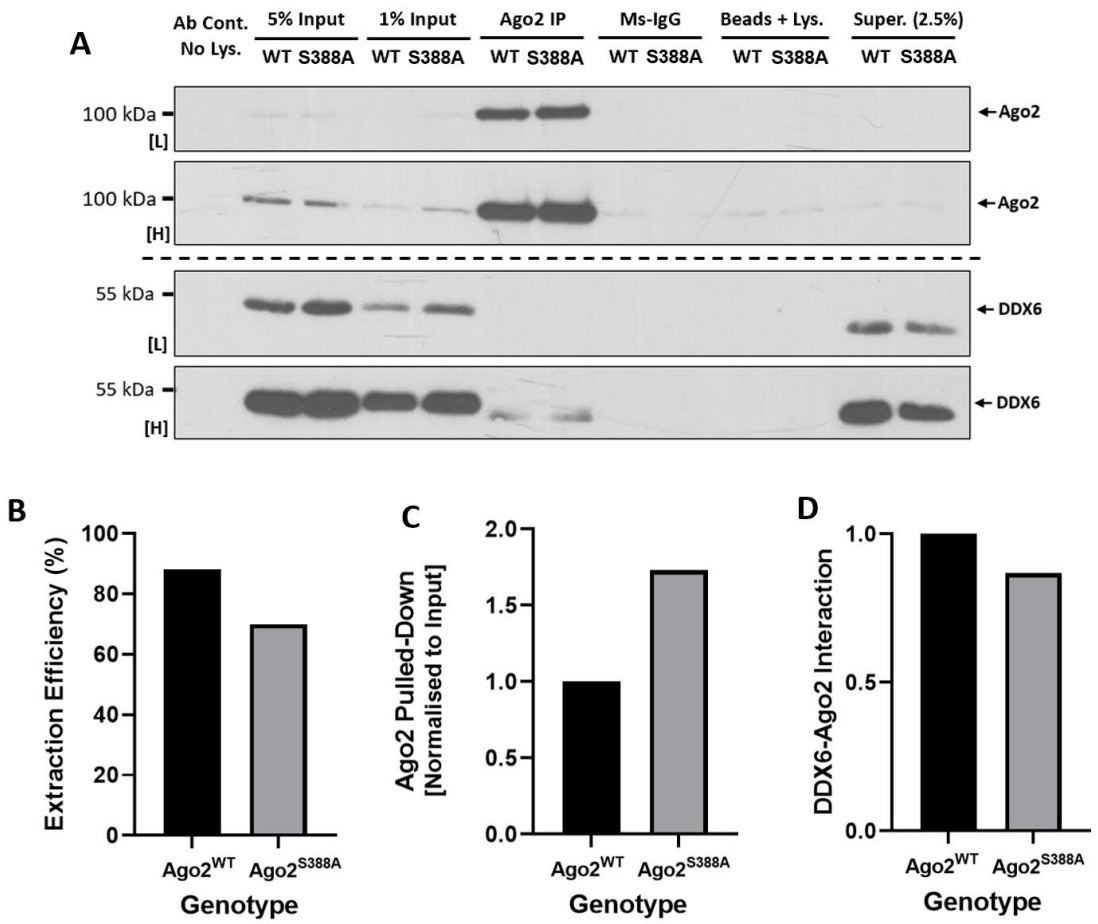

Figure 3.10: Successful IP of Ago2 using FUJIFILM Wako Ago2-Ms Ab, and Co-IP of interacting DDX6. Ago2^{WT} vs Ago2^{S388A}, using mouse CTX 1 mg/mL per condition. (A) *Western blot images from an Ago2 Co-IP using 5 µg Ago2-Ms Ab (Ago2 IP), where 50% of overall Ago2 IP was loaded in each case. Upper strips show immunoblotting for immunoprecipitated Ago2, and lower strips immunoblotting for interacting DDX6. Two exposures of each are shown, with higher and lower exposures indicated by [H] and [L], respectively. Both 5% and 1% Inputs were run, along with controls of 5 µg Ms-IgG (Ms-IgG), Ab and beads without lysate (Ab cont.), and lysate and beads without Ab added (Beads + Lys). Ab-bead incubation supernatant (Super.) was also run, comparable to a 2.5% start volume, or half that of the 5% input. The following graphs show quantification of data using protein signal values from these blots, n=1.* ***(B)*** *Quantification of extraction efficiency of the IP, using Ago2 supernatant and input protein.* ***(C)*** *Quantification of differences in Ago2 immunoprecipitated in Ago2^{WT} vs Ago2^{S388A}. IP protein signal normalised first to that of input, and then values normalised to Ago2^{WT}, such that Ago2^{WT} = 1.* ***(D)*** *Quantification of differences in DDX6 (interacting DDX6 normalised to respective input) interacting with immunoprecipitated Ago2 (i.e. then normalised to respective immunoprecipitated Ago2 signal) in Ago2^{WT} vs Ago2^{S388A}. Values were normalised to Ago2^{WT}, such that Ago2^{WT} = 1.*

3.2.2 DDX6 Immunoprecipitation

To understand more about the role that the RISC interacting protein DDX6 plays in the context of phosphorylation of Ago2 at S388, in regulating miRNA-mediated gene-silencing, it was important to achieve successful immunoprecipitation of DDX6. Successful immunoprecipitation of DDX6 using 4 µg DDX6-Ms Ab is shown in **Fig3.8**. It should be noted that in RNA-IPs described later in the chapter, from which protein-RNA interaction data was analysed, 6 µg DDX6-Ms Ab was used per condition for initial immunoprecipitation.

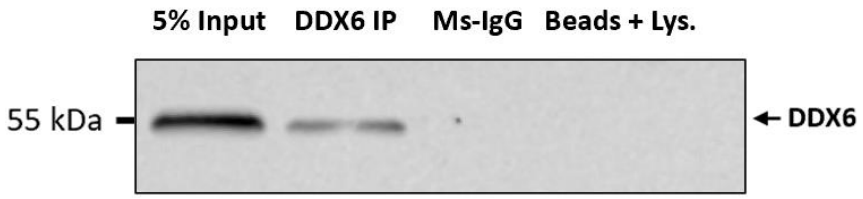

Figure 3.11: Successful IP of DDX6 using Biolegend DDX6-Ms Ab, in mouse brain tissue. *Western blot of a single DDX6 IP experiment (n=1) using 4 µg DDX6-Ms Ab, where 50% of overall DDX6 IP was loaded. Immunoblotting for immunoprecipitated DDX6 shown, alongside 5% input and control of 4 µg Ms-IgG (Ms-IgG), and lysate and beads without Ab added (Beads + Lys). No Ab and beads without lysate control, or Ab-bead supernatant was present in this experiment.*

3.3 Optimised RNA-Immunoprecipitations

3.3.1 Notes on Ct-Value Analysis

RNA-IPs were carried out using TRIzol protocol optimised as per **Part 3.1**. For optimised RNA-IPs, experiments where DNA or phenol had been taken up during TRIzol isolation were discarded, as contamination can cause interference during cDNA preparation and therefore cause unreliable Ct-values during RT-qPCR. Raw Ct-value data from remaining RT-qPCR runs was then inspected to ensure that within triplicate repeats the Ct-values were not highly variable, before calculating mean values. As the scale for Ct-values is exponential, even differences of ±1.0 within triplicates are out-of-place, although in this case ±2 from the middle value was considered acceptable. It was also determined whether individual Ct-values were within an acceptable range. The closer Ct-values are to 40 (the maximum number of amplification cycles carried out), the less reliable the values are, so a Ct of above 38 was not considered acceptable, and not used in further analysis. In instances where Ct-values were above 38, cDNA preparation and RT-qPCR was repeated using a higher volume of RNA during the cDNA preparation step. It is important to note that for the RNA-IP experiments where Ct-values were used to analyse protein-mRNA interaction levels, RNA data for Ms-IgG controls was not incorporated into the analysis any further than being deemed at an acceptable level for a control Ct-value (usually close to 40).

As final interaction data of $Ago2^{WT}$ and $Ago2^{S388A}$ is normalised to $Ago2^{WT}$ values such that $Ago2^{WT}$ always equals 1, values in the $Ago2^{S388A}$ of below 1 indicate decreased association of mRNA with either Ago2 or DDX6 when S388 is mutated such that it cannot be phosphorylated, and vice versa. As miRNA-mediated gene silencing occurs via the interaction of miRNA within the RISC and a target mRNA to cause its translational repression, a decreased association of mRNA with proteins within RISC would suggest a decrease in translational repression.

3.3.2 Notes on RNA-WB Normalisation

When carrying out analysis of RNA-IPs, it was important to normalise RNA interaction data to the amount of the Ago2 or DDX6 that the RNA would have been interacting with. From the conditions run on the WB in each case, one could either normalise to the direct 1% input or the immunoprecipitated Ago2 or DDX6. Normalising to the direct 1% input would provide analysis of the relative interaction levels between mRNA of interest and all Ago2 or DDX6 present in the original $Ago2^{WT}$ or $Ago2^{S388A}$ lysate, which would correct for uneven starting levels of Ago2 or DDX6 in each.

Normalising to immunoprecipitated Ago2 or DDX6, however, would theoretically provide analysis of the interaction levels between mRNA that had been precipitated and each molecule of Ago2 or DDX6 that had been precipitated, which originally made it the more obvious choice as a normalising factor.

However, it became apparent during experimentation that quantification of TRIzol-isolated protein signals may not be entirely reliable. For example, for a TRIzol-isolated protein input, the input had to be increased to 10% to provide a signal that could also be observed alongside a direct, non-TRIzol isolated input of only 1% (see **Fig3.11A** as exemplar), which brought into question the efficiency of protein isolation by TRIzol.

Although the final analysis of optimised RNA-IPs used 1% direct input as a normalising factor (see the **following sections**), the effect on final relative interaction values of normalising to TRIzol-isolated IP protein versus direct input was also investigated (**Fig3.9**). Using immunoprecipitated Ago2 or DDX6 to normalise usually gave a larger SEM than using input normalisation (**Fig3.9A-C**). Additionally, although still statistically non-significant, normalising to IP protein usually provided $Ago2^{S388A}$ interaction levels higher than those following input normalisation (**Fig3.9A-C**). In some cases, normalising to IP protein even resulted in interaction levels of >1.0 in $Ago2^{S388A}$ versus interaction levels <1.0 with input normalisation (**Fig3.9A-B**), which would provide opposing analysis of interactions if differences were significant.

With very small immunoprecipitated protein amounts such as those used in these RNA-IPs, the protein pellet was very difficult to visualise, so it is possible that during TRIzol-isolation not all of the protein pellet was isolated as it should be. It is also useful to note that following phase separation, the isolation of both RNA and protein are then carried out individually meaning that any issues occurring with protein isolation would not necessarily be reflected in RNA data. Vigorous shaking of the microfuge tube to dislodge the pellet entirely during washing stages has since been shown to allow easier visualisation of the whole protein pellet and would be useful in any future investigations to allow the IP protein signal to be more reliable as a normalisation factor. For the following RNA-IPs, however, the direct 1% input was used as the normalisation factor, more reliably correcting for uneven start levels of the Ago2 or DDX6. TRIzol-isolated proteins signals were still important to check that the IP had worked, and that no protein was appearing with controls.

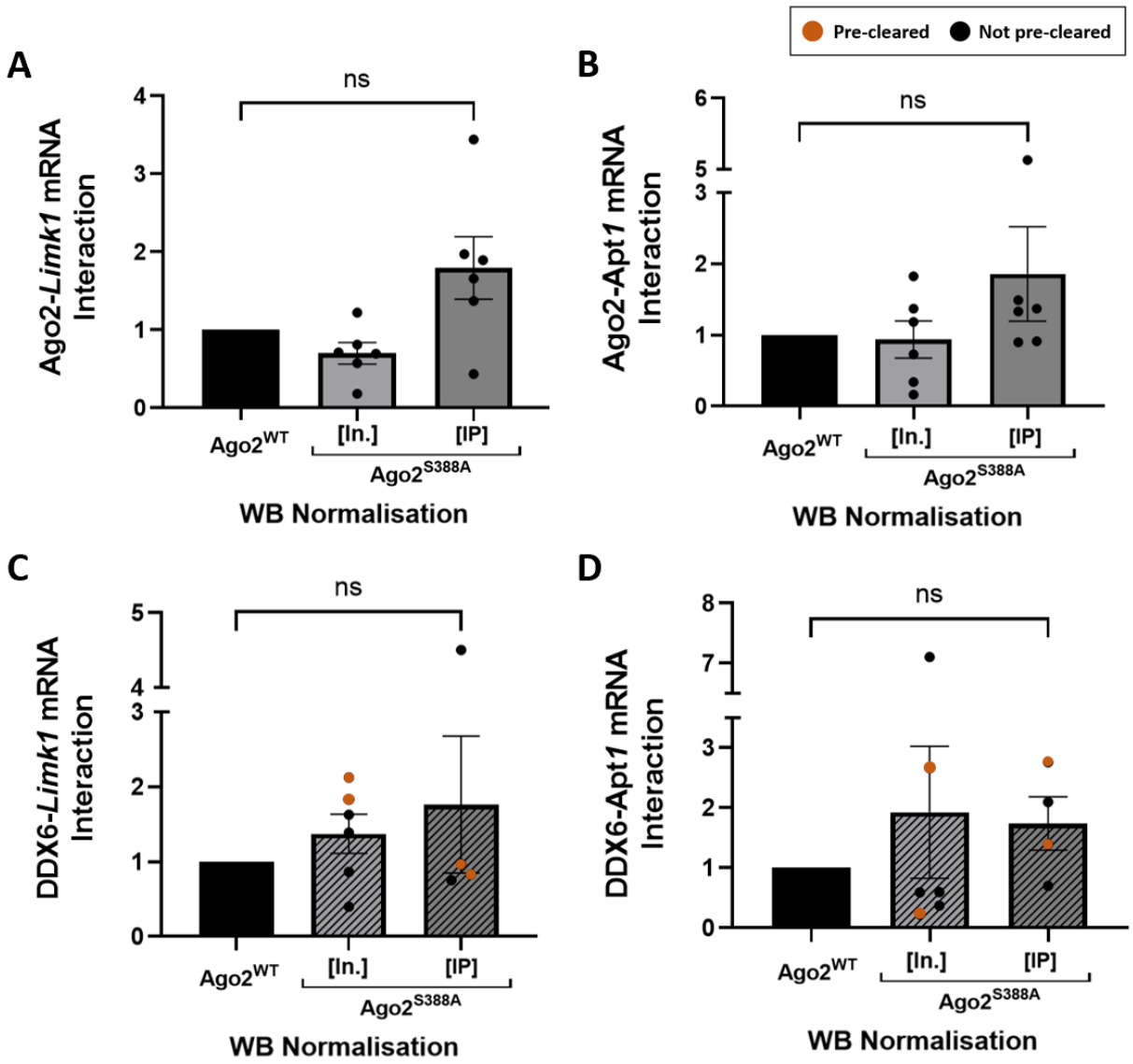

Figure 3.9: The effects of normalising RNA data to Western blot proteins, using 1% direct input versus TRIzol-isolated IP protein. (A-D) *Show quantification of interactions between mRNAs of interest with either Ago2 or DDX6. Pre-cleared experiments are indicated in orange. NB: Ago2^{S388A} normalised to [In.] is only shown above to indicate differences between normalisations, these results are discussed separately in further sections/figures. Both Ago2^{WT} and Ago2^{S388A} values were normalised to Ago2^{WT}, where Ago2^{WT} has a value of 1. *p<0.05; Unpaired student's t-test was used only to indicate non-significance (ns) between Ago2^{WT} and Ago2^{S388A} normalised to [IP], with SEM error bars indicated. No outliers were identified using boundaries of ±2.5 SD from the mean.* ***(A-B)*** *n=6 for each normalisation factor.* ***(C-D)*** *n=6 for 1% input [In.] normalisation, and n=4 for IP protein [IP] normalisation.*

3.3.3 Ago2 Interactions with *Limk1* and *Apt1* mRNA

Previous *in vitro* studies indicated that Ago2 phosphorylation at S387 was responsible for regulating the repression of specific mRNAs (Rajgor et al., 2018). Silencing of *Limk1* was shown to be sensitive to this phosphorylation, whereas silencing of *Apt1* was shown to be unaffected. Physical association of Ago2 with *Limk1* mRNA in neurons increases with the phosphomimic mutant Ago2-S387D and decreases with the phosphonull mutant Ago2-S387A, whereas Ago2-*Apt1* association remains unaffected (Perooli & Hanley, Unpublished Observations). To investigate whether these findings translate to *ex vivo* studies, RNA-IPs from Ago2^{WT} and Ago2^{S388A} mouse cortex tissue were utilised to investigate any differences in interactions between Ago2 and the mRNAs *Limk1* and *Apt1* that occur when S388 phosphorylation cannot occur.

Immunoprecipitation of Ago2 was first carried out, and optimised TRIzol protocol used to isolate RNA and protein from conditions as required. As well as isolating RNA from the immunoprecipitated Ago2 for each genotype, RNA is also isolated from an input for normalisation, and control Ms-IgG to ensure no non-specific binding of RNA was occurring. An example of the Nanodrop absorbances of isolated RNA for an individual RNA-IP repeat is shown in **Fig3.10**.

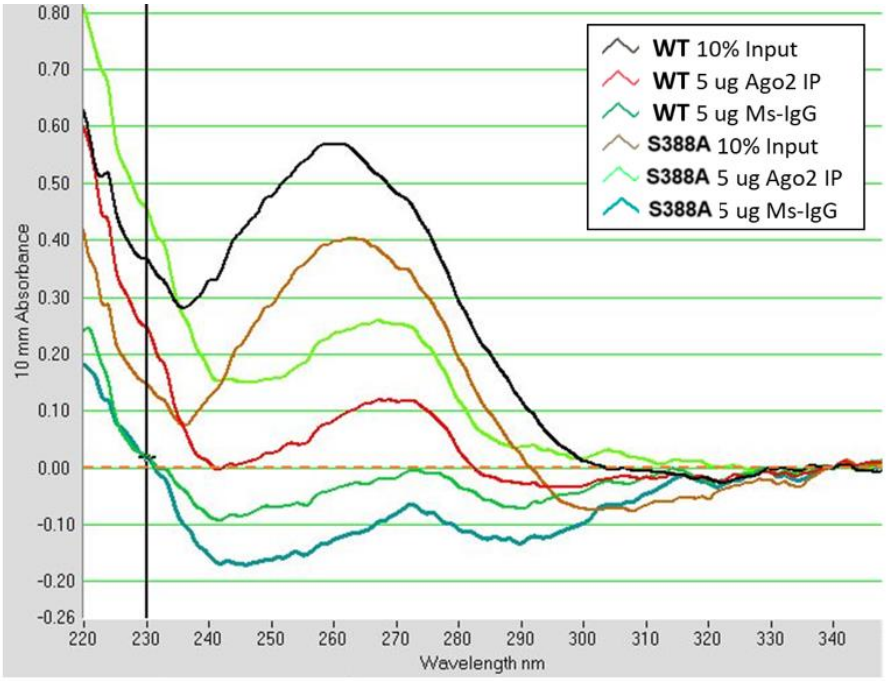

Figure 3.10: Exemplar Nanodrop graph following immunoprecipitation and TRIzol isolation of RNA present in each Ago2^{WT} and Ago2^{S388A} condition. *RNA absorbance occurs at wavelength 260 nm.*

The Nanodrop graph indicates successful precipitation of RNA from both Ago2^{WT} and Ago2^{S388A} using Ago2-Ms Ab, with highest RNA absorbances (260 nm) indicated in each input versus their associated IP (**Fig3.10**). RNA isolated from Ms-IgG control conditions in each case have an RNA absorbance of below 0, indicating RNA is not being non-specifically precipitated here.

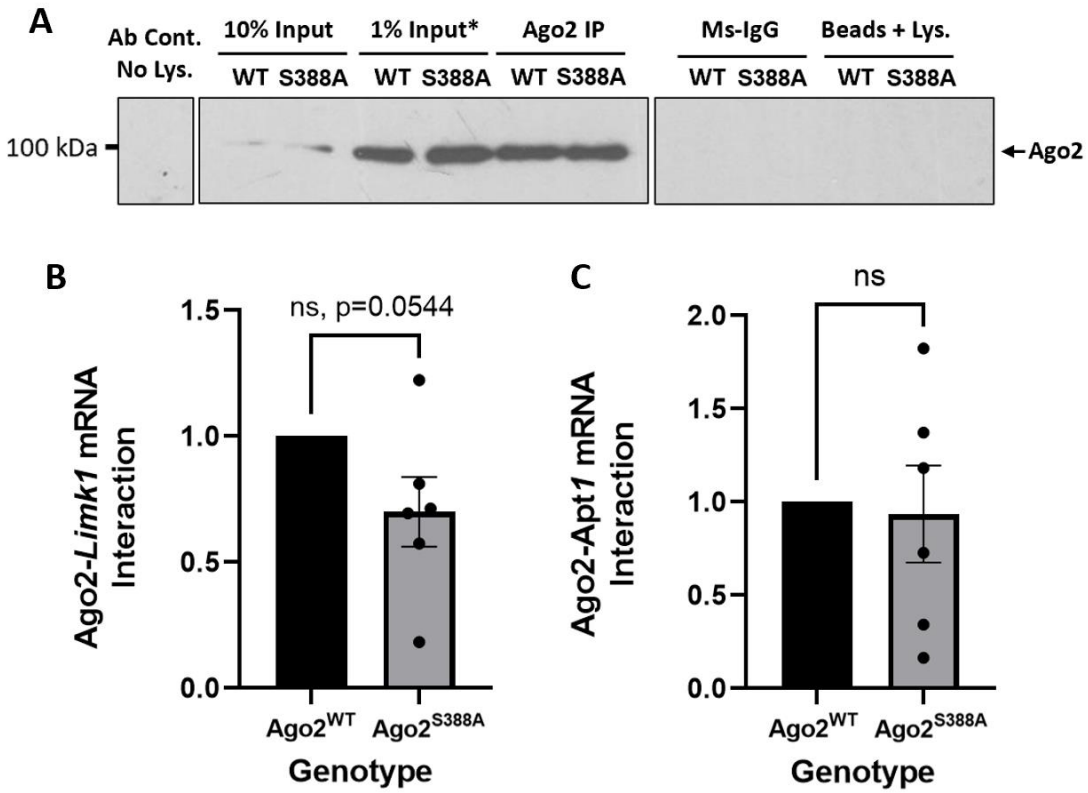

Figure 3.11: Ex vivo effects of S388A phosphonull mutation on the interactions between Ago2 and the mRNAs Limk1 and Apt1, within mouse cortex. (A) *Representative Western blot from an Ago2 RNA-IP using 5 µg Ago2-Ms Ab (Ago2 IP), where 50% of overall Ago2 IP was loaded in each case. Controls of 5 µg Ms-IgG (Ms-IgG), Ab and beads without lysate (Ab cont.), and lysate and beads without Ab added (Beads + Lys) are shown. All lanes contain 'indirect' protein that has been TRIzol-isolated, apart from the asterisked (*) 1% Input which was 'direct', or non-TRIzol-isolated.* ***(B)*** *and* ***(C)*** *show quantification of Ago2-Limk1 mRNA and Ago2-Apt1 mRNA relative interaction levels, respectively, in* Ago2^{WT} *mice versus* Ago2^{S388A}*. Relative associations of mRNA with Ago2 were found using a ΔΔCt-method using raw RT-qPCR Ct-values, before being normalised to the protein signal of their associated direct 1% input (as in* ***(A)****), for each* Ago2^{WT} *and* Ago2^{S388A}*. Both* Ago2^{WT} *and* Ago2^{S388A} *values were then normalised to* Ago2^{WT}*, where* Ago2^{WT} *has a value of 1. n=6, *p<0.05; Unpaired student's t-test, with standard error of the mean (SEM) error bars indicated. No outliers were identified using boundaries of ±2.5 standard deviation (SD) from the mean.*

Isolated RNA was then used in downstream cDNA preparation and RT-qPCR, as described in the **Methods**. RNA-IP results for Ago2 interactions with *Limk1* and *Apt1* are shown in **Fig3.11**.

Results indicated that no statistically significant difference in the association of Ago2 with either *Limk1* or *Apt1* mRNA was detectable between $Ago2^{WT}$ and $Ago2^{S388A}$ (**Fig3.11B** and **Fig3.11C**, respectively). Four of the six data points for the $Ago2^{S388A}$ in Ago2-*Limk1* interactions (**Fig3.11B**) were clustered around the mean of 0.700. There was a more observable spread of data in that of the $Ago2^{S388A}$ in Ago2-*Apt1* interactions (**Fig3.11C**), with a mean of 0.936.

3.3.4 DDX6 Interactions with *Limk1* and *Apt1* mRNA

To investigate whether any differences in interactions between RISC protein DDX6 and the mRNAs *Limk1* and *Apt1* occur when S388 cannot be phosphorylated, RNA-IPs from $Ago2^{WT}$ and $Ago2^{S388A}$ mouse cortex tissue were again utilised, with results shown in **Fig3.12**.

To provide 6 repeats of DDX6 RNA-IPs, protein-RNA interaction analysis from 4 non-pre-cleared experiments and 2 pre-cleared experiments were pooled together. The only difference in experimental procedure for the pre-cleared repeats was an additional step of lysate pre-clearing using non-blocked beads prior to immunoprecipitation, where beads were originally causing non-specific protein binding to occur in control lanes. Non-pre-cleared repeats used in final analysis did not have non-specific binding occurring in control lanes, indicating pre-clearing was not necessary for these experiments. WB examples for pre-cleared and non-pre-cleared repeats are indicated in **Fig3.12A** and **Fig3.12B**, respectively.

Results indicated that no statistically significant difference between $Ago2^{WT}$ and $Ago2^{S388A}$ mice was detectable in the association of DDX6 with either *Limk1* or *Apt1* mRNA (**Fig3.12C** and **Fig3.12D**, respectively). No statistically significant difference in DDX6-*Apt1* mRNA interaction may be in-line with hypothesised outcomes of this experiment due to previous findings that S387 phosphorylation *in vitro* does not affect Ago2-*Apt1* interactions *in vitro*.

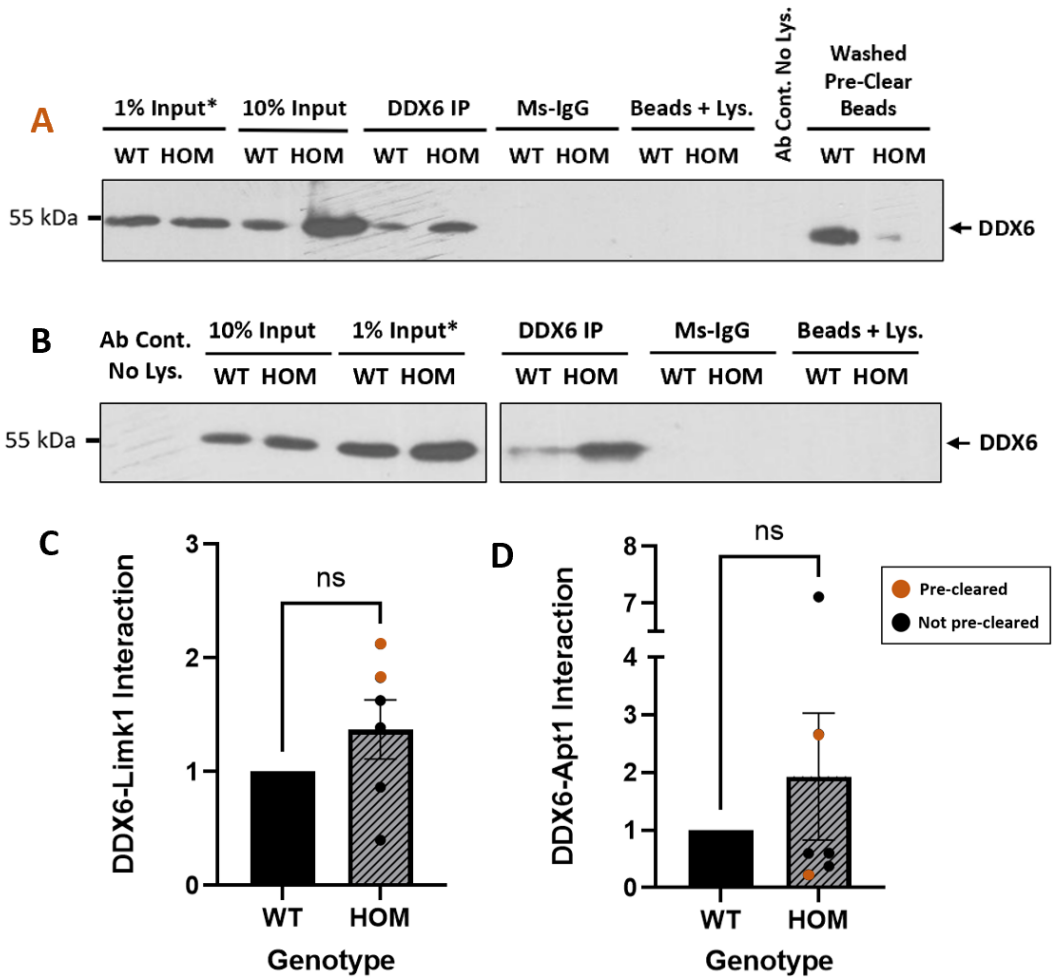

Figure 3.12: Ex vivo effects of S388A phosphonull mutation on the interactions between DDX6 and the mRNAs Limk1 and Apt1, within mouse cortex. ***(A)*** *Representative Western blot from a DDX6 RNA-IP using 6 µg DDX6-Ms Ab (DDX6 IP), where initial pre-clearing of lysate took place. Proteins bound to the pre-clear beads following washes are shown (Washed Pre-Clear Beads).* ***(B)*** *Representative Western blot from a DDX6 RNA-IP using 6 µg DDX6-Ms Ab (DDX6 IP), where pre-clearing was not carried out. In both (**A**) and (**B**) 50% of overall DDX6 IP was loaded in each case. Controls of 6 µg Ms-IgG (Ms-IgG), Ab and beads without lysate (Ab cont.), and lysate with only beads added (Beads + Lys) are also shown. All lanes contain 'indirect' protein that has been TRIzol-isolated, apart from the asterisked (*) 1% Input which was 'direct', or non-TRIzol-isolated.* ***(C)*** *and* ***(D)*** *show quantification of DDX6-Limk1 mRNA and DDX6-Apt1 mRNA interactions, respectively, in $Ago2^{WT}$ mice versus $Ago2^{S388A}$. Pre-cleared experiments are indicated in orange. Relative associations of mRNA with Ago2 were found using a ΔΔCt-method using raw RT-qPCR Ct-values, before being normalised to the protein signal of their associated direct 1% input (as in (**A**) and (**B**)) for each $Ago2^{WT}$ and $Ago2^{S388A}$. Both $Ago2^{WT}$ and $Ago2^{S388A}$ values were then normalised to $Ago2^{WT}$, where $Ago2^{WT}$ has a value of 1. n=6 (Pre-cleared n=2, non-pre-cleared n=4) *p<0.05; Unpaired student's t-test, with SEM error bars indicated. No outliers were identified using boundaries of ±2.5 SD from the mean.*

4. Discussion

4.1 Experimental Results

4.1.1 Ago2 and DDX6 Interactions with *Limk1* and *Apt1*

Although the difference in Ago2-*Limk1* direct interaction between $Ago2^{WT}$ and $Ago2^{S388A}$ was shown to be not statistically significant, it is notable that the p-value in this RNA-IP experiment was 0.0544, which is extremely close to the cut-off alpha value of 0.05. Therefore, it is reasonable to consider that a statistically significant reduction in Ago2-*Limk1* mRNA interaction (of around 30%) could have been detected with further repeats, which would be in line with the hypothesised effects of the S388A mutation. For the Ago2-*Apt1* mRNA interaction, no significant difference (5%, p=0.8093) was observed between $Ago2^{WT}$ and $Ago2^{S388A}$, which on the other hand is in-line with hypothesised outcomes of this experiment due to previous findings that S387 phosphorylation does not affect this interaction *in vitro* (Perooli & Hanley, Unpublished Observations).

The phosphorylation of Ago2 at S387 has previously been shown *in vitro* to cause both increased DDX6-Ago2 interaction and increased Ago2-*Limk1* interaction, so it was hypothesised that lack of this phosphorylation event could disrupt association of DDX6-*Limk1 ex vivo*. However, no statistically significant difference in DDX6-*Limk1* mRNA interaction was observed between $Ago2^{WT}$ and $Ago2^{S388A}$.

4.1.2 Higher Immunoprecipitated Ago2 Levels in $Ago2^{S388A}$

Although Ago2-Ms Co-IP data (**Fig3.7**) can only be classed as preliminary in this specific collection of data due to one repeat being carried out, it is interesting to note that the higher levels of Ago2 being precipitated in $Ago2^{S388A}$ versus $Ago2^{WT}$ mouse CTX was shown to be statistically significant in experiments carried out by Johnnie Chronias in the Hanley lab (Chronias & Hanley, Unpublished Observations). This suggests that the S388A mutation of Ago2 allows more Ago2 to become bound by Ago2-Ms Ab during immunoprecipitation. This could be due to either a greater amount of 'free-Ago2' within the CTX, that is not bound to other interacting or accessory proteins that could hinder Ab-binding or could indicate that the mutation makes the Ago2 protein itself more able to bind to the Ab in question. Theoretically, it would make sense that removing the ability of Ago2 to be post-translationally modified in this manner could reduce its ability to interact with and regulate other proteins.

4.1.3 Relative Differences in mRNA Ct-Values, in Ago2 versus DDX6 RNA-IPs

Although not detailed in the results section, differences in Ct-values were observed between Ago2 and DDX6 RNA-IPs using the optimised IP conditions for each IP Ab. For the same mouse cortex tissue, the DDX6 IP usually provided a Ct-value of ~1-2 below that of the Ago2 IP. For example, Ct-values of 35.4 versus 37.7 were provided for *Apt1* in DDX6 RNA-IP and Ago2 RNA-IP, respectively, using the same mouse cortex. These differences in Ct-values indicate that more mRNA – either *Limk1* or *Apt1* – was detected when using the DDX6 IP rather than the Ago2 IP. This implies that differences in IP efficiency may have occurred between the Ago2 and DDX6 IPs, which has subsequently caused differences in the co-purification of mRNAs. Looking at the Western blots from IPs of Ago2 (**Fig3.7**) and DDX6 (**Fig3.8**), this is particularly interesting as the Ago2 IP appears much more efficient at pulling down the protein of interest than the DDX6 IP. It is therefore not clear why higher amounts of mRNA would be precipitated using the DDX6 IP. It is possible that the Ago2 IP Ab may bind Ago2 protein in such a way that the binding of mRNA is somewhat impaired, whereas this does not occur with the DDX6 IP Ab, hence the unimpaired DDX6-mRNA interaction allows higher amounts of mRNA precipitation overall.

4.2 Future Directions

4.2.1 Effects of S388A on Dendritic Spine Morphology

It is important to understand the effect of S388A on the morphology of spines, as this mechanism of regulation has been linked to spine shrinkage. Using Golgi-Cox method to stain neurons in brain tissue sections of $Ago2^{WT}$ and $Ago2^{S388A}$, differences in spine morphology could be investigated. For example, differences in dimensions of both the neck and heads of spines could be investigated, as well as differences in the ratios of different spine classifications present along dendrites. This could also be investigated in different brain regions of the mice, to see if tissue-specific differences present.

4.2.2 Effects of S388A in the Hippocampus

Differences in miRNA expression profiles and of their regulation occurs within different areas of the mammalian brain. It is reasonable to consider therefore, that regulation of direct binding of Ago2 or DDX6 to the mRNAs *Limk1* or *Apt1*, and therefore also regulation of their repression, may vary in different mouse brain regions. Differential regulation throughout the brain is important to investigate due to the differing behaviours that each brain region involves. It is important to consider that RNA-IP experiments in this project were only carried out using cortex tissue, and not with hippocampal tissue.

It is widely established that spatial memory is hippocampal-dependent and object recognition memory largely is perirhinal cortex-dependent (Cinalli Jr. et al., 2020). Grace Ryall in the Hanley Group has carried out a range of behavioural studies using the same $Ago2^{WT}$ and $Ago2^{S388A}$ mice to investigate how either of these behavioural processes may be impacted when S388 phosphorylation cannot occur. These *in vivo* studies looked at differences in task performance between $Ago2^{WT}$ and $Ago2^{S388A}$ mice. Data was pooled from two groups of mice – an older group (4-6 months old) and a younger group (2-4 months old), each consisting of 10-11 mice per genotype, to look for conserved differences. Conserved, significant deficits in short-term spatial memory were observed in the phosphonull mice versus wild-type, using an object location task with 5-minute delay between sample and test phases (Ryall & Hanley, Unpublished Observations). As there was no observable effect of the S388 mutation on object recognition task performance, but there was using the short-term object location task, it suggests that S388 phosphorylation specifically contributes to the consolidation and retrieval of memories within the hippocampus.

4.2.3 Regulation of Further mRNAs

As phosphorylation of Ago2 at S387 has been defined as a specific pathway for structural plasticity, investigating its effects on mRNAs encoding structural proteins would be of interest. RNA-IP investigations using brain tissue of $Ago2^{WT}$ and $Ago2^{S388A}$ could be used to identify differences in direct binding of RISC proteins – including Ago2 and DDX6 – with mRNAs encoding known key structural proteins such as Arp2/3 and cofilin. These proteins are vital in cytoskeletal actin regulation within spines, and therefore also in the dynamic structural changes that spines undergo in LTP and LTD. However, as an approach this would be highly time-consuming. Better yet, more unbiased, high-throughput approaches to screening can be used, for example utilising next generation sequencing to indicate differences in RNA associations between $Ago2^{WT}$ and $Ago2^{S388A}$.

Different miRNAs can work in concert with one another to provide changes in plasticity. It is useful to consider that different pools of miRNAs may have their regulation switched on or off by the phosphorylation event that occurs at S388. Identification of further mRNAs that have their binding to RISC proteins – and therefore repression – regulated through S388 phosphorylation will allow further insight into these different pools of miRNAs that have their regulation switched on and off by this phosphorylation.

Differences in gene expression and translation of structural proteins that occur between $Ago2^{WT}$ and $Ago2^{S388A}$ mice could then be investigated further using *in vitro* neuronal cultures and viral transductions to access changes in spine morphology and size that occur when these proteins are knocked down or overexpressed.

4.2.4 Generation of Different Transgenics

Although not financially feasible, it is exciting to explore the possibility of further transgenic animal models that could be used to investigate the role of S388 phosphorylation. Generation of mouse models where the S388A mutation was limited to a specific brain region, such as the cortex or hippocampus, would allow tissue-specific investigations of behaviour to be carried out, without effects from other brain regions providing a confounding variable in analysis of results. Animal transgenics where the S388A transgene was inducible, rather than constantly ‘on’ would allow for the timescales of certain behavioural or electrophysiological changes that occur with inhibited S388 phosphorylation to be determined.

4.2.5 Amelioration of Aspects of AD

The importance of miRNA regulation in the context of diseases is extremely important to consider. Understanding how miRNAs mediate regulation of LTD, and of synaptic weakening, can improve our understanding of diseases that are caused by dysregulation or aberration of certain spine-related processes within the brain. Breeding $Ago2^{S388A/S388A}$ mice with mouse models for aspects of AD would allow any potential amelioration of AD phenotypes that occur with reduced S388 phosphorylation to be investigated.

Changes in miRNA profiles occur during AD (Liu et al., 2022). Therefore, understanding how these changes are both regulated and linked to structural plasticity could allow for future use of certain miRNAs as disease biomarkers, allowing for earlier detection and earlier intervention. Understanding roles of miRNAs within structural plasticity can also provide possible avenues for future therapeutic interventions.

4.2.6 RISC as a Therapeutic Target

In addition to miRNAs as therapeutic targets, the regulation of RISC protein interactions could also provide avenues for therapeutic intervention. For example, investigations into the use of small peptides to disrupt DDX6 binding to RISC, or the use of inhibitors of specific post-translational modifications on RISC and RISC-associated proteins could be of use.

References

Akao, Y., Marukawa, O., Morikawa, H., Nakao, K., Kamei, M., Hachiya, T., & Tsujimoto, Y. (1995). The rck/p54 candidate proto-oncogene product is a 54-kilodalton D-E-A-D box protein differentially expressed in human and mouse tissues. *Cancer Res*, *55*(15), 3444-3449.

Alshalalfa, M. (2012). MicroRNA Response Elements-Mediated miRNA-miRNA Interactions in Prostate Cancer. *Adv Bioinformatics*, *2012*, 839837. https://doi.org/10.1155/2012/839837

Antunes, G., & Simoes-de-Souza, F. M. (2018). AMPA receptor trafficking and its role in heterosynaptic plasticity. *Scientific Reports*, *8*(1), 10349. https://doi.org/10.1038/s41598-018-28581-w

Baltaci, S. B., Mogulkoc, R., & Baltaci, A. K. (2019). Molecular Mechanisms of Early and Late LTP. *Neurochem Res*, *44*(2), 281-296. https://doi.org/10.1007/s11064-018-2695-4

Bassani, S., Folci, A., Zapata, J., & Passafaro, M. (2013). AMPAR trafficking in synapse maturation and plasticity. *Cellular and Molecular Life Sciences*, *70*(23), 4411-4430. https://doi.org/10.1007/s00018-013-1309-1

Behm-Ansmant, I., Rehwinkel, J., Doerks, T., Stark, A., Bork, P., & Izaurralde, E. (2006). mRNA degradation by miRNAs and GW182 requires both CCR4:NOT deadenylase and DCP1:DCP2 decapping complexes. *Genes Dev*, *20*(14), 1885-1898. https://doi.org/10.1101/gad.1424106

Berry, K. P., & Nedivi, E. (2017). Spine Dynamics: Are They All the Same? *Neuron*, *96*(1), 43-55. https://doi.org/10.1016/j.neuron.2017.08.008

Bliss, T. V., & Collingridge, G. L. (1993). A synaptic model of memory: long-term potentiation in the hippocampus. *Nature*, *361*(6407), 31-39. https://doi.org/10.1038/361031a0

Bliss, T. V., & Cooke, S. F. (2011). Long-term potentiation and long-term depression: a clinical perspective. *Clinics (Sao Paulo)*, *66 Suppl 1*(Suppl 1), 3-17. https://doi.org/10.1590/s1807-59322011001300002

Bliss, T. V., & Lomo, T. (1973). Long-lasting potentiation of synaptic transmission in the dentate area of the anaesthetized rabbit following stimulation of the perforant path. *J Physiol*, *232*(2), 331-356. https://doi.org/10.1113/jphysiol.1973.sp010273

Boda, B., Alberi, S., Nikonenko, I., Node-Langlois, R., Jourdain, P., Moosmayer, M., Parisi-Jourdain, L., & Muller, D. (2004). The mental retardation protein PAK3 contributes to synapse formation and plasticity in hippocampus. *J Neurosci*, *24*(48), 10816-10825. https://doi.org/10.1523/jneurosci.2931-04.2004

Bridge, K. S., Shah, K. M., Li, Y., Foxler, D. E., Wong, S. C. K., Miller, D. C., Davidson, K. M., Foster, J. G., Rose, R., Hodgkinson, M. R., Ribeiro, P. S., Aboobaker, A. A., Yashiro, K., Wang, X., Graves, P. R., Plevin, M. J., Lagos, D., & Sharp, T. V. (2017). Argonaute Utilization for miRNA Silencing Is Determined by Phosphorylation-Dependent Recruitment of LIM-Domain-Containing Proteins. *Cell Rep*, *20*(1), 173-187. https://doi.org/10.1016/j.celrep.2017.06.027

Byth, L. A. (2014). Ca(2+)- and CaMKII-mediated processes in early LTP. *Ann Neurosci*, *21*(4), 151-153. https://doi.org/10.5214/ans.0972.7531.210408

Cenik, E. S., & Zamore, P. D. (2011). Argonaute proteins. *Curr Biol*, *21*(12), R446-449. https://doi.org/10.1016/j.cub.2011.05.020

Chauderlier, A., Gilles, M., Spolcova, A., Caillierez, R., Chwastyniak, M., Kress, M., Drobecq, H., Bonnefoy, E., Pinet, F., Weil, D., Buée, L., Galas, M.-C., & Lefebvre, B. (2018). Tau/DDX6 interaction increases microRNA activity. *Biochimica et Biophysica Acta (BBA) - Gene Regulatory Mechanisms*, *1861*(8), 762-772. https://doi.org/https://doi.org/10.1016/j.bbagrm.2018.06.006

Chen, W., & Qin, C. (2015). General hallmarks of microRNAs in brain evolution and development. *RNA Biol*, *12*(7), 701-708. https://doi.org/10.1080/15476286.2015.1048954

Chronias, J. & Hanley, J. (Unpublished Observations). *MSc Research*. University of Bristol.

Cinalli Jr., D. A., Cohen, S. J., Guthrie, K., & Stackman Jr., R. W. (2020). Object Recognition Memory: Distinct Yet Complementary Roles of the Mouse CA1 and Perirhinal Cortex [Original Research]. *Frontiers in Molecular Neuroscience*, *13*. https://doi.org/10.3389/fnmol.2020.527543

Connor, S. A., & Wang, Y. T. (2016). A Place at the Table: LTD as a Mediator of Memory Genesis. *Neuroscientist*, *22*(4), 359-371. https://doi.org/10.1177/1073858415588498

Cotman, C. W., Banker, G., Churchill, L., & Taylor, D. (1974). Isolation of postsynaptic densities from rat brain. *J Cell Biol*, *63*(2 Pt 1), 441-455. https://doi.org/10.1083/jcb.63.2.441

DeFelipe, J. (2006). Brain plasticity and mental processes: Cajal again. *Nature Reviews Neuroscience*, *7*(10), 811-817. https://doi.org/10.1038/nrn2005

Dieterich, D. C., Hodas, J. J. L., Gouzer, G., Shadrin, I. Y., Ngo, J. T., Triller, A., Tirrell, D. A., & Schuman, E. M. (2010). In situ visualization and dynamics of newly synthesized proteins in rat hippocampal neurons. *Nature Neuroscience*, *13*(7), 897-905. https://doi.org/10.1038/nn.2580

Douglas, R. N., & Birchler, J. A. (2013). MicroRNAs in Eukaryotes. In W. J. Lennarz & M. D. Lane (Eds.), *Encyclopedia of Biological Chemistry (Second Edition)* (pp. 98-102). Academic Press. https://doi.org/https://doi.org/10.1016/B978-0-12-378630-2.00623-X

Dudek, S. M., & Bear, M. F. (1992). Homosynaptic long-term depression in area CA1 of hippocampus and effects of N-methyl-D-aspartate receptor blockade. *Proc Natl Acad Sci U S A*, *89*(10), 4363-4367. https://doi.org/10.1073/pnas.89.10.4363

Ernoult-Lange, M., Baconnais, S., Harper, M., Minshall, N., Souquere, S., Boudier, T., Bénard, M., Andrey, P., Pierron, G., Kress, M., Standart, N., le Cam, E., & Weil, D. (2012). Multiple binding of repressed mRNAs by the P-body protein Rck/p54. *Rna*, *18*(9), 1702-1715. https://doi.org/10.1261/rna.034314.112

Faber, D. S., & Pereda, A. E. (2018). Two Forms of Electrical Transmission Between Neurons [Review]. *Frontiers in Molecular Neuroscience*, *11*. https://doi.org/10.3389/fnmol.2018.00427

Fiore, R., Khudayberdiev, S., Christensen, M., Siegel, G., Flavell, S. W., Kim, T.-K., Greenberg, M. E., & Schratt, G. (2009). Mef2-mediated transcription of the miR379–410 cluster regulates activity-dependent dendritogenesis by fine-tuning Pumilio2 protein levels. *The EMBO Journal*, *28*(6), 697-710. https://doi.org/https://doi.org/10.1038/emboj.2009.10

Fox, K., & Stryker, M. (2017). Integrating Hebbian and homeostatic plasticity: introduction. *Philos Trans R Soc Lond B Biol Sci*, *372*(1715). https://doi.org/10.1098/rstb.2016.0413

García-López, P., García-Marín, V., & Freire, M. (2007). The discovery of dendritic spines by Cajal in 1888 and its relevance in the present neuroscience. *Prog Neurobiol*, *83*(2), 110-130. https://doi.org/10.1016/j.pneurobio.2007.06.002

Garner, C. C., Tucker, R. P., & Matus, A. (1988). Selective localization of messenger RNA for cytoskeletal protein MAP2 in dendrites. *Nature*, *336*(6200), 674-677. https://doi.org/10.1038/336674a0

Ha, M., & Kim, V. N. (2014). Regulation of microRNA biogenesis. *Nat Rev Mol Cell Biol*, *15*(8), 509-524. https://doi.org/10.1038/nrm3838

Hansen, K. B., Wollmuth, L. P., Bowie, D., Furukawa, H., Menniti, F. S., Sobolevsky, A. I., Swanson, G. T., Swanger, S. A., Greger, I. H., Nakagawa, T., McBain, C. J., Jayaraman, V., Low, C. M., Dell'Acqua, M. L., Diamond, J. S., Camp, C. R., Perszyk, R. E., Yuan, H., & Traynelis, S. F. (2021). Structure, Function, and Pharmacology of Glutamate Receptor Ion Channels. *Pharmacol Rev*, *73*(4), 298-487. https://doi.org/10.1124/pharmrev.120.000131

Harris, K. M., Jensen, F. E., & Tsao, B. (1992). Three-dimensional structure of dendritic spines and synapses in rat hippocampus (CA1) at postnatal day 15 and adult ages: implications for the maturation of synaptic physiology and long-term potentiation. *J Neurosci*, *12*(7), 2685-2705. https://doi.org/10.1523/jneurosci.12-07-02685.1992

He, K.-W., Song, L., Cummings, L. W., Goldman, J., Huganir, R. L., & Lee, H.-K. (2009). Stabilization of Ca2+-permeable AMPA receptors at perisynaptic sites by GluR1-S845 phosphorylation. *Proceedings of the National Academy of Sciences*, *106*, 20033 - 20038.

Hebb, D. O. (1949). *The organization of behavior; a neuropsychological theory*. Wiley.

Herculano-Houzel, S. (2009). The human brain in numbers: a linearly scaled-up primate brain. *Front Hum Neurosci*, *3*, 31. https://doi.org/10.3389/neuro.09.031.2009

Holt, C. E., Martin, K. C., & Schuman, E. M. (2019). Local translation in neurons: visualization and function. *Nature Structural & Molecular Biology*, *26*(7), 557-566. https://doi.org/10.1038/s41594-019-0263-5

Horman, S. R., Janas, M. M., Litterst, C., Wang, B., MacRae, I. J., Sever, M. J., Morrissey, D. V., Graves, P., Luo, B., Umesalma, S., Qi, H. H., Miraglia, L. J., Novina, C. D., & Orth, A. P. (2013). Akt-mediated phosphorylation of argonaute 2 downregulates cleavage and upregulates translational repression of MicroRNA targets. *Mol Cell*, *50*(3), 356-367. https://doi.org/10.1016/j.molcel.2013.03.015

Hotulainen, P., & Hoogenraad, C. C. (2010). Actin in dendritic spines: connecting dynamics to function. *J Cell Biol*, *189*(4), 619-629. https://doi.org/10.1083/jcb.201003008

Huber, K. M., Roder, J. C., & Bear, M. F. (2001). Chemical Induction of mGluR5- and Protein Synthesis–Dependent Long-Term Depression in Hippocampal Area CA1. *Journal of Neurophysiology*, *86*(1), 321-325. https://doi.org/10.1152/jn.2001.86.1.321

Ipsaro, J. J., & Joshua-Tor, L. (2015). From guide to target: molecular insights into eukaryotic RNA-interference machinery. *Nature Structural & Molecular Biology*, *22*(1), 20-28. https://doi.org/10.1038/nsmb.2931

Iwakawa, H. O., & Tomari, Y. (2022). Life of RISC: Formation, action, and degradation of RNA-induced silencing complex. *Mol Cell*, *82*(1), 30-43. https://doi.org/10.1016/j.molcel.2021.11.026

Iwasaki, S., & Tomari, Y. (2009). Argonaute-mediated translational repression (and activation). *Fly (Austin)*, *3*(3), 204-206.

Jembrek, M. J., & Vlainic, J. (2015). GABA Receptors: Pharmacological Potential and Pitfalls. *Curr Pharm Des*, *21*(34), 4943-4959. https://doi.org/10.2174/1381612821666150914121624

Jin, S., Zhan, J., & Zhou, Y. (2021). Argonaute proteins: structures and their endonuclease activity. *Molecular Biology Reports*, *48*(5), 4837-4849. https://doi.org/10.1007/s11033-021-06476-w

Josa-Prado, F., Henley, J. M., & Wilkinson, K. A. (2015). SUMOylation of Argonaute-2 regulates RNA interference activity. *Biochem Biophys Res Commun*, *464*(4), 1066-1071. https://doi.org/10.1016/j.bbrc.2015.07.073

Kasai, H., Fukuda, M., Watanabe, S., Hayashi-Takagi, A., & Noguchi, J. (2010). Structural dynamics of dendritic spines in memory and cognition. *Trends in Neurosciences*, *33*(3), 121-129. https://doi.org/https://doi.org/10.1016/j.tins.2010.01.001

Katz, B., & Miledi, R. (1968). The role of calcium in neuromuscular facilitation. *The Journal of Physiology*, *195*(2), 481-492. https://doi.org/https://doi.org/10.1113/jphysiol.1968.sp008469

Kirino, Y., Kim, N., de Planell-Saguer, M., Khandros, E., Chiorean, S., Klein, P. S., Rigoutsos, I., Jongens, T. A., & Mourelatos, Z. (2009). Arginine methylation of Piwi proteins catalysed by dPRMT5 is required for Ago3 and Aub stability. *Nature Cell Biology*, *11*(5), 652-658. https://doi.org/10.1038/ncb1872

Kwak, P. B., & Tomari, Y. (2012). The N domain of Argonaute drives duplex unwinding during RISC assembly. *Nat Struct Mol Biol*, *19*(2), 145-151. https://doi.org/10.1038/nsmb.2232

Lee, Y., Kim, M., Han, J., Yeom, K. H., Lee, S., Baek, S. H., & Kim, V. N. (2004). MicroRNA genes are transcribed by RNA polymerase II. *Embo j*, *23*(20), 4051-4060. https://doi.org/10.1038/sj.emboj.7600385

Li, X., Wang, X., Cheng, Z., & Zhu, Q. (2020). AGO2 and its partners: a silencing complex, a chromatin modulator, and new features. *Crit Rev Biochem Mol Biol*, *55*(1), 33-53. https://doi.org/10.1080/10409238.2020.1738331

Lisman, J. (2003). Actin's actions in LTP-induced synapse growth. *Neuron*, *38*(3), 361-362. https://doi.org/10.1016/s0896-6273(03)00257-5

Liu, J., Carmell, M. A., Rivas, F. V., Marsden, C. G., Thomson, J. M., Song, J. J., Hammond, S. M., Joshua-Tor, L., & Hannon, G. J. (2004). Argonaute2 is the catalytic engine of mammalian RNAi. *Science*, *305*(5689), 1437-1441. https://doi.org/10.1126/science.1102513

Liu, S., Fan, M., Zheng, Q., Hao, S., Yang, L., Xia, Q., Qi, C., & Ge, J. (2022). MicroRNAs in Alzheimer's disease: Potential diagnostic markers and therapeutic targets. *Biomedicine & Pharmacotherapy*, *148*, 112681. https://doi.org/https://doi.org/10.1016/j.biopha.2022.112681

Lledo, P. M., Hjelmstad, G. O., Mukherji, S., Soderling, T. R., Malenka, R. C., & Nicoll, R. A. (1995). Calcium/calmodulin-dependent kinase II and long-term potentiation enhance synaptic transmission by the same mechanism. *Proc Natl Acad Sci U S A*, *92*(24), 11175-11179. https://doi.org/10.1073/pnas.92.24.11175

Lopez-Orozco, J., Pare, J. M., Holme, A. L., Chaulk, S. G., Fahlman, R. P., & Hobman, T. C. (2015). Functional analyses of phosphorylation events in human Argonaute 2. *Rna*, *21*(12), 2030-2038. https://doi.org/10.1261/rna.053207.115

Ma, J. B., Ye, K., & Patel, D. J. (2004). Structural basis for overhang-specific small interfering RNA recognition by the PAZ domain. *Nature*, *429*(6989), 318-322. https://doi.org/10.1038/nature02519

Malenka, R. C., Kauer, J. A., Perkel, D. J., & Nicoll, R. A. (1989). The impact of postsynaptic calcium on synaptic transmission — its role in long-term potentiation. *Trends in Neurosciences*, *12*(11), 444-450. https://doi.org/https://doi.org/10.1016/0166-2236(89)90094-5

Mathys, H., Basquin, J., Ozgur, S., Czarnocki-Cieciura, M., Bonneau, F., Aartse, A., Dziembowski, A., Nowotny, M., Conti, E., & Filipowicz, W. (2014). Structural and biochemical insights to the role of the CCR4-NOT complex and DDX6 ATPase in microRNA repression. *Mol Cell*, *54*(5), 751-765. https://doi.org/10.1016/j.molcel.2014.03.036

McManus, M. T., & Sharp, P. A. (2002). Gene silencing in mammals by small interfering RNAs. *Nature Reviews Genetics*, *3*(10), 737-747. https://doi.org/10.1038/nrg908

Meer, E., Wang, D., Kim, S., Barr, I., Guo, F., & Martin, K. (2012). Identification of a cis-acting element that localizes mRNA to synapses. *Proceedings of the National Academy of Sciences of the United States of America*, *109*, 4639-4644. https://doi.org/10.1073/pnas.1116269109

Meijer, H. A., Smith, E. M., & Bushell, M. (2014). Regulation of miRNA strand selection: follow the leader? *Biochem Soc Trans*, *42*(4), 1135-1140. https://doi.org/10.1042/bst20140142

Meng, Y., Zhang, Y., Tregoubov, V., Janus, C., Cruz, L., Jackson, M., Lu, W. Y., MacDonald, J. F., Wang, J. Y., Falls, D. L., & Jia, Z. (2002). Abnormal spine morphology and enhanced LTP in LIMK-1 knockout mice. *Neuron*, *35*(1), 121-133. https://doi.org/10.1016/s0896-6273(02)00758-4

Meriney, S. D., & Fanselow, E. E. (2019). Chapter 14 - Synaptic Plasticity. In S. D. Meriney & E. E. Fanselow (Eds.), *Synaptic Transmission* (pp. 287-329). Academic Press. https://doi.org/https://doi.org/10.1016/B978-0-12-815320-8.00014-4

Michlewski, G., & Cáceres, J. F. (2019). Post-transcriptional control of miRNA biogenesis. *Rna*, *25*(1), 1-16. https://doi.org/10.1261/rna.068692.118

Miller, S., Yasuda, M., Coats, J. K., Jones, Y., Martone, M. E., & Mayford, M. (2002). Disruption of dendritic translation of CaMKIIalpha impairs stabilization of synaptic plasticity and memory consolidation. *Neuron*, *36*(3), 507-519. https://doi.org/10.1016/s0896-6273(02)00978-9

Milstein, A. D., Li, Y., Bittner, K. C., Grienberger, C., Soltesz, I., Magee, J. C., & Romani, S. (2021). Bidirectional synaptic plasticity rapidly modifies hippocampal representations. *Elife*, *10*. https://doi.org/10.7554/eLife.73046

Muljo, S. A., Kanellopoulou, C., & Aravind, L. (2010). MicroRNA targeting in mammalian genomes: genes and mechanisms. *Wiley Interdiscip Rev Syst Biol Med*, *2*(2), 148-161. https://doi.org/10.1002/wsbm.53

Müller, W., & Connor, J. A. (1991). Dendritic spines as individual neuronal compartments for synaptic Ca2+ responses. *Nature*, *354*(6348), 73-76. https://doi.org/10.1038/354073a0

Murakoshi, H., Wang, H., & Yasuda, R. (2011). Local, persistent activation of Rho GTPases during plasticity of single dendritic spines. *Nature*, *472*(7341), 100-104. https://doi.org/10.1038/nature09823

Naruse, K., Matsuura-Suzuki, E., Watanabe, M., Iwasaki, S., & Tomari, Y. (2018). In vitro reconstitution of chaperone-mediated human RISC assembly. *Rna*, *24*(1), 6-11. https://doi.org/10.1261/rna.063891.117

Nikolić, M. (2008). The Pak1 Kinase: An Important Regulator of Neuronal Morphology and Function in the Developing Forebrain. *Molecular Neurobiology*, *37*(2), 187-202. https://doi.org/10.1007/s12035-008-8032-1

Nishiyama, J. (2019). Plasticity of dendritic spines: Molecular function and dysfunction in neurodevelopmental disorders. *Psychiatry Clin Neurosci*, *73*(9), 541-550. https://doi.org/10.1111/pcn.12899

Ostareck, D. H., Naarmann-de Vries, I. S., & Ostareck-Lederer, A. (2014). DDX6 and its orthologs as modulators of cellular and viral RNA expression. *Wiley Interdiscip Rev RNA*, *5*(5), 659-678. https://doi.org/10.1002/wrna.1237

Ouyang, Y., Rosenstein, A., Kreiman, G., Schuman, E. M., & Kennedy, M. B. (1999). Tetanic stimulation leads to increased accumulation of Ca(2+)/calmodulin-dependent protein kinase II via dendritic protein synthesis in hippocampal neurons. *J Neurosci*, *19*(18), 7823-7833. https://doi.org/10.1523/jneurosci.19-18-07823.1999

Parkinson, G. T., & Hanley, J. G. (2018). Mechanisms of AMPA Receptor Endosomal Sorting [Review]. *Frontiers in Molecular Neuroscience*, *11*. https://doi.org/10.3389/fnmol.2018.00440

Perooli, F. & Hanley, J. (Unpublished Observations). *PhD Research*. University of Bristol.

Pitman, R. M. (1984). The versatile synapse. *J Exp Biol*, *112*, 199-224. https://doi.org/10.1242/jeb.112.1.199

Qi, H. H., Ongusaha, P. P., Myllyharju, J., Cheng, D., Pakkanen, O., Shi, Y., Lee, S. W., Peng, J., & Shi, Y. (2008). Prolyl 4-hydroxylation regulates Argonaute 2 stability. *Nature*, *455*(7211), 421-424. https://doi.org/10.1038/nature07186

Rajgor, D., Fiuza, M., Parkinson, G. T., & Hanley, J. G. (2017). The PICK1 Ca(2+) sensor modulates N-methyl-d-aspartate (NMDA) receptor-dependent microRNA-mediated translational repression in neurons. *J Biol Chem*, *292*(23), 9774-9786. https://doi.org/10.1074/jbc.M117.776302

Rajgor, D., Sanderson, T. M., Amici, M., Collingridge, G. L., & Hanley, J. G. (2018). NMDAR-dependent Argonaute 2 phosphorylation regulates miRNA activity and dendritic spine plasticity. *Embo j*, *37*(11). https://doi.org/10.15252/embj.201797943

Ramalingam, P., Palanichamy, J. K., Singh, A., Das, P., Bhagat, M., Kassab, M. A., Sinha, S., & Chattopadhyay, P. (2014). Biogenesis of intronic miRNAs located in clusters by independent transcription and alternative splicing. *Rna*, *20*(1), 76-87. https://doi.org/10.1261/rna.041814.113

Ramón, Y., & Cajal, S. R. y. (1888). Estructura de los centros nerviosos de las Aves.

Ravindran, S., Nalavadi, V. C., & Muddashetty, R. S. (2019). BDNF Induced Translation of Limk1 in Developing Neurons Regulates Dendrite Growth by Fine-Tuning Cofilin1 Activity [Original Research]. *Frontiers in Molecular Neuroscience*, *12*. https://doi.org/10.3389/fnmol.2019.00064

Reiner, A., & Levitz, J. (2018). Glutamatergic Signaling in the Central Nervous System: Ionotropic and Metabotropic Receptors in Concert. *Neuron*, *98*(6), 1080-1098. https://doi.org/10.1016/j.neuron.2018.05.018

Rodriguez, A., Griffiths-Jones, S., Ashurst, J. L., & Bradley, A. (2004). Identification of mammalian microRNA host genes and transcription units. *Genome Res*, *14*(10a), 1902-1910. https://doi.org/10.1101/gr.2722704

Rouya, C., Siddiqui, N., Morita, M., Duchaine, T. F., Fabian, M. R., & Sonenberg, N. (2014). Human DDX6 effects miRNA-mediated gene silencing via direct binding to CNOT1. *Rna*, *20*(9), 1398-1409. https://doi.org/10.1261/rna.045302.114

Ryall, G. & Hanley, J. (Unpublished Observations). *PhD Research*. University of Bristol.

Schelski, M., & Bradke, F. (2017). Neuronal polarization: From spatiotemporal signaling to cytoskeletal dynamics. *Molecular and Cellular Neuroscience*, *84*, 11-28. https://doi.org/https://doi.org/10.1016/j.mcn.2017.03.008

Schratt, G. M., Tuebing, F., Nigh, E. A., Kane, C. G., Sabatini, M. E., Kiebler, M., & Greenberg, M. E. (2006). A brain-specific microRNA regulates dendritic spine development. *Nature*, *439*(7074), 283-289. https://doi.org/10.1038/nature04367

Segal, M. (2017). Dendritic spines: Morphological building blocks of memory. *Neurobiology of Learning and Memory*, *138*, 3-9. https://doi.org/https://doi.org/10.1016/j.nlm.2016.06.007

Sheng, M., & Hoogenraad, C. C. (2007). The postsynaptic architecture of excitatory synapses: a more quantitative view. *Annu Rev Biochem*, *76*, 823-847. https://doi.org/10.1146/annurev.biochem.76.060805.160029

Shepherd, J. D., & Huganir, R. L. (2007). The Cell Biology of Synaptic Plasticity: AMPA Receptor Trafficking. *Annual Review of Cell and Developmental Biology*, *23*(1), 613-643. https://doi.org/10.1146/annurev.cellbio.23.090506.123516

Sherman, D. L., & Brophy, P. J. (2005). Mechanisms of axon ensheathment and myelin growth. *Nature Reviews Neuroscience*, *6*(9), 683-690. https://doi.org/10.1038/nrn1743

Shigeoka, T., Jung, J., Holt, C. E., & Jung, H. (2018). Axon-TRAP-RiboTag: Affinity Purification of Translated mRNAs from Neuronal Axons in Mouse In Vivo. *Methods Mol Biol*, *1649*, 85-94. https://doi.org/10.1007/978-1-4939-7213-5_5

Siegel, G., Obernosterer, G., Fiore, R., Oehmen, M., Bicker, S., Christensen, M., Khudayberdiev, S., Leuschner, P. F., Busch, C. J. L., Kane, C., Hübel, K., Dekker, F., Hedberg, C., Rengarajan, B., Drepper, C., Waldmann, H., Kauppinen, S., Greenberg, M. E., Draguhn, A., . . . Schratt, G. M. (2009). A functional screen implicates microRNA-138-dependent regulation of the depalmitoylation enzyme APT1 in dendritic spine morphogenesis. *Nature Cell Biology*, *11*(6), 705-716. https://doi.org/10.1038/ncb1876

Simon, B., Kirkpatrick, J. P., Eckhardt, S., Reuter, M., Rocha, E. A., Andrade-Navarro, M. A., Sehr, P., Pillai, R. S., & Carlomagno, T. (2011). Recognition of 2'-O-Methylated 3'-End of piRNA by the PAZ Domain of a Piwi Protein. *Structure*, *19*(2), 172-180. https://doi.org/https://doi.org/10.1016/j.str.2010.11.015

Smith, A. C. W., & Kenny, P. J. (2018). MicroRNAs regulate synaptic plasticity underlying drug addiction. *Genes Brain Behav*, *17*(3), e12424. https://doi.org/10.1111/gbb.12424

Sobczyk, A., & Svoboda, K. (2007). Activity-dependent plasticity of the NMDA-receptor fractional Ca2+ current. *Neuron*, *53*(1), 17-24. https://doi.org/10.1016/j.neuron.2006.11.016

Song, I., & Huganir, R. L. (2002). Regulation of AMPA receptors during synaptic plasticity. *Trends in Neurosciences*, *25*(11), 578-588. https://doi.org/https://doi.org/10.1016/S0166-2236(02)02270-1

Steward, O. (1997). mRNA localization in neurons: a multipurpose mechanism? *Neuron*, *18*(1), 9-12. https://doi.org/10.1016/s0896-6273(01)80041-6

Sutton, M. A., Ito, H. T., Cressy, P., Kempf, C., Woo, J. C., & Schuman, E. M. (2006). Miniature neurotransmission stabilizes synaptic function via tonic suppression of local dendritic protein synthesis. *Cell*, *125*(4), 785-799. https://doi.org/10.1016/j.cell.2006.03.040

Tamagnini, F., Burattini, C., Casoli, T., Balietti, M., Fattoretti, P., & Aicardi, G. (2012). Early impairment of long-term depression in the perirhinal cortex of a mouse model of Alzheimer's disease. *Rejuvenation Res*, *15*(2), 231-234. https://doi.org/10.1089/rej.2011.1311

Tan, H. L., Chiu, S. L., Zhu, Q., & Huganir, R. L. (2020). GRIP1 regulates synaptic plasticity and learning and memory. *Proc Natl Acad Sci U S A*, *117*(40), 25085-25091. https://doi.org/10.1073/pnas.2014827117

Tassabehji, M., Metcalfe, K., Fergusson, W. D., Carette, M. J. A., Dore, J. K., Donnai, D., Read, A. P., Pröschel, C., Gutowski, N. J., Mao, X., & Sheer, D. (1996). LIM–kinase deleted in Williams syndrome. *Nature Genetics*, *13*(3), 272-273. https://doi.org/10.1038/ng0796-272

Tian, Y., Simanshu, D. K., Ma, J. B., & Patel, D. J. (2011). Structural basis for piRNA 2'-O-methylated 3'-end recognition by Piwi PAZ (Piwi/Argonaute/Zwille) domains. *Proc Natl Acad Sci U S A*, *108*(3), 903-910. https://doi.org/10.1073/pnas.1017762108

von Bohlen und Halbach, O. (2010). Dendritic spine abnormalities in mental retardation. *Cell and Tissue Research*, *342*(3), 317-323. https://doi.org/10.1007/s00441-010-1070-9

Wang, G., Grone, B., Colas, D., Appelbaum, L., & Mourrain, P. (2011). Synaptic plasticity in sleep: learning, homeostasis and disease. *Trends Neurosci*, *34*(9), 452-463. https://doi.org/10.1016/j.tins.2011.07.005

Wang, H. W., Noland, C., Siridechadilok, B., Taylor, D. W., Ma, E., Felderer, K., Doudna, J. A., & Nogales, E. (2009). Structural insights into RNA processing by the human RISC-loading complex. *Nat Struct Mol Biol*, *16*(11), 1148-1153. https://doi.org/10.1038/nsmb.1673

Wang, I. F., Ho, P. C., & Tsai, K. J. (2022). MicroRNAs in Learning and Memory and Their Impact on Alzheimer's Disease. *Biomedicines*, *10*(8). https://doi.org/10.3390/biomedicines10081856

Wang, Y., Arribas-Layton, M., Chen, Y., Lykke-Andersen, J., & Sen, G. L. (2015). DDX6 Orchestrates Mammalian Progenitor Function through the mRNA Degradation and Translation Pathways. *Mol Cell*, *60*(1), 118-130. https://doi.org/10.1016/j.molcel.2015.08.014

Wang, Z., Wang, Y., Liu, T., Wang, Y., & Zhang, W. (2019). Effects of the PIWI/MID domain of Argonaute protein on the association of miRNAi's seed base with the target. *Rna*, *25*(5), 620-629. https://doi.org/10.1261/rna.069328.118

Wu, B., Eliscovich, C., Yoon, Y. J., & Singer, R. H. (2016). Translation dynamics of single mRNAs in live cells and neurons. *Science*, *352*(6292), 1430-1435. https://doi.org/10.1126/science.aaf1084

Wu, J., Yang, J., Cho, W. C., & Zheng, Y. (2020). Argonaute proteins: Structural features, functions and emerging roles. *J Adv Res*, *24*, 317-324. https://doi.org/10.1016/j.jare.2020.04.017

Yamauchi, T. (2002). Molecular constituents and phosphorylation-dependent regulation of the post-synaptic density. *Mass Spectrom Rev*, *21*(4), 266-286. https://doi.org/10.1002/mas.10033

Yang, N., Higuchi, O., Ohashi, K., Nagata, K., Wada, A., Kangawa, K., Nishida, E., & Mizuno, K. (1998). Cofilin phosphorylation by LIM-kinase 1 and its role in Rac-mediated actin reorganization. *Nature*, *393*(6687), 809-812. https://doi.org/10.1038/31735

Yasuda, R., Hayashi, Y., & Hell, J. W. (2022). CaMKII: a central molecular organizer of synaptic plasticity, learning and memory. *Nat Rev Neurosci*, *23*(11), 666-682. https://doi.org/10.1038/s41583-022-00624-2

Yergert, K. M., Doll, C. A., O'Rouke, R., Hines, J. H., & Appel, B. (2021). Identification of 3' UTR motifs required for mRNA localization to myelin sheaths in vivo. *PLoS Biol*, *19*(1), e3001053. https://doi.org/10.1371/journal.pbio.3001053

Yokoi, N., Fukata, M., & Fukata, Y. (2012). Chapter One - Synaptic Plasticity Regulated by Protein–Protein Interactions and Posttranslational Modifications. In K. W. Jeon (Ed.), *International Review of Cell and Molecular Biology* (Vol. 297, pp. 1-43). Academic Press. https://doi.org/https://doi.org/10.1016/B978-0-12-394308-8.00001-7

Zeng, Y., Sankala, H., Zhang, X., & Graves, P. R. (2008). Phosphorylation of Argonaute 2 at serine-387 facilitates its localization to processing bodies. *Biochem J*, *413*(3), 429-436. https://doi.org/10.1042/bj20080599

Zhang, S., Zhang, X., Bie, Y., Kong, J., Wang, A., Qiu, Y., & Zhou, X. (2022). STUB1 regulates antiviral RNAi through inducing ubiquitination and degradation of Dicer and AGO2 in mammals. *Virol Sin*, *37*(4), 569-580. https://doi.org/10.1016/j.virs.2022.05.001

Zhou, Q., Homma, K. J., & Poo, M. M. (2004). Shrinkage of dendritic spines associated with long-term depression of hippocampal synapses. *Neuron*, *44*(5), 749-757. https://doi.org/10.1016/j.neuron.2004.11.011

Zucker, R. S., & Regehr, W. G. (2002). Short-Term Synaptic Plasticity. *Annual Review of Physiology*, *64*(1), 355-405. https://doi.org/10.1146/annurev.physiol.64.092501.114547